SATBAYEV UNIVERSITY

ISSN 2959-2348 (Online)

ENGINEERING JOURNAL of Satbayev University

Volume 148 (Issue 1)
February 2026

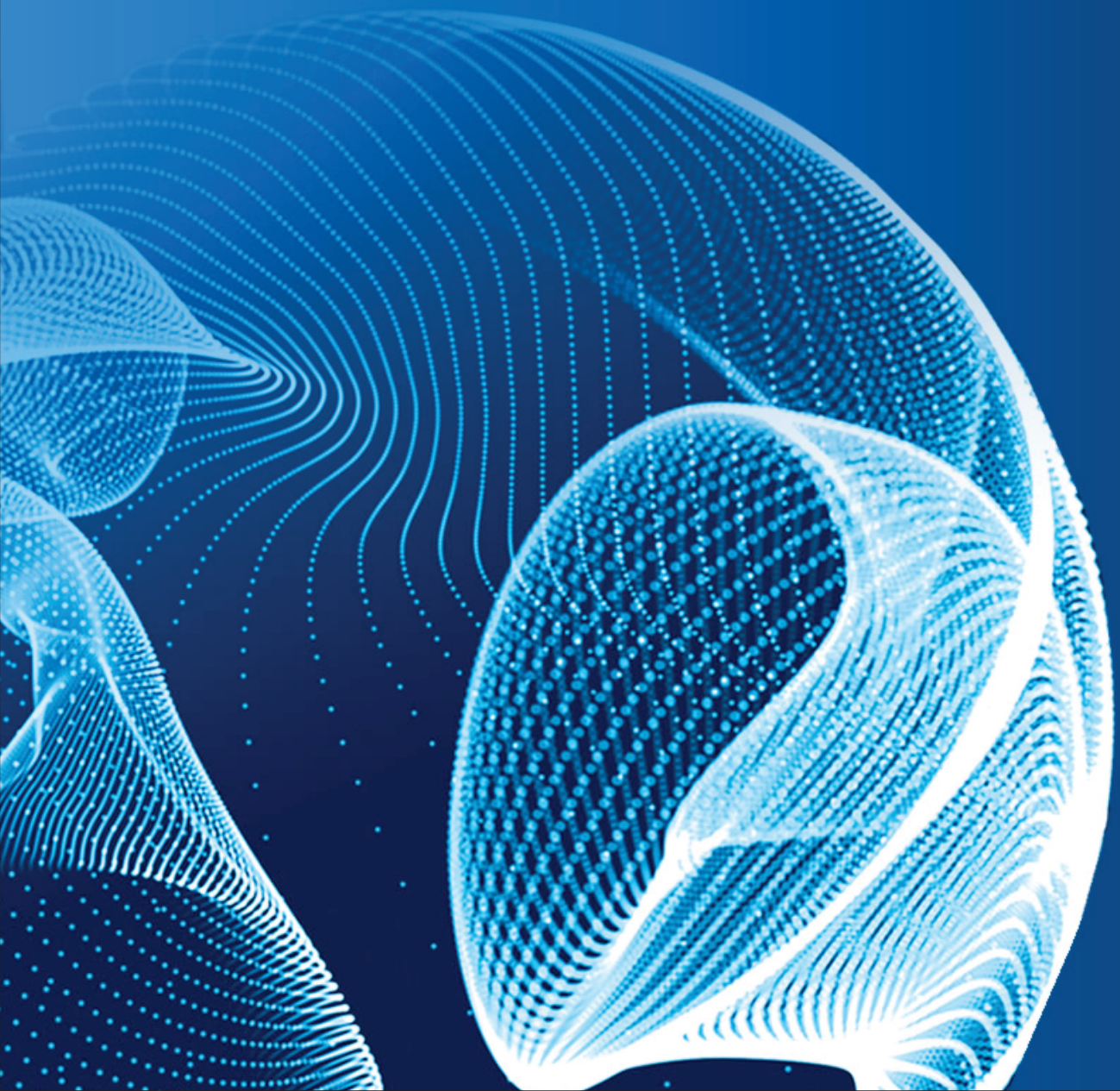

eISSN 2959-2348

eISSN 2959-2348

eISSN 2959-2348

SATBAYEV UNIVERSITY

Engineering Journal of Satbayev University

Volume 148 (2026), Issue 1, 1-7

https://doi.org/10.51301/ejsu.2026.i1.01

A small-sized continuous reactor system for extracting nickel, cobalt and iron from stale tailings

A.T. Khabiyev[1], S. Dilibal[2], A.N. Mussulmanbekova[1], M.O. Kanapiya[1], Ye.S. Merkibayev[3*]

[1]*U.A. Joldasbekov Institute of Mechanics and Engineering, Almaty, Kazakhstan*
[2]*Istanbul Gedik University, Istanbul, Turkey*
[3]*International Educational Corporation, Almaty, Kazakhstan*
**Corresponding author: Erik_me@mail.ru*

Abstract. The increasing accumulation of stale tailings from mining operations poses both environmental risks and opportunities for the recovery of valuable metals. This study focuses on the development, additive manufacturing, and experimental validation of a small-scale continuous reactor system for the extraction of nickel, cobalt, and iron from stale pyrite tailings at the Sokolovsko-Sarbaisky Mining and Processing Plant (Kazakhstan). The reactor system was fabricated using additive manufacturing (3D printing) with PET-G polymer, allowing for rapid prototyping, modular assembly, chemical resistance, and cost-effective production. The system comprises three sequentially connected reactors operating in continuous flow. Reagent and slurry feeding were conducted using peristaltic pumps, while a stepper-motor-driven mechanical stirrer ensured homogeneous mixing. Temperature was controlled by circulating a heat-transfer fluid through integrated heat-exchange channels, enabling stable operation over 20-120°C. Before leaching, stale tailings were subjected to oxidative roasting in a fluidized-bed furnace at 650-700°C for 1 hour, which facilitated the decomposition of sulfides into oxides. Subsequent leaching experiments were conducted with sulfuric acid concentrations ranging from 25 to 175 g/dm^3, varying residence times, and controlled thermal conditions. Optimal parameters were established as 100 g/dm^3 H_2SO_4, 100°C, and 120 minutes, resulting in recoveries of 93.01% for Ni and 91.49% for Co, with moderate Fe dissolution of 64.4%. The results confirm that the designed continuous reactor system provides reproducible hydrometallurgical performance, stable process control, and scalability potential. This approach highlights the combined advantages of continuous-flow chemistry and additive manufacturing in processing low-grade, environmentally challenging raw materials.

Keywords: *continuous reactor; additive manufacturing; nickel; cobalt; iron; leaching; stale tailings; hydrometallurgy.*

Received: 17 September 2025
Accepted: 14 February 2026
Available online: 28 February 2026

1. Introduction

The global mining industry plays a pivotal role in supplying raw materials that underpin modern technologies, from energy storage devices and renewable energy infrastructure to advanced alloys and everyday consumer products. However, alongside the production of concentrates and metals, mining and mineral processing operations generate enormous amounts of waste, particularly tailings. These fine-grained residues are usually stored in impoundments or waste dumps, which pose long-term environmental and social challenges. Tailings storage facilities have been associated with catastrophic dam failures, leaching of toxic elements, dust emissions, and land occupation. At the same time, tailings frequently contain appreciable amounts of valuable metals that were not fully recovered during initial processing due to technological or economic limitations at the time [1].

Kazakhstan, as one of the major producers of iron ore, copper, and polymetallic ores, faces similar challenges. The Sokolovsko-Sarbaisky Mining and Processing Plant (SSGPO) is among the largest producers of iron ore in the country. Over the course of its decades-long operation, it has generated substantial volumes of tailings that have become stale. These tailings contain residual concentrations of nickel (Ni), cobalt (Co), and iron (Fe), along with associated gangue minerals. Historically, the recovery of Ni and Co was not prioritized in such operations, leading to their accumulation in waste storage. As global demand for Ni and Co increases, particularly due to their role in lithium-ion batteries and clean energy technologies, the reprocessing of stale tailings becomes both a strategic and environmentally necessary initiative [2].

Hydrometallurgy has long been recognized as a viable method for extracting metals from low-grade ores, concentrates, and secondary raw materials. Compared to pyrometallurgical methods, hydrometallurgical processes generally operate at lower temperatures, produce fewer gaseous emissions, and allow for selective recovery of metals through leaching, solvent extraction, and ion exchange [3]. Sulfuric acid is the most widely used leaching reagent for Ni and Co, especially when combined with oxidative pretreatments.

alibek1324@inbox.ru; savas.dilibal@gedik.edu.tr; tuaimeasel@mail.ru; magzhan9897@gmail.com; Erik_me@mail.ru
Engineering Journal of Satbayev University. eISSN 2959-2348. Published by Satbayev University

Oraby et al. [1] demonstrated that flotation tailings rich in Ni and Co sulfides could be successfully processed using glycine–ammonia systems, achieving metal recoveries above 85-90%. Likewise, sulfuric acid leaching is effective for metallurgical slags, with hydrogen peroxide serving as an auxiliary oxidant to enhance dissolution of Ni and Co [2].

Pretreatment is often essential to improve the solubility of refractory minerals. Roasting transforms sulfides, silicates, and refractory oxides into more leachable forms. Reduction roasting, in particular, has been applied to oxidized nickel ores, with temperatures between 400 and 850°C resulting in nearly complete Ni recovery after sulfuric acid leaching [3]. In the case of cobalt-bearing pyrite, oxidative roasting reduced sulfur content and facilitated Co recovery by producing soluble oxide phases [4]. Such approaches demonstrate that a combination of thermal and hydrometallurgical processes is necessary to achieve efficient extraction from complex tailings.

Despite the maturity of hydrometallurgical techniques, most laboratory and pilot studies rely on batch systems, which present limitations in scalability, reproducibility, and process control. Continuous flow systems address these challenges by maintaining steady-state conditions, reducing reagent fluctuations, and enabling tighter control of temperature, pH, and residence time. Panda et al. [5] reviewed the hydrometallurgical recovery of valuable metals from industrial wastes, highlighting the advantages of continuous processes in terms of efficiency and energy consumption. Continuous stirred-tank reactors (CSTRs), plug-flow reactors, and tubular reactors have been successfully applied in copper heap leaching, rare earth element recovery, and nickel hydrometallurgy, yielding improved yields and reduced reagent use compared to batch operations.

Parallel to advances in process engineering, new approaches to equipment design are reshaping laboratory-scale experimentation. Additive manufacturing, commonly known as 3D printing, has emerged as a disruptive technology that enables the rapid fabrication of complex geometries, modular components, and chemically resistant reactors at a relatively low cost. Kitson et al. [6] introduced the concept of “reactionware”, demonstrating how 3D-printed reactors could be configured as modular flow systems for organic synthesis. Beauchamp et al. [7] extended these concepts to photochemical reactions, highlighting the ability of 3D-printed reactors to control reaction pathways and to enable scale-up. Moreover, the article's author designed and utilized a reactor system to produce metronidazole derivatives [8].

The advantages of 3D printing for reactor design are manifold. First, rapid prototyping enables researchers to test and refine designs quickly, eliminating the need for expensive machining. Second, features such as mixing chambers, heat exchangers, or sensor channels can be directly embedded into the printed structure, eliminating the need for post-processing. Third, new materials such as PET-G, polypropylene, and polymer–ceramic composites provide resistance to acidic and oxidative environments [9, 10]. Nordin et al. [9] fabricated corrosion-resistant 3D-printed microfluidic devices for electrochemical studies, demonstrating their durability under aggressive chemical conditions. Liravi and Toyserkani [10] reported on polymer–ceramic composites tailored for additive manufacturing of chemical reactors, enabling operation under harsher conditions than conventional polymer devices.

While applications of 3D-printed reactors in hydrometallurgy are still rare, examples from related fields illustrate their potential. Chisholm et al. [11] designed 3D-printed reactors for nanoparticle synthesis, achieving precise size control unattainable in conventional batch reactors. Chen et al. [12] developed 3D-printed flow reactors for polymer synthesis, demonstrating reproducibility and scalability. These studies suggest that additive manufacturing can bridge the gap between laboratory research and industrial applications by offering modular, adaptable reactor systems.

Integrating additive manufacturing with continuous hydrometallurgical processing creates a powerful synergy. Continuous operation provides process stability and scalability, while 3D printing ensures flexibility, cost reduction, and rapid design iteration. This integration is particularly promising for the treatment of low-grade ores and stale tailings, where conventional equipment may be too costly or inflexible. Furthermore, compact 3D-printed reactors are well-suited for decentralized operations, enabling in situ processing at mine sites and reducing transportation of hazardous wastes.

The present research seeks to explore this intersection by developing a small-scale, continuous reactor system fabricated via 3D printing and applying it to the recovery of Ni, Co, and Fe from stale tailings of the Sokolovsko-Sarbaisky Mining and Processing Plant. The study involves designing reactor modules with integrated mixing and heating, applying oxidative roasting as pretreatment, and optimizing sulfuric acid leaching conditions. The outcomes are expected to demonstrate not only the feasibility of additive manufacturing in hydrometallurgy but also its potential to provide scalable, sustainable solutions for tailings reprocessing.

2. Materials and methods

2.1. Raw materials and reagents

As the feedstock, a roasted pyrite concentrate was used, obtained from the stale tailings of the Sokolovsko-Sarbaisky Mining and Processing Plant (SSGPO, Kazakhstan). The material contained mainly iron oxides and sulfides with minor amounts of nickel (0.10 wt.%) and cobalt (0.21 wt.%). Sulfuric acid (H_2SO_4, analytical grade) was applied as the primary leaching reagent in concentrations ranging from 25 to 175 g/dm^3. All chemicals used in the experiments were of analytical purity (“hch”, “chda”, “osch”) and suitable for spectroscopic analysis. Deionized water was used to prepare all solutions.

2.2. Design and additive manufacturing of the continuous reactor system

2.2.1. Design of the reactor system

The system consists of three reactors (Figure 1) connected in series, operating in continuous flow mode. Feeding of solid and liquid reagents was carried out using peristaltic pumps, and a stepper motor-driven mechanical stirrer ensured thorough mixing. Temperature control was achieved by circulating a heat-transfer fluid through integrated channels within the reactor body, enabling stable operation over a range of 20 to 120°C. The configuration enables the continuous introduction of leaching solution and tailings slurry, efficient mixing, and collection of the product solution.

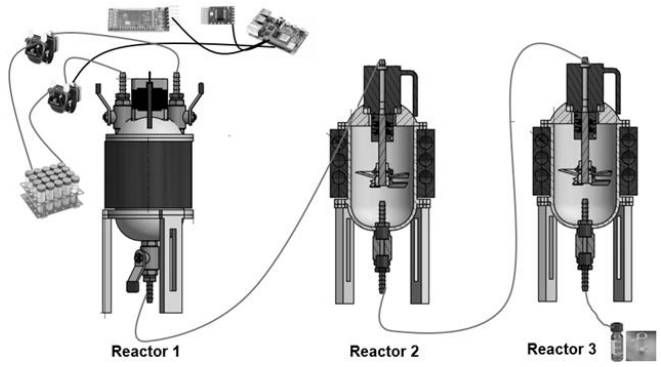

Figure 1. Design of a continuous reactor system for extracting nickel and cobalt from stale tailings

In Reactor 1, roasted pyrite concentrate and a sulfuric acid solution are introduced into the system via peristaltic pumps, where initial mixing and slurry preparation occur under controlled temperature and agitation conditions. Reactor 2 serves as the central unit for acid leaching, equipped with a mechanical stirrer to ensure homogeneous mixing and with integrated heat-exchange elements to maintain a stable thermal regime. Reactor 3 represents the final stage of the process, where leaching reactions are completed, yielding a pregnant solution containing nickel and cobalt ions, which is collected in vials for further analysis and separation.

2.2.2. Additive manufacturing of the reactor system

A small, continuous reactor system for extracting nickel and cobalt from stale tailings was designed and manufactured using additive manufacturing (3D printing). The reactor body, lid, stand, stirrer, and heat-exchanger elements were fabricated from PET-G polymer on a Bambu Lab X1 3D printer. Printing parameters were set as follows: nozzle temperature 240-250°C, bed temperature 70-80°C, layer height 0.2-0.28 mm, and infill density 20-40%. After printing, the supports were removed, the surfaces were cleaned, and the parts were assembled into a modular reactor unit.

2.2.3. Manufacturing of the reactor components

The manufacturing of reactor system components (reactor lid, stand, reactor body, heat exchanger elements, and stirrer) is carried out as follows (Figure 2). At the initial stage, 3D models of all parts are designed in CAD software, taking into account their structural features, and then exported in STL or 3MF format.

Figure 2. AM-based reactor components (main body with heat exchanger and mixer)

The reactor body, lid, stand, stirrer, and heat-exchanger elements were fabricated from PET-G polymer on a Bambu Lab X1 3D printer.

Next, printing parameters are set in Bambu Studio: extruder temperature 240-250°C, bed temperature 70-80°C, layer height 0.2-0.28 mm, infill density 20-40%, and printing speed 80-120 mm/s. Supports are enabled for parts with overhanging elements (such as the lid and stand), and a brim is applied to improve bed adhesion.

After loading the PET-G filament into the printer, automatic calibration is performed, and printing begins. The reactor body is produced as a cylindrical part with uniform cooling to prevent warping, the lid is printed with supports and mounting holes, the stand with vertical columns is printed at a lower speed for stability, the stirrer is manufactured as a separate part to be later connected to a stepper motor and controller, and the heat exchanger elements are produced with high precision to ensure tight connections.

After printing, post-processing is performed, including support removal, surface cleaning, and optional sanding or heat treatment to smooth the layers (Figure 3).

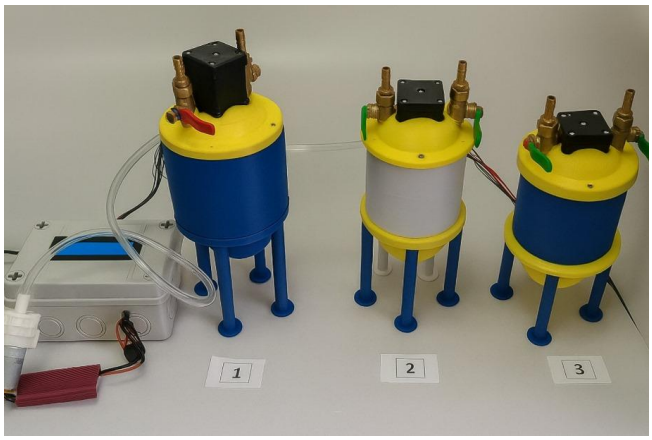

Figure 3. AM-based continuous processing reactor system for the extraction of nickel and cobalt from stale tailings (1, 2 and 3 indicate the numbers of the respective reactors)

All parts are checked for dimensional accuracy, then assembled into a single structure: the body is fixed to the stand and lid with bolts, the stirrer is mounted and connected to a stepper motor via a controller for mixing operations, and the heat exchanger elements are installed. Cooling and heating of the reactor are achieved by circulating liquid through the system using peristaltic pumps.

2.3 Roasting and leaching procedure

Before leaching, the stale tailings were subjected to oxidative roasting in a fluidized bed furnace at 650-700°C for 60 minutes with an oxygen-enriched air supply (15% O_2). The obtained calcine was cooled and fed into the continuous reactor system for sulfuric acid leaching.

Leaching was carried out at a solid-to-liquid (S/L) ratio of 1:2, with the slurry continuously circulated through the three-stage reactor unit. Process parameters included acid concentration of 25-175 g/dm^3, temperature range of 20-120°C, and residence times of 15-240 minutes. Optimal leaching conditions were determined as 100 g/dm^3 H_2SO_4, 100°C, and 120 min, under which the maximum extractions of Ni and Co reached 93.01% and 91.49%, respectively.

2.4 Analytical methods

Titrimetric and spectrometric methods were used to determine the chemical composition of solid residues and leach solutions. The phase composition of the roasted samples was analyzed by X-ray diffraction (D8 Advance, Bruker) using Cu Kα radiation (40 kV, 30 mA). The pH of the solutions was monitored using a pH-150MP pH meter with standard electrodes. Thermodynamic calculations and Pourbaix diagrams for the Ni–S–H2O and Co–S–H2O systems were generated using the Outotec HSC Chemistry 5 software package.

3. Results and discussion

The small-sized continuous reactor system fabricated via additive manufacturing was tested for the extraction of nickel and cobalt from roasted stale tailings of the Sokolovsko-Sarbaisky Mining and Processing Plant (SSGPO, Kazakhstan). The experimental work demonstrated that continuous leaching provides stable operating conditions, adequate mixing, and reproducible recovery of valuable metals.

3.1 Effect of sulfuric acid concentration

The concentration of sulfuric acid has a decisive effect on the leaching behavior of nickel, cobalt, and iron from thermally decomposed pyrite concentrate. Figure 4 shows the dependence of the extraction of Ni, Co, and Fe on the concentration of H_2S_4.

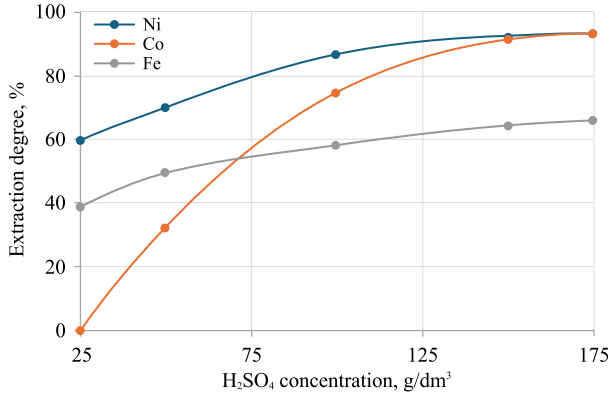

Figure 4. Dependence of the extraction of Ni, Co, and Fe on the concentration of H_2SO_4

At a low H_2SO_4 concentration of 25 g/dm^3, nickel extraction reaches about 59.6%, cobalt extraction is initially negligible, while iron extraction is around 39.1%. Increasing the acid concentration to 50 g/dm^3 enhances nickel recovery to 70.0%, cobalt to 32.5%, and iron to 50.0%. A pronounced improvement is observed in the 100-150 g/dm^3 range, where nickel extraction increases to 86.7-92.0%, cobalt to 75.0-91.5%, and iron to 58.0-64.4%.

Further increasing the acid concentration up to 175 g/dm^3 results in a saturation effect: Ni and Co recoveries reach about 93%, while Fe extraction increases only slightly to 66.0%. Thus, the optimal acid concentration lies in the range of 100-150 g/dm^3, ensuring maximum recoveries of nickel and cobalt while maintaining moderate iron dissolution. This creates favorable conditions for subsequent selective separation of the target metals, followed by solvent extraction or precipitation.

3.2 Effect of leaching time

The effect of leaching time on the dissolution of nickel, cobalt, and iron from roasted stale tailings was investigated over a range of 5-240 minutes. Figure 5 shows the time dependence of the extraction of Ni, Co, and Fe.

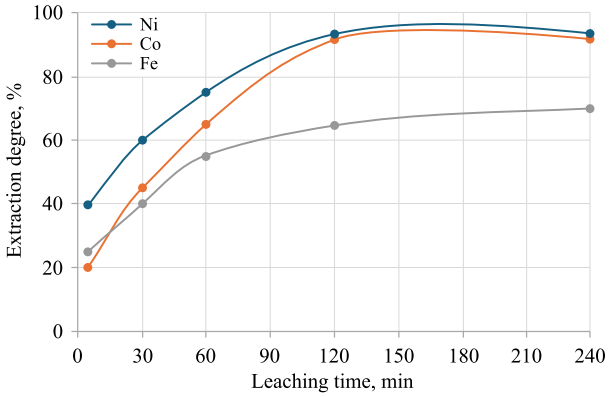

Figure 5. Dependence of the extraction of Ni, Co, and Fe on leaching time

The results show that nickel extraction increases rapidly from 40% at 5 minutes to 75% at 60 minutes, reaching a maximum of 93.0% at 120 minutes. After this, only a slight increase to 93.5% is observed at 240 minutes, indicating that equilibrium has been reached. Cobalt follows a similar trend, with lower initial rates: 20% at 5 minutes, increasing to 65% at 60 minutes. At 120 minutes, the maximum extraction of 91.5% is achieved, with only marginal improvement to 92% at 240 minutes. Iron dissolution is a gradual and continuous process, increasing from 25% at 5 minutes to 64.4% at 120 minutes, and reaching 70% at 240 minutes. These results indicate that the optimal leaching time is 120 minutes, at which nickel and cobalt recoveries exceed 91% while iron dissolution remains moderate. Prolonged leaching beyond this time provides no significant improvement in Ni and Co extraction but increases Fe dissolution, thereby complicating downstream purification and separation processes.

3.3 Effect of temperature

The effect of temperature on the extraction of nickel, cobalt, and iron from roasted stale tailings was investigated in the range of 20-120°C. Figure 6 shows the temperature dependence of the extraction of Ni, Co, and Fe.

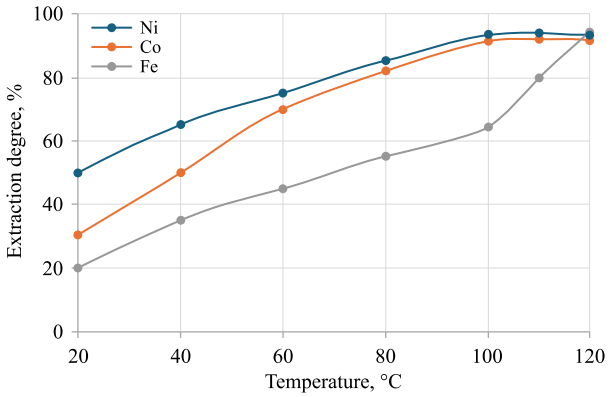

Figure 6. Dependence of the extraction of Ni, Co, and Fe on temperature

At low temperatures (20-40°C), nickel and cobalt recoveries were limited to 50-65% and 30-50%, respectively, while iron dissolution remained at 20-35%. Increasing the temperature to 60-80°C significantly enhanced metal recovery, with nickel extraction rising to 75-85%, cobalt to 70-82%, and iron to 45-55%. The maximum recoveries of nickel (93.0%) and cobalt (91.5%) were achieved at 100°C, accompanied by moderate iron dissolution of 64.4%. Further temperature increases to 110-120°C resulted in only marginal improvements in nickel and cobalt extraction (up to 93.3% and 92.2%, respectively), but were accompanied by a sharp rise in iron dissolution, ranging from 80% to 94.2%. These results indicate that the optimal leaching temperature lies between 100 and 110°C, where high recoveries of nickel and cobalt are achieved while maintaining iron dissolution at a manageable level. Exceeding this temperature range reduces process selectivity and complicates downstream purification due to excessive iron content in the pregnant solution.

4. Conclusions

The study successfully demonstrated the feasibility of fabricating a small-scale continuous reactor system by additive manufacturing (3D printing) and applying it to the hydrometallurgical recovery of nickel, cobalt, and iron from stale tailings of the Sokolovsko-Sarbaisky Mining and Processing Plant.

Pretreatment of the tailings by oxidative roasting significantly improved the subsequent acid leaching efficiency. The optimal operating conditions 100 g dm^{-3} H_2O_4, 100 °C, and 120 min of residence time yielded recoveries of 93.0 % Ni and 91.5 % Co with moderate Fe dissolution (64.4 %). These results confirm the efficiency of combining thermal pretreatment with continuous sulfuric acid leaching. The research also demonstrated the practical advantages of additive manufacturing for the design of laboratory-scale hydrometallurgical equipment. The modular and cost-efficient 3D-printed system enables rapid prototyping, integration of multifunctional components, and straightforward scaling to pilot-plant operations.

Overall, the findings demonstrate that combining continuous-flow hydrometallurgy with additive manufacturing presents a sustainable technological approach for processing low-grade ores and tailings, promoting efficient resource utilization and minimizing environmental impact.

Author contributions

Conceptualization: SD; Data curation: ATK; Formal analysis: YSM; Funding acquisition: MOK; Investigation: MOK; Methodology: ATK; Project administration: ATK; Resources: ATK; Software: YSM; Supervision: YSM; Validation: ANM; Visualization: ATK; Writing – original draft: ATK; Writing – review & editing: SD. All authors have read and agreed to the published version of the manuscript.

Funding

This research was funded by the Science Committee of the Ministry of Science and Higher Education of the Republic of Kazakhstan, grant number AP22783377.

Acknowledgements

The authors express their sincere gratitude to the editor and anonymous reviewers for their constructive comments and valuable suggestions, which have significantly improved the quality of this manuscript.

Conflicts of interest

The authors declare no conflict of interest.

Data availability statement

The original contributions presented in this study are included in the article. Further inquiries can be directed to the corresponding author.

References

[1] Oraby, E., Deng, Z., Li, H. & Eksteen, J. (2023). Selective extraction of nickel and cobalt from disseminated sulfide flotation cleaner tailings using alkaline glycine–ammonia leaching solutions. *Minerals Engineering*, 204, 108418. https://doi.org/10.1016/j.mineng.2023.108418

[2] Lou, Y., Tang, X., Liu, C. & Zhang, W. (2023). Optimizing the Leaching Parameters and Studying the Kinetics of Nickel and Cobalt Recovery from Xinjiang Nickel–Cobalt Slag. *JOM*, *75*, 381-391. https://doi.org/10.1007/s11837-022-05530-7

[3] Khasanov, M.S., Sadykhov, G.B., Anisonyan, K.G., Zablotskaya, Y.V. & Olyunina, T.V. (2022). Effect of the Temperature of Reduction Roasting of Ferriferous Oxidized Nickel Ores on the Nickel and Cobalt Recovery during Hydrometallurgical Processing of a Cinder. *Russian Metallurgy (Metally)*, *7*, 714-718. https://doi.org/10.1134/S0036029522070059

[4] Urtnasan, E., Kumar, A., & Wang, J.P. (2024). Correlation between Thermodynamic Studies and Experimental Process for Roasting Cobalt-Bearing Pyrite. *Metals*, *14*(7), 777. https://doi.org/10.3390/met14070777

[5] Huang, F., Liao, Y., Zhou, J., Wang, Y. & Li, H. (2015). Selective recovery of valuable metals from nickel converter slag at elevated temperature with sulfuric acid solution. *Separation and Purification Technology*, *156*, 572-581. https://doi.org/10.1016/j.seppur.2015.10.051

[6] Kitson, P.J., Rosnes, M. H., Sans, V., Dragone, V. & Cronin, L. (2012). Configurable 3D-printed millifluidic and microfluidic 'lab on a chip' reactionware devices. *Lab on a Chip*, *12*(18), 3267–3271. https://doi.org/10.1039/C2LC40761B

[7] Nielsen, A.V., Beauchamp, M.J., Nordin, G.P. & Woolley, A.T. (2020). 3D printed microfluidics. *Annual Review of Analytical Chemistry, 13(1),* 45-65. https://doi.org/10.1146/annurev-anchem-091619-102649

[8] Khabiyev, A., Dilibal, S., Mussulmanbekova, A., Kanapiya, M. & Kerimkulov, D. (2024). Additively Manufactured Continuous Processing Reactor System for Producing Liquid-Based Pharmaceutical Substances. *Applied Sciences*, *14*(16), 6853. https://doi.org/10.3390/app14166853.

[9] Kumar, A. (2019). Classification of challenges in 3D printing for combined electrochemical and microfluidic applications: a review. *Rapid Prototyping Journal*, *25*(7), 1328-1346. https://doi.org/10.1108/RPJ-05-2018-0115

[10] Liravi, F. & Toyserkani, E. (2018). Additive manufacturing of polymer–ceramic composites for chemical reactor applications. *Journal of Materials Processing Technology*, *252*, 624-630. https://doi.org/10.1016/j.jmatprotec.2017.10.038

[11] Lignos, I., Ow, H., Lopez, J.P., McCollum, D.A., Zhang, H., Imbrogno, J., & Jensen, K.F. (2020). Continuous multistage synthesis and functionalization of sub-100 nm silica nanoparticles in 3D-printed continuous stirred-tank reactor cascades. *ACS applied materials & interfaces*, *12*(5), 6699-6706. https://doi.org/10.1021/acsami.9b20605

[12] Maier, M. C., Valotta, A., Hiebler, K., Soritz, S., Gavric, K., Grabner, B. & Gruber-Woelfler, H. (2020). 3D printed reactors for synthesis of active pharmaceutical ingredients in continuous flow. *Organic Process Research & Development*, *24*(10), 2197-2207. https://doi.org/10.1021/acs.oprd.0c00228

Ескірген қалдықтардан никель, кобальт және темір алуға арналған шағын көлемді үздіксіз реакторлық жүйе

А.Т. Хабиев[1], С. Дилибал[2], А.Н. Мусулманбекова[1], М.О. Канапия[1], Е.С. Меркибаев[3*]

[1]*Ө.А. Жолдасбеков атындағы Механика және машинатану институты, Алматы, Қазақстан*
[2]*Ыстамбұл Гедик университеті, Стамбул, Түркия*
[3]*Халықаралық білім беру корпорациясы, Алматы, Қазақстан*

**Корреспонденция үшін автор: Erik_me@mail.ru*

Аңдатпа. Тау-кен жұмыстарынан ескірген қалдықтардың жинақталуының артуы экологиялық тәуекелдерді де, бағалы металдарды қалпына келтіру мүмкіндіктерін де тудырады. Бұл зерттеу Соколов-Сарыбай Тау-Кен Байыту комбинатының (Қазақстан) ескірген пирит қалдықтарынан никель, кобальт және темір өндіруге арналған шағын көлемді үздіксіз реакторлық жүйені әзірлеуге, қоспаларды өндіруге және тәжірибелік тексеруге бағытталған. Реактор жүйесі жылдам прототиптеуге, модульдік құрастыруға, химиялық төзімділікке және үнемді өндіріске мүмкіндік беретін PET-G полимерімен қоспа өндірісін (3d басып шығару) пайдалана отырып жасалған. Жүйе үздіксіз ағын жағдайында жұмыс істейтін бірізді қосылған үш реактордан тұрады. Реагенттер мен суспензияларды беру перистальтикалық сорғылардың көмегімен жүзеге асырылды, ал біртекті араластыру сатылы қозғалтқышпен басқарылатын механикалық араластырғышпен қамтамасыз етілді. Температура 20-120°C аралығында тұрақты жұмыс Істеуге Мүмкіндік Беретін интеграцияланған жылу алмасу арналары Арқылы жылу тасымалдағыш сұйықтықты айналдыру Арқылы бақыланды. Шаймалау алдында ескірген қалдықтар бір сағат ішінде 650-700°C температурада сұйық төсек пешінде тотықтырғыш қуыруға ұшырады, бұл сульфидтердің оксидтерге ыдырауын жеңілдетті. Кейінгі шаймалау тәжірибелері күкірт қышқылының концентрациясы 25-175 г/дм^3, әр түрлі тұру уақыты және бақыланатын жылу жағдайлары бойынша жүргізілді. Оңтайлы параметрлер 100 г/дм^3 H_2SO_4, 100°C және 120 минут ретінде белгіленді, нәтижесінде Ni үшін 93.01% және Co үшін 91.49% қалпына келтірілді, Орташа Fe еруі 64.4% болды.%. Нәтижелер жобаланған үздіксіз реактор жүйесі қайталанатын гидрометаллургиялық өнімділікті, процесті тұрақты басқаруды және масштабталатын әлеуетті қамтамасыз ететінін растайды. Бұл тәсіл төмен сұрыпты және экологиялық тұрғыдан күрделі шикізатты өңдеуде үздіксіз ағынды химия мен қоспаларды өндірудің біріктірілген артықшылықтарын көрсетеді.

Негізгі сөздер: *үздіксіз реактор; қоспалар өндірісі; никель; кобальт; темір; сілтілеу; ескірген қалдықтар; гидрометаллургия.*

Малогабаритная реакторная система непрерывного действия для проведения извлечения никеля, кобальта и железа из лежалых хвостов

А.Т. Хабиев[1], С. Дилибал[2], А.Н. Мусулманбекова[1], М.О. Канапия[1], Е.С. Меркибаев[3*]

[1]*Институт механики и машиноведения имени академика У.А. Джолдасбекова, Алматы, Казахстан*
[2]*Стамбульский Гедик университет, Стамбул, Турция*
[3]*Международная образовательная корпорация, Алматы, Казахстан*

**Автор для корреспонденции: Erik_me@mail.ru*

Аннотация. Растущее накопление залежалых хвостов горных работ создает как экологические риски, так и возможности для извлечения ценных металлов. Данное исследование посвящено разработке, аддитивному производству и экспериментальной проверке малогабаритной реакторной установки непрерывного действия, предназначенной для извлечения никеля, кобальта и железа из отработанных пиритных хвостов Соколовско-Сарбайского горно-обогатительного комбината (Казахстан). Реакторная система была изготовлена с использованием технологии аддитивного производства (3D-печати) с использованием полимера PET-G, что обеспечивает быстрое создание прототипов, модульную сборку, химическую стойкость и экономичное производство. Система состоит из трех последовательно соединенных реакторов, работающих в режиме непрерывного потока. Подача реагентов и суспензии осуществлялась с помощью перистальтических насосов, а однородное перемешивание обеспечивалось механической мешалкой с шаговым приводом. Температура регулировалась путем циркуляции теплоносителя по встроенным теплообменным каналам, что обеспечивало стабильную работу в диапазоне 20-120°C. Перед выщелачиванием залежалые хвосты подвергали окислительному обжигу в печи с псевдоожиженным слоем при температуре 650-700°C в течение одного часа, что способствовало разложению сульфидов на оксиды. Последующие эксперименты по выщелачиванию проводились

с концентрациями серной кислоты 25-175 г/дм^3, различным временем выдержки и контролируемыми тепловыми режимами. Были установлены оптимальные параметры: 100 г/дм^3 H_2SO_4, 100°C и 120 минут, в результате чего степень извлечения Ni составила 93.01%, Co – 91.49%, при умеренном растворении Fe – 64.4%. Результаты подтверждают, что разработанная система реакторов непрерывного действия обеспечивает воспроизводимые гидрометаллургические характеристики, стабильное управление процессом и возможность масштабирования. Такой подход подчеркивает преимущества непрерывного химического процесса и производства добавок при переработке низкосортного и экологически опасного сырья.

Ключевые слова: *реактор непрерывного действия; аддитивное производство; никель; кобальт; железо; выщелачивание; отработанные хвосты; гидрометаллургия.*

Publisher's note

All claims expressed in this manuscript are solely those of the authors and do not necessarily represent those of their affiliated organizations, or those of the publisher, the editors and the reviewers.

SATBAYEV UNIVERSITY

Engineering Journal of Satbayev University

Volume 148 (2026), Issue 1, 8-15

https://doi.org/10.51301/ejsu.2026.i1.02

Research into the ternary-remelted alloy Ti-10V-2Fe-3Al structural and technological properties

A.T. Mamutova[1], T.A. Chepushtanova[2*], B. Mishra[3]

[1]*Ust-Kamenogorsk Titanium and Magnesium Plant JSC, Ust-Kamenogorsk, Kazakhstan*
[2]*Satbayev University, Almaty, Kazakhstan*
[3]*Worcester Polytechnic Institute, Worcester, USA*

**Corresponding author: t.chepushtanova@satbayev.university*

Abstract. This paper presents the results of producing a triple-remelted Ti-10V-2Fe-3Al alloy. The results of SEM–EDS analysis of the alloy are reported, and the structure of the Ti-10-2-3 alloy along the height of an industrial electrode is determined. For the first time, results of a direct comparison between the morphology of the *α/β* phases and the local chemical composition in three characteristic zones of a 4.5 t electrode, "top", "middle 1", "middle 2", and "bottom", are obtained based on comprehensive SEM–EDS analysis. It is established that, with respect to the main alloying elements (Ti, Al, V), the ingot is fully chemically homogenized along its height, and the VAR (vacuum arc remelting) regime ensures an acceptable level of macrosegregation. It is shown that the concentrations of (Ti, Al, V), the principal alloying elements in Ti-10V-2Fe-3Al, do not change significantly between samples. SEM–EDS results indicate that the scatter in elemental concentrations is ≤1-1.5%, which is considered an indicator of high-quality VAR processing; this level of scatter implies minimal differences in elemental concentrations: Al variations are within ±0.5-1.0%, V variations are within ±0.5-1.0%, and Ti maintains a stable fraction of approximately ~83-86%. Morphological studies reveal that the *α/β* structure is formed uniformly, without pronounced columnar segregation. The results of the direct comparison of *α/β*-phase morphologies enabled the development of a quality-control methodology for electrodes based on SEM–EDS profiles.

Keywords: *titanium alloy; vacuum arc remelting; SEM–EDS analysis; triple remelting; α/β microstructure; morphology.*

Received: 18 November 2025
Accepted: 14 February 2026
Available online: 28 February 2026

1. Introduction

In recent years, research on titanium alloys has shifted toward detailed studies of the microstructural mechanisms that determine their performance characteristics, as well as the factors that affect the chemical homogeneity and phase state of industrially produced ingots. For the high-strength Ti-10V-2Fe-3Al (Ti-10-2-3) alloy, which belongs to the class of metastable *β*- and (*α*+*β*)-alloys, the distribution of alloying elements and the morphology of *α/β* phases after vacuum arc remelting (VAR) directly determine the strength, ductility, delamination resistance, and service life of critically loaded components. The primary methods for processing sponge titanium into ingots are vacuum arc remelting (VAR) and electron beam melting (EBM). These processes are the primary means of producing titanium alloys. VAR technology is widely used to improve the purity and structure of standard ingots, known as consumable electrodes, which are melted under vacuum.

Modern analytical approaches emphasize that not only the global chemical purity but also local microstructural inhomogeneities can significantly affect alloy properties. According to reviews on metastable *β*-alloys [1-4], even slight variations in the content of *β*-stabilizers (V, Fe), *α*-stabilizers (Al, O), or microsegregation of oxygen can lead to the formation of brittle zones, alter phase transformation kinetics, and cause the appearance of undesirable intermetallic phases, including α_2-Ti_3Al. Therefore, the importance of local analysis methods has increased in recent years, particularly scanning electron microscopy (SEM) combined with energy-dispersive spectroscopy (EDS), which enables the detection of micron- and submicron-scale structural inhomogeneities in industrially produced ingots.

A special focus within this group is the high-strength metastable *β*-alloy Ti-10V-2Fe-3Al (Ti-10-2-3), which has found wide application in chassis design, powertrain components, and integral fuselage assemblies due to its unique ability to achieve controlled *α*-phase morphology, regulated both by work hardening and aging regimes [5–7]. According to Banerjee & Williams [1] and Peters et al. [3] the mechanical properties of Ti-10-2-3 are determined by the distribution of *β*-stabilizers (V, Fe), the concentration of solid-solution elements in the *α*-phase (Al, O), the cooling rate, and the actual thermodynamic conditions of the *β*→*α* transformation.

Lutjering & Williams [2] and Boyer [8] emphasize that the spatial inhomogeneity of *β*-stabilizer distribution, local oxygen segregation, and *α/β* interphase morphology are critical parameters that determine fracture toughness, ductility, and the durability of highly loaded components.

post@uktmp.kz; t.chepushtanova@satbayev.university; bmishra@wpi.edu
Engineering Journal of Satbayev University. eISSN 2959-2348. Published by Satbayev University

Analyzing triple-melted ingots presents challenges, as a complex combination of factors influences structure formation: the composition and distribution of charge materials, solidification thermophysics, remelting conditions, and local temperature and heat flux variations. Large industrial electrodes weighing 4500 kg exhibit vertical and radial chemical gradients formed during ingot solidification, as well as differences in α/β-phase morphology between the top, middle, and bottom sections. These features are scarcely represented in the scientific literature: most publications focus either on laboratory melts or on structural analysis after heat treatment [9-12], while systematic SEM–EDS studies of large-scale, triple-melted industrial ingots are lacking.

The microstructure and performance characteristics of titanium alloys are determined by a set of phase transformations arising from titanium's pronounced polymorphism. Alloying elements introduced into titanium interact differently with the α- and β-phase lattices, stabilizing one modification over the other depending on changes in interatomic forces and their contributions to the thermodynamic stability of the phase states. This stability is defined by the polymorphic transformation temperature (PTT), a key parameter in the phase diagram of the Ti–X system [13].

Elements that predominantly dissolve in the α-phase, such as aluminum, oxygen, carbon, and nitrogen, increase the $\alpha\leftrightarrow\beta$ transformation temperature. Their presence leads to higher elastic moduli in the α solid solution and broadens its stability range. These elements, especially oxygen, nitrogen, and carbon, are inevitably introduced into the metal from both sponge titanium and alloying materials (C, Al) [14].

In contrast, β-type elements vanadium and iron lower the polymorphic transformation temperature, expanding the stability range of the β-phase. By dissolving in the β solid solution, they increase its elastic characteristics and promote the formation of a metastable β-matrix upon cooling. The transition of titanium atoms between β- and α-phases underlying these transformations is of particular interest.

Aluminum's low density reduces the alloy's specific weight and effectively increases its specific strength. It is a crucial α-stabilizer that provides strengthening while maintaining acceptable ductility. However, its content is limited by a critical threshold (~7 wt.%); exceeding this limit leads to the formation of the ordered intermetallic α_2-phase (Ti_3Al). The presence of this phase sharply reduces technological plasticity and impact toughness. To prevent α_2-phase formation, alloy compositions are optimized by limiting aluminum content and introducing β-stabilizers (Mo, V) [15].

Vanadium is the most versatile and widely used β-stabilizer in titanium alloys. Unlike other β-stabilizers, it simultaneously increases strength and ductility, making it unique among this group of elements. Its solubility in the α-phase reaches ~3%, allowing the development of alloys that combine the advantages of α-alloys (high weldability) and (α+β)-alloys (strengthening through heat treatment).

Oxygen, despite being an effective strengthener, significantly reduces ductility by forming a solid interstitial solution. At concentrations above ~0.2 wt.% and heating near the PTT, oxygen segregation at α-grain boundaries or the formation of fine α-phase particles enriched with oxygen may occur. These processes lead to a pronounced decrease in impact toughness and an increase in brittleness, consistent with [16-18].

Despite significant progress in theoretical modeling of β-alloys, data on the actual distribution of alloying elements and impurities in industrial triple-VAR ingots remain limited. Few studies provide a comprehensive correlation between α/β-structure morphology, chemical profiles, and local enrichment zones along the height of industrial-scale electrodes (mass 2.0-4.5 t), a crucial diagnostic aspect for ensuring VAR process stability and predicting the properties of the final semi-finished product.

This study aims to systematically investigate the structure and chemical homogeneity of an industrial Ti-10V-2Fe-3Al triple-VAR ingot using SEM–EDS, focusing on technologically induced inhomogeneities and identifying factors influencing α/β-microstructure formation along the electrode height.

2. Materials and methods

2.1. Initial materials

The object of this study was a triple-VAR Ti-10V-2Fe-3Al ingot, produced by vacuum arc remelting (VAR) according to the customer's specification: Al – 2.6-3.4%, V – 9.0-11.0%, Fe – 1.6-2.2%, O – max. 0.13%. The production of this ingot involved the following materials, whose chemical compositions are presented in Tables 1-5.

Table 1. Chemical composition of aluminum granules

Element	Al	Zn	Si	Fe	Mn	Mg	Ni	Pb	Sn	Ti	Cr	Cd	Be	Cu	C
Content, wt.%	99.8	0.003	0.025	0.113	0.02	0.0002	0.0051	0.001	0.0007	0.007	0.001	0.0001	0.0001	0.0004	0.002

Table 2. Chemical composition of the V–Al–Fe master alloy

Element	V	Al	Fe	B	C	Cr	Cu	Mo	P	S	Si	N	O
Content, wt.%	66.6	21.1	12.1	0.001	0.001	0.01	0.002	0.01	0.001	0.003	0.10	0.03	0.03

Table 3. Chemical composition of the V–Al–C alloy

Element	V	Al	B	C	Cr	Cu	Fe	Mn	Mo	Ni	P	S	Si	H	N	O
Content, wt.%	65.3	33.7	0.001	0.68	0.01	0.001	0.17	0.002	0.003	0.004	0.003	0.001	0.09	0.004	0.017	0.01

Table 4. Chemical composition of iron powder

Element	Fe	S	O(total)	N
Content, wt.%	99.98	0.003	0.019	0.001

Table 5. Chemical composition of titanium sponge

Element	Ti	Ni	Cl	O	N	Fe	C	Mn	Si	Mg	H	H_2O	Al	Sn	Cr	B
Content, wt.%	99.77	0.013	0.075	0.038	0.002	0.039	0.003	0.003	0.002	0.01	0.00062	0.01	0.005	0.002	0.017	0.001

2.2. Technology to produce titanium ingots in a vacuum arc remelting (VAR) furnace

The triple-VAR Ti-10V-2Fe-3Al alloy was produced on an industrial scale at Ust-Kamenogorsk Titanium and Magnesium Plant JSC. The VAR furnace configuration used for producing the Ti-10V-2Fe-3Al alloy is shown in Figure 1.

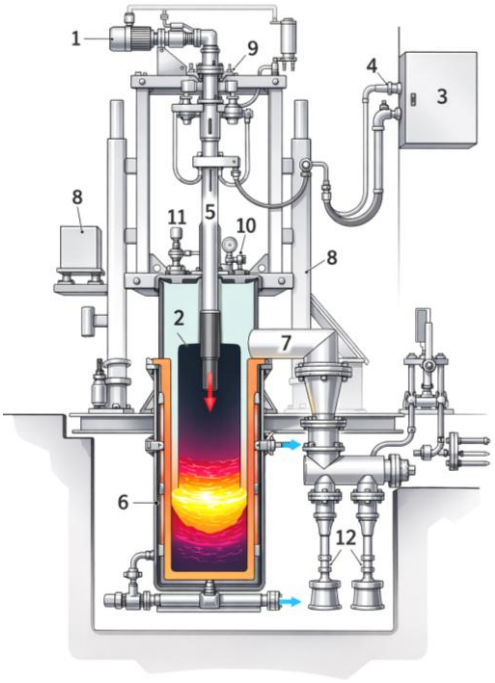

Figure 1. Schematic of the VAR furnace: 1 – electrode feed drive; 2 – furnace chamber; 3 – melting power supply; 4 – busbars and cables; 5 – plunger-type electrode holder; 6 – water-cooled jacket with mold (crucible); 7 – vacuum line; 8 – rotating column; 9 – coordinate positioning system; 10 – load cell system; 11 – TV camera system; 12 – oil booster pumps

During vacuum arc remelting (VAR), under the action of high temperatures generated in the electric arc zone between the consumable electrode and the base plate of the copper mold, the metal at the lower end of the electrode melts, and droplets of molten metal fall into the molten pool. Under the mold's cooling effect, an ingot is formed. Before the melting operation, the furnace chamber was evacuated, and vacuum was maintained throughout the melting process. Thus, molten metal droplets passed through a vacuum environment, ensuring deep purification of the metal from gases and certain nonferrous metal impurities and resulting in a dense ingot structure. Metal solidification in the water-cooled copper mold exhibited a clear directional character, aligned with the direction of heat removal. As a result of VAR, the mechanical properties of the metal improved and became more homogeneous in different directions of the ingot.

To reduce the risk of incorporating materials with excessively high or low density into the final product, the electrode holder was welded to the consumable electrode. The vacuum arc remelting process itself was carried out using separate melting assemblies. For this purpose, two molds were prepared: one intended for the electrode holder welding process and the other for the VAR process. Only molds and base plates that had undergone cleaning and drying procedures were used.

Using an overhead electric crane, the electrode holder was installed vertically at the upper end of the electrode, which was positioned in the melting assembly installed in the furnace. The electrode holder connected the ram (shaft) to the consumable electrode.

After furnace closure, the facility was evacuated. Leak testing was carried out in a computerized mode with data recorded in the process documentation. Upon reaching the specified vacuum parameters in the furnace chamber, a tight test was conducted.

The electrode holder was welded to the electrode by arc welding, forming an electric arc between the holder and the electrode's upper surface. Due to the arc energy, a molten titanium pool formed at the center of the electrode’s upper surface. Once enough liquid titanium had accumulated, the electrode holder was lowered using the electrode feed drive system and pressed into the molten pool. After solidification, a continuous welded joint was formed between the electrode holder and the electrode. This process was carried out under constant reduced pressure maintained by the VAR vacuum system.

After cooling the weld joint, the vacuum system was isolated from the furnace using appropriate vacuum valves, and atmospheric air was admitted into the furnace chamber.

The VAR operator loaded the starting material onto the bottom of the mold. This starting material was intended to protect the mold base plate from damage at the start of the melting process and was evenly distributed over the base plate, with a slight increase in thickness at the mold-base plate junctions. The furnace was then sealed and connected to the vacuum system.

The melting process was initiated from a remote control panel in the control room. Remelting process parameters were entered into the system.

During the melting process, monitored parameters were recorded in process logs every 20 minutes. A dedicated VAR operator performed monitoring and parameter adjustments at each processing stage.

After the melting was complete, the mold containing the ingot was removed from the furnace station using an overhead electric crane, transported to the assembly area, and placed on a special stand. The ingot obtained after remelting underwent dry cleaning of its lateral surface in a brushing machine. Subsequently, the ingot was transported to the “clean zone” of the machining area, where the crown was removed from the gating part on a lathe.

After crown removal, the ingot was subjected to high-pressure wet cleaning and drying in a washing unit designed for ingots and mold base plates. This stage completed the intermediate ingot processing procedure.

The electrode (first-remelting ingot) was installed with the gating part facing downward onto the base plate using an overhead crane. After installing the mold with the first remelting ingot into the melting station, the second remelting was performed. All subsequent processes associated with the second remelt vacuum evacuation, installation and welding of the electrode holder, preparation for melting, cooling, extraction, and mold washing were carried out following the same procedure as for the first remelt.

Surface treatment of titanium ingots was performed as a batch process in the machining area. Mechanical machining of the ingot end faces and lateral surfaces was performed on lathes. Machining was performed over the entire ingot surface until all surface irregularities and shrinkage cavities were removed entirely.

Sampling from titanium ingots was performed on a radial drilling machine by drilling using annular cutters. The number of samples, sampling locations, and dimensions of the sampling cones were determined in accordance with the applicable customer specification.

Sampling procedures, test methods, and testing volumes were conducted in accordance with the regulatory documentation for the product and the current technological and analytical control scheme. The quality, chemical composition, geometric dimensions, and weight of titanium ingots and alloys were required to comply with customer specifications.

The investigations employed scanning electron microscopy and elemental analysis using a JEOL JSM-7000 SEM equipped with EDS. Elemental composition was also determined by X-ray fluorescence analysis using an Olympus Element S XRF analyzer, and the alloys were chemically analyzed.

3. Results and discussion

3.1 Results of Ti-10V-2Fe-3Al alloy production

Vacuum arc remelting (VAR) of the Ti-10V-2Fe-3Al alloy was carried out in three successive remelts.

During the first remelt, the melted alloy mass (Δm) was 4.5 t, and the melting time (Δt) was 7 h 40 min. The electrode cross-sectional area (S_e) was 500 mm^2.

In the second remelt, Δm was 4.4 t and Δt was 10 h, with S_e equal to 600 mm^2.

The third remelt was performed with Δm = 4.4 t and Δt = 21 h 40 min, using an electrode with S_e = 680 mm^2.

The titanium density (γ_t) used in the calculations was 4.67-4.75 g/cm^3.

The calculated chemical composition of the consumable electrodes was identical for all melts and was as follows (wt.%): Al – 3.25; V – 9.70; Fe – 1.95; O – 0.105; C – 0.011.

The first remelt was performed in a mold with a 620 mm diameter. The first electrode was remelted at a mass melting rate of 9.90 kg/min, the second at 7.49 kg/min, and the third at 7.96 kg/min. Melting was carried out, resulting in a residual disk with a height of at least 40 mm.

Cooling after the first remelt was conducted for 10 h under residual pressure in the VAR furnace chamber (a key process parameter); cooling times for the second and third remelts were 10 h and 8 h, respectively. The average voltage during the steady-state melting stage ranged from 29.8 to 33.3 V, and the solenoid coil operated at a ±3 s periodicity.

The calculated composition of the titanium electrodes is presented in Table 6.

Table 6. Calculated charge composition of consumable titanium electrodes

Charge material	Melt 1, kg	Melt 2, kg	Melt 3, kg	Melt 4, kg
Al granules	17.1	17.1	17.1	17.1
V-Al-C master alloy	50	50	50	50
V-Al-Fe master alloy	588.3	588.3	588.3	588.3
TiO_2	8.2	8.6	8.7	8.6
Fe powder	16.4	16.5	15.7	15.4
Sponge titanium	3819.7	3819.4	3819.9	3820.3
Total	4500	4500	4500	4500

Thus, the Ti-10V-2Fe-3Al alloy was produced by triple VAR remelting. Subsequently, the alloy microstructure was investigated using scanning electron microscopy combined with energy-dispersive X-ray spectroscopy (SEM–EDS).

To study the alloy's composition and properties, four samples were taken from the electrode in the regions “top”, “middle 1”, “middle 2”, and “bottom” on the ingot's lateral surface. The results of the chemical analysis of the alloys are presented in the figure. The chemical composition of the surface samples from the four experimental Ti-10V-2Fe-3Al alloys meets the material specification. The scheme of dividing the alloys into sections is shown in Figure 2.

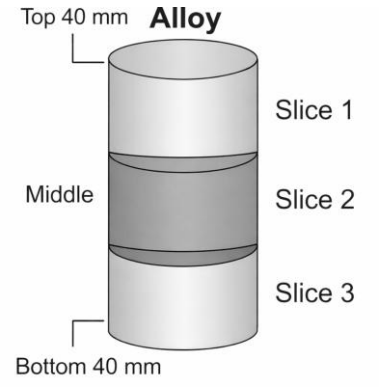

Figure 2. Scheme of alloy sectioning

Each experimental alloy was then divided into three sections, and samples were collected from the ends of each section for elemental distribution analysis across the alloy cross-section. The first cut was made 40 mm from the top of the ingot; the second, from the middle of the ingot as a representative sample of the steady-state melting regime; and the third, 40 mm from the bottom.

3.2. SEM-EDS results

To establish the relationship between the microstructure of Ti-10-2-3 titanium alloys and charge inhomogeneity, the type of alloying materials (V–Al–Fe, V–Al–C, TiO_2), the charge preparation method (briquetting, layered assembly), VAR melting regimes, and defects formed “from bottom to top” along the electrode height, SEM–EDS analysis was performed on the produced Ti-10V-2Fe-3Al alloy.

From a technological standpoint, the application of this method is also highly relevant, since industrial production may result in vertical (along the ingot height) and radial (from center to periphery) chemical gradients, non-uniform distribution of β-stabilizers (V, Fe), and variations in α/β-phase morphology during cooling. SEM–EDS analysis enables modeling of optimal technological conditions for ingot production and provides insight into the origins of these production-related issues.

The objects of investigation in the SEM–EDS analysis were four electrode zones: ingot samples taken from the “top”, “middle 1”, “middle 2”, and “bottom” regions.

The rationale for selecting these sampling locations was to investigate the following processes occurring within the ingot: the top-region sample was intended to identify potential defects associated with the final VAR pass; the middle-region samples were used to confirm steady-state crystallization; and the bottom-region sample was analyzed to reveal possible degradation of ingot structure resulting from interaction with the mold jacket or base plate.

For the SEM–EDS analysis, selected magnifications were used to characterize the structural features and phase distribution within the ingot, namely 500× for the overall micro-

structure and primary phase distribution, 1000-2000× for the α-phase plate morphology, and 5000× for local microstructural features, dispersed particles, and segregation zones.

Accordingly, the study focused on identifying vertical chemical gradients (V or Fe enrichment upward or downward), the distribution of *β*-stabilizers during remelting, the presence of oxygen or carbon segregation, an increase in oxygen content in the upper part of the ingot due to contact with residual gases during VAR, and oxygen enrichment at *α*-phase boundaries as an early stage of α_2-Ti_3Al formation.

3.2.1. Results of sample morphology analysis

As a result of studying the patterns of morphological evolution of the *α*/*β* structure, the following structural features were identified:

1). Top sample. At magnifications of ×3000-5000, thin, parallel, step-like layers, small, loose fragments, and isolated fine particles on the surface were observed. The EDS spectrum confirms the dominance of Ti (TiK*α* peak at ~4.5 keV), with pronounced peaks of V and Al and a noticeable fraction of C. The surface is relatively smooth, with isolated defects; however, the increased carbon content is attributed to the influence of the final stages of remelting, surface reactions, and/or polishing.

2). Bottom sample. At magnifications of ×3000-5000, distinct clusters of rounded and irregularly shaped particles accumulating between the "steps" of the matrix are clearly observed. By their morphology, these features resemble nonmetallic inclusions (oxides or slag fragments). Pronounced layering, significant defects, and a high number of nonmetallic inclusions were identified. This indicates that the structure formed during an unstable initial remelting stage, with possible non-uniform crystallization and local dendritic segregation, which is typical of the bottom region of an ingot. The EDS spectrum shows a Ti content of approximately 83.5-84 wt.%. The contents of V and Al are also close to nominal values, and no pronounced downward vertical segregation of *β*-stabilizers is observed. The carbon content is noticeably lower than in the top region, indirectly confirming the surface-related nature of part of the carbon enrichment in the upper section.

3). Middle 1 sample. At magnifications of ×3000-5000, individual *α*-plates appear more flattened and well-fused, and the surface is relatively smooth, without many porous particles. This region of the ingot exhibits the most uniform lamellar structure. It contains a minimal number of inclusions, indicating a steady-state VAR regime optimal for the formation of a homogeneous *α*/*β* microstructure. In this zone, the chemical composition is the most stable and closest to the calculated Ti-10V-2Fe-3Al system. The low carbon content and absence of pronounced oxygen peaks indicate a minimal presence of gas-saturated and oxide-related defects. Morphologically, this corresponds to the steady-state remelting region, where the *α*/*β* structure is uniformly formed without pronounced columnar segregation.

4). Middle 2 sample. At magnifications of ×3000-5000, this region exhibits a layered, fractured zone containing an oxide phase, with film-like or slag-related inclusions. The EDS spectrum indicates the formation of structural defects in this region.

Since the selected middle-region sample confirms a steady-state crystallization process, SEM–EDS analyses of this sample ("middle 1") are presented in Figures 3-5:

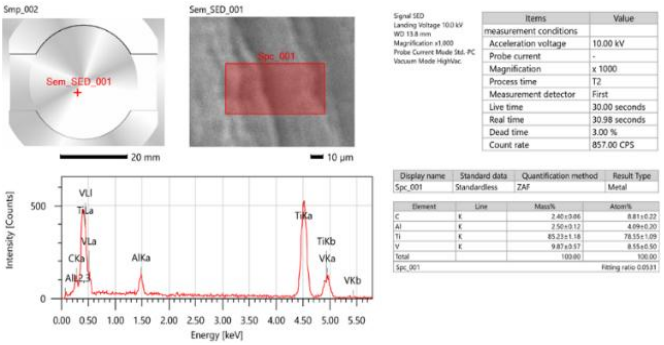

Figure 3. SEM elemental analysis results of the surface area of the "middle 1" sample

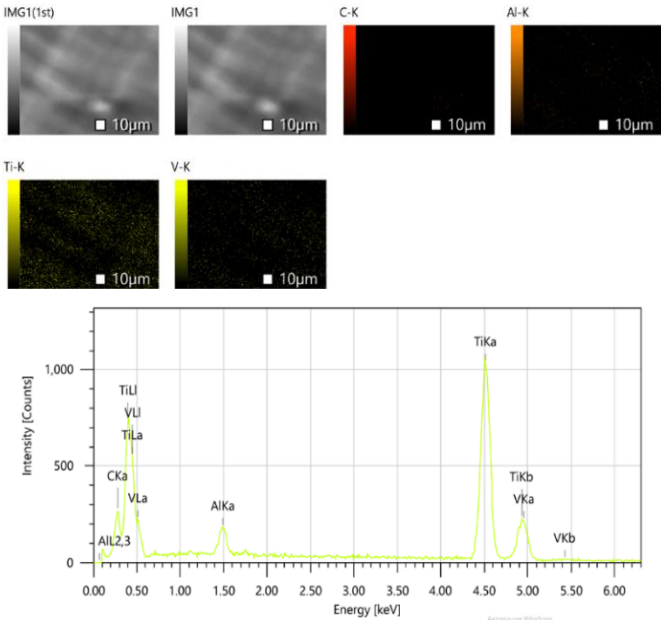

Figure 4. EDS mapping results of the "middle 1" sample

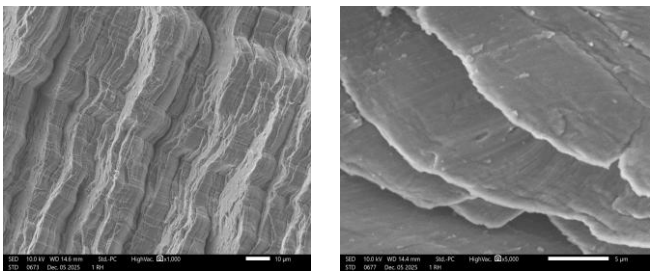

(a) (b)

Figure 5. SEM micrographs of the "middle 1" sample obtained at magnifications of: (a) – ×1000; (b) – ×5000

Based on the study of the vertical Al–V–Ti gradient along the ingot height, it was established that the absence of a pronounced vertical chemical gradient in the major alloying elements (Ti, Al, V) indicates the high efficiency of triple VAR remelting. This process ensures deep homogenization of the molten metal and effective suppression of segregation phenomena. As a result, the stability of the phase composition, the uniformity of the *α*/*β* microstructure morphology, and the predictability of mechanical properties along the ingot height are significantly improved.

Quantitative SEM–EDS data confirm the absence of a chemical gradient:

1). In all three "metallic" regions (top, bottom, and middle 1), the vanadium content lies within a narrow range of approximately 9.3-9.9 wt.%, indicating that a vertical V gradient along the ingot height is practically absent and that the β-stabilizer is distributed uniformly.

2). The aluminum content ranges from 2.5 to 3.1 wt.% across all three regions, with no significant vertical Al segregation detected.

3). A slight increase in titanium content from the top toward the middle 1 region was observed; however, this variation falls within the measurement uncertainty.

Thus, it was established that, with respect to the main alloying elements (Ti, Al, V), the ingot is chemically homogeneous along its height, and the VAR regime provides an acceptable level of macrosegregation control. The concentrations of Ti, Al, and V, the principal alloying elements in Ti-10V-2Fe-3Al, do not change significantly between samples taken from the top, middle 1, middle 2, and bottom regions of the ingot.

A compositional scatter of ≤1-1.5% is considered an excellent indicator of VAR melt quality. This level of scatter indicates minimal concentration differences: Al variations within ±0.5-1.0%, V variations within ±0.5-1.0%, and a stable Ti fraction of approximately 83-86%. For large industrial ingots with a mass of 4.5 t, such a low degree of compositional variation is regarded as a highly favorable result.

3.2.2. Results of vertical gradient analysis

An analysis of the vertical Al–V–Ti gradient along the ingot height revealed that the absence of a pronounced vertical chemical gradient in the main alloying elements (Ti, Al, V) indicates the high efficiency of triple vacuum arc remelting. This process provides deep homogenization of the molten metal and effectively suppresses macrosegregation. As a result, enhanced phase stability, uniform α/β microstructure morphology, and predictable mechanical properties along the ingot height are achieved.

The absence of a significant chemical gradient is confirmed by quantitative SEM–EDS results:

1) Vanadium (V). In all three metallic regions (top, bottom, and middle 1), the vanadium content falls within a narrow range of approximately 9.3–9.9 wt.%, indicating that a vertical V gradient is practically absent and that the β-stabilizer is distributed uniformly.

2) Aluminum (Al). The aluminum content ranges from 2.5 to 3.1 wt.% across all regions, with no evidence of significant vertical Al segregation.

3) Titanium (Ti). A slight increase in Ti content from the top toward the middle 1 region is observed; however, this variation lies within the measurement uncertainty.

Thus, the ingot is chemically homogeneous with respect to the principal alloying elements (Ti, Al, V) over its entire height, and the applied VAR regime provides acceptable macrosegregation control. The concentrations of Ti, Al, and V, the key alloying elements in Ti-10V-2Fe-3Al, do not change significantly across the top, middle 1, middle 2, and bottom regions.

A compositional scatter of 1-1.5% or less is considered an excellent indicator of VAR melting quality. This level of scatter corresponds to minimal elemental variations: Al within ±0.5-1.0%, V within ±0.5-1.0%, and a stable Ti fraction of approximately 83-86 wt.%. For large industrial ingots weighing 4.5 t, such a low degree of compositional variation represents an optimal result.

3.2.3. Development of an electrode quality control method based on SEM–EDS profiles

The obtained distribution profiles of V, Fe, Al, and O along scanning lines in the "top", "middle 1", "middle 2", and "bottom" regions make it possible to propose a quantitative electrode quality criterion based on microsegregation parameters:

– maximum deviation of β-stabilizer concentration (V, Fe) from the mean value along the line, $\Delta C_{\max}$;

– root-mean-square deviation σ_C along the line length;

– correlation length L_{corr} (the characteristic scale of chemically inhomogeneous regions);

– relative oxygen enrichment in locally enriched zones, $\Delta C_{O(local)}$.

In regions typical of the ingot middle, ΔC_{max} and σ_C remain limited, while L_{corr} is small, indicating fine-scale, well-averaged microsegregation. In the bottom part of the ingot, these parameters increase, reflecting the presence of larger-scale chemical inhomogeneities.

It is proposed to introduce an integral chemical inhomogeneity index, I_{chem}, that incorporates contributions from β-stabilizers and oxygen, and to define a limiting value, I_{chem}^{crit} (Critical Chemical Inhomogeneity Index). Exceeding this threshold indicates an unacceptable level of chemical inhomogeneity, at which the alloy or electrode should be rejected, or the triple-VAR remelting regime should be adjusted.

This approach transforms SEM–EDS analysis from a qualitative tool into a quantitative method for controlling ingot acceptance. Incorporating SEM–EDS-based homogeneity criteria into charge preparation regulations makes it possible to close the process loop "briquette → electrode → ingot" and to ensure reproducible microstructural quality under industrial production conditions.

4. Conclusions

It was established that the central regions ("middle 1") exhibit the most homogeneous distribution of V, Al, and Fe. The scatter of local β-stabilizer concentrations across the cross-section is minimal, reflecting a steady-state melting and solidification regime during triple VAR processing. The α-phase morphology in these regions is close to equilibrium: α colonies exhibit comparable thickness and length, while the β matrix forms a continuous framework without pronounced dendritic segregation.

Thus, for the first time, a comparative analysis of the α/β microstructure morphology along the height of an industrial electrode weighing 4500 kg produced by VAR at UKTMP has been performed.

It was demonstrated that no vertical chemical gradient exists along the electrode height, indicating the high quality and efficiency of the triple VAR process, as well as a uniform distribution of Al, V, and Fe governed by melting regimes and charge-mixing characteristics. The applied triple VAR technology ensures chemical homogeneity of the Ti-10V-2Fe-3Al alloy matrix along the ingot height. Local oxygen-enriched zones were identified, which may be used to predict a reduction in ductility and the potential formation of the α_2 phase.

Based on the results, a quality control methodology for electrodes was developed using SEM–EDS profiles.

Author contributions

Conceptualization: ATM, TAC; Data curation: ATM, BM; Formal analysis: ATM, TAC; Funding acquisition: ATM, TAC; Investigation: ATM, TAC; Methodology: ATM, TAC, BM; Project administration: ATM, TAC; Resources: ATM, TAC, BM; Software: ATM, TAC; Supervision: ATM, TAC, BM; Validation: ATM, TAC, BM; Visualization: ATM, TAC, BM; Writing – original draft: ATM, TAC, BM; Writing – review & editing: ATM, TAC, BM. All authors have read and agreed to the published version of the manuscript.

Funding

This research was carried out with the financial support of the agreement № 1090-TMK from 02.11.2025 / 11-168 from 19.11.2025. of Ust-Kamenogorsk Titanium and Magnesium Plant JSC.

Acknowledgements

The authors express their sincere gratitude to the editor and anonymous reviewers for their constructive comments and valuable suggestions, which have significantly improved the quality of this manuscript.

Conflicts of interest

The authors declare no conflict of interest.

Data availability statement

The original contributions presented in this study are included in the article. Further inquiries can be directed to the corresponding author.

References

[1] Banerjee, D., & Williams, J.C. (2013). Perspectives on titanium science and technology. *Acta Materialia, 61(3),* 844-879. https://doi.org/10.1016/j.actamat.2012.10.043

[2] Lutjering, G., & Williams, J.C. (2007). Titanium. *Springer.* https://doi.org/10.1007/978-3-540-73036-1

[3] Peters, M., Kumpfert, J., Ward, C.H. & Leyens, C. (2003). Titanium alloys for aerospace applications. *Advanced Engineering Materials, 5(6),* 419-427. https://doi.org/10.1002/adem.200310095

[4] Ballor, J., Li, T., Prima, F., Boehlert, C.J., & Devaraj, A. (2023). A review of the metastable omega phase in beta titanium alloys: the phase transformation mechanisms and its effect on mechanical properties. *International Materials Reviews*, *68*(1), 26-45. https://doi.org/10.1080/09506608.2022.2036401

[5] Yang, Z., Kou, H., Li, J., Hu, R., Chang, H., & Zhou, L. (2011). Macrosegregation behavior of Ti-10V-2Fe-3Al alloy during vacuum consumable arc remelting process. *Journal of Materials Engineering and Performance*, *20*(1), 65-70. https://doi.org/10.1007/s11665-010-9645-x

[6] Tahara, M., Hasunuma, K., & Hosoda, H. (2021). Microstructure of α+ β dual phase formed from isothermal α ″phase via novel decomposition pathway in metastable β-Ti alloy. *Journal of Alloys and Compounds*, *868*, 159237. https://doi.org/10.1016/j.jallcom.2021.159237

[7] Zhou, Z., Xiang, Z., Wang, B., Li, J., Chen, J., & Chen, Z. (2025). Influence of heat treatment on the mechanical properties, microstructure, and strengthening mechanisms of a novel metastable β titanium alloy. *Journal of Alloys and Compounds*, *1022*, 178726. https://doi.org/10.1016/j.jallcom.2025.178726

[8] Boyer, R.R. (1996) An Overview on the Use of Titanium in the Aerospace Industry. *Materials Science and Engineering: A*, *213,* 103-114. https://doi.org/10.1016/0921-5093(96)10233-1

[9] Taylor, C.M., Abrego Hernandez, S.G., Marshall, M. & Broderick, M. (2018). Cutting fluid application for titanium alloys Ti-6Al-4V and Ti-10V-2Fe-3Al in a finish turning process. *Procedia CIRP, 77,* 441-444. https://doi.org/10.1016/j.procir.2018.08.279

[10] Wang, X., Li, F., Xu, T., Ma, X., Hou, B., Luo, L., & Liu, B. (2021). Microstructure and microhardness evolution of Ti-10V-2Fe-3Al alloy under tensile/torsional deformation modes. *Journal of Alloys and Compounds, 881,* 160484. https://doi.org/10.1016/j.jallcom.2021.160484

[11] Ellyson, B., Saville, A., Fezzaa, K., Sun, T., Parab, N., Finfrock, C., Rietema, C. J., Smith, D., Copley, J., Johnson, C., Becker, C. G., Klemm-Toole, J., Kirk, C., Kedir, N., Gao, J., Chen, W., Clarke, K. D., & Clarke, A. J. (2023). High strain rate deformation of aged TRIP Ti-10V-2Fe-3Al (wt.%) examined by in-situ synchrotron X-ray diffraction. *Acta Materialia*, *245*, 118621. https://doi.org/10.1016/j.actamat.2022.118621

[12] Zhao, Q., Sun, Q., Xin, S., Chen, Y., Wu, C., Wang, H., Xu, J., Wan, M., Zeng, W., & Zhao, Y. (2022). High-strength titanium alloys for aerospace engineering applications: A review on melting-forging process. *Materials Science and Engineering A, 845,* 143260. https://doi.org/10.1016/j.msea.2022.143260

[13] Zhu, E., Li, F., Zhao, Q., Yuan, Z., You, J., & Hashmi, A.F. (2025). Deformation behavior of metastable Ti-10V-2Fe-3Al alloy subjected to varying pre-strain levels: Mechanism and microstructural adaptations. *Journal of Alloys and Compounds, 1029,* 180798. https://doi.org/10.1016/j.jallcom.2025.180798

[14] Qi, L., Zhang, K., Qiao, X., Huang, L., Huang, X. & Zhao, X. (2020). Microstructural evolution in the surface of Ti–10V–2Fe–3Al alloy by solution treatments. *Progress in Natural Science: Materials International, 30(1),* 106-109. https://doi.org/10.1016/j.pnsc.2020.01.011

[15] Qi, L., Qiao, X., Huang, L., Huang, X., Xiao, W. & Zhao, X. (2019). Effect of cold rolling deformation on the microstructure and properties of Ti-10V-2Fe-3Al alloy. *Materials Characterization, 155,* 109789. https://doi.org/10.1016/j.matchar.2019.109789

[16] Qi, L., Qiao, X., Huang, L., Huang, X. & Zhao, X. (2019). Effect of structural stability on the stress induced martensitic transformation in Ti-10V-2Fe-3Al alloy. *Materials Science and Engineering A, 756,* 381–388. https://doi.org/10.1016/j.msea.2019.04.058

[17] Danard, Y., Poulain, R., Garcia, M., Guillou, R., Thiaudière, D., Mantrid, S., Banerjee, R., Sun, F. & Prima, F. (2019). Microstructure design and in-situ investigation of TRIP/TWIP effects in a forged dual-phase Ti–10V–2Fe–3Al alloy. *Materialia, 8,* 100507. https://doi.org/10.1016/j.mtla.2019.100507

[18] Brozek, C., Sun, F., Vermaut, P., Millet, Y., Lenain, A., Embury, D., Jacques, P. J., & Prima, F. (2016). A β-titanium alloy with extra high strain-hardening rate: Design and mechanical properties. Scripta Materialia, 114, 60-64. https://doi.org/10.1016/j.scriptamat.2015.11.020

Ti-10V-2Fe-3Al үш мәрте қайта балқытылған қорытпаның құрылымдық және технологиялық қасиеттерін зерттеу

А.Т. Мамутова[1], Т.А. Чепуштанова[2*], Б. Мишра[3]

[1]*Өскемен титан-магний комбинаты АҚ, Өскемен, Қазақстан*
[2]*Satbayev University, Алматы, Қазақстан*
[3]*Вустер политехникалық институты, Вустер, АҚШ*

**Корреспонденция үшін автор: t.chepushtanova@satbayev.university*

Аңдатпа. Мақалада Ti-10V-2Fe-3Al құрамды үш мәрте қайта балқытылған қорытпаны алу нәтижелері келтірілген. Аталған қорытпаға жүргізілген SEM–EDS талдауының нәтижелері ұсынылып, өнеркәсіптік электродтың биіктігі бойынша Ti-10-2-3 қорытпасының құрылымы анықталған. Алғаш рет салмағы 4.5 т болатын электродтың үш сипаттамалық аймағында – «жоғарғы», «орта 1», «орта 2», «төменгі» – *α*/*β*-фазалардың морфологиясы мен жергілікті химиялық құрамын тікелей салыстыру нәтижелері кешенді SEM–EDS талдауы негізінде алынды. Негізгі легирлеуші элементтер (Ti, Al, V) бойынша құйма биіктігі бойымен толық химиялық теңестірілгені және ВДП (вакуумды доғалық қайта балқыту) режимі макросегрегацияның қолайлы деңгейін қамтамасыз ететіні анықталды. Ti-10V-2Fe-3Al қорытпасындағы басты легирлеуші элементтер – Ti, Al және V концентрацияларының сынамалар арасында айтарлықтай өзгермейтіні көрсетілді. SEM–EDS талдауы нәтижелері элементтер концентрациясының шашырауы ≤1–1.5% шегінде екенін көрсетті, бұл ВДП балқытудың сапалы жүргізілгенінің көрсеткіші болып табылады; яғни элементтер концентрацияларындағы айырмашылықтар минималды: Al өзгерістері ±0.5–1.0%, V өзгерістері ±0.5-1.0%, ал Ti тұрақты түрде шамамен ~83-86% үлесті құрайды. Морфологиялық зерттеулер нәтижесінде *α*/*β*-құрылымның біркелкі қалыптасқаны, айқын бағаналы сегрегацияның жоқ екені анықталды. *α*/*β*-фазалар морфологиясын тікелей салыстыру нәтижелері SEM–EDS профильдері бойынша электродтардың сапасын бақылау әдістемесін әзірлеуге мүмкіндік берді.

Негізгі сөздер: *титан қорытпасы; вакуумды доғалық қайта балқыту; SEM–EDS талдауы; үш мәрте қайта балқыту; α/β-микроқұрылым; морфология.*

Исследование структурных и технологических свойств сплава тройного переплава Ti-10V-2Fe-3Al

А.Т. Мамутова[1], Т.А. Чепуштанова[2*], Б. Мишра[3]

[1]*АО Усть-Каменогорский титаномагниевый комбинат, Усть-Каменогорск, Казахстан*
[2]*Satbayev University, Алматы, Казахстан*
[3]*Вустерский политехнический институт, Вустер, США*

**Автор для корреспонденции: t.chepushtanova@satbayev.university*

Аннотация. В статье представлены результаты получения сплава тройного переплава состава Ti-10V-2Fe-3Al, представлены результаты SEM–EDS анализа данного сплава, определена структура сплава Ti-10-2-3 по высоте промышленного электрода. Впервые получены результаты прямого сопоставления морфологии *α*/*β*-фаз и локального химического состава в трёх характерных зонах электрода весом 4.5 т – «верх», «середина 1», «середина 2», «низ» на основе комплексного анализа SEM–EDS. Установлено, что по основным легирующим элементам (Ti, Al, V) слиток полностью химически выровнен по высоте, и ВДП-режим обеспечивает приемлемый уровень макросегрегации. Установлено, что концентрации Ti, Al, V (главные легирующие элементы в Ti-10V-2Fe-3Al) не меняются существенно между пробами. Определено, что SEM–EDS результаты проб показывают на разброс концентраций элементов ≤1–1.5%, что считается показателем качества проведенной ВДП плавки, процент разброса означает, что различия концентраций элементов минимальны: изменения Al – в пределах ±0.5-1.0%, изменения V – в пределах ±0.5-1.0%, Ti занимает стабильную долю ~83–86%. Результатами морфологических исследований установлено, что структура *α*/*β* сформирована равномерно, без выраженной колонной сегрегации. Результаты прямого сопоставления морфологии *α*/*β*-фаз позволили разработать методику контроля качества электродов по SEM–EDS-профилям.

Ключевые слова: *титановый сплав; вакуумно-дуговой переплав; SEM–EDS анализ; тройной переплав; α/β-микроструктура, морфология.*

Publisher's note

All claims expressed in this manuscript are solely those of the authors and do not necessarily represent those of their affiliated organizations, or those of the publisher, the editors and the reviewers.

SATBAYEV UNIVERSITY

Engineering Journal of Satbayev University

Volume 148 (2026), Issue 1, 16-28

https://doi.org/10.51301/ejsu.2026.i1.03

Dynamics of temperature-strength changes in the immediate roof and formation of the gasified cavity of an underground gasifier

P. Saik[1,2], V. Lozynskyi[1,2*], M. Berdnyk[1], D. Klimov[1]

[1]*Belt and Road Initiative Center for Chinese-European Studies (BRICCES), Guangdong University of Petrochemical Technology, Maoming, China*

[2]*Dnipro University of Technology, Dnipro, Ukraine*

**Corresponding author: lozynskyi.v.h@nmu.one*

Abstract. This study aims to identify regularities in the evolution of the temperature field and the uniaxial compressive strength (UCS) of immediate roof rocks under the influence of chemical reaction zones along the combustion face. It also aims to determine how the goaf area forms and changes over time as a function of gasification duration, injection pressure of the blowing mixture, and coal seam thickness. The study was carried out using a laboratory UCG setup that reproduces combustion face advance and roof deformation. The temperature in the modelled immediate roof was recorded by sensors installed along the reaction channel. Siltstone samples taken from the immediate roof of seam n_7^n at the Mezhyrichanska mine (SE "Lvivvuhillia", Ukraine) were thermally treated and tested in uniaxial compression using a KL 200/CE-Tecnotest press. The goaf geometry was determined from roof-subsidence reference sensors, graphical reconstruction of contours at different time instants, and area calculation by the trapezoidal rule with consideration of producer-gas composition and concentration. At 0.55 m above the seam, temperature in the oxidizing zone (0-9 m) increased from approximately 323 to 550°C, reached about 573°C in the transition zone (9-11 m), and decreased to ~200°C in the reducing zone (11-30 m). UCS varied along the combustion face with a maximum near the transition zone and a subsequent decrease in the reducing zone. An exponential relationship was observed in the oxidizing zone, whereas a logarithmic relationship was observed in the reducing zone. The goaf area changed nonlinearly, predominantly exponentially, with gasification duration and seam thickness. It was also associated with the injection-pressure regime of the blowing mixture and roof-caving manifestations. The identified relationships can be used to predict goaf parameters and to assess roof stability when substantiating controlled UCG operating regimes.

Keywords: *underground coal gasification; goaf; temperature field; rocks; uniaxial compressive strength; combustion face.*

Received: 14 August 2025
Accepted: 2 February 2026
Available online: 28 February 2026

1. Introduction

Today, underground coal gasification is regarded as one of the promising technologies that enables the rational use of a substantial part of the resource base that was previously considered economically impractical or technically unsafe for conventional mining [1, 2]. One of the key advantages of underground coal gasification is a significant reduction in anthropogenic pressure on mining regions [3, 4]. Unlike conventional mining, underground gasification does not require the development of underground workings, hoisting of rock mass to the surface, or the creation of waste rock dumps, sludge ponds, or tailings storage facilities. As a result, the area of technogenically disturbed land is substantially reduced, the scale of potentially hazardous geoenvironmental objects is limited, and the risk of adverse environmental impacts is reduced [5-9]. Another essential advantage is improved industrial safety. Since the main processes occur without personnel in underground space, the primary hazards typical of conventional underground coal mining are eliminated, including gas-dynamic events, roof falls, sudden outbursts, and methane or coal-dust explosions [10-12].

The implementation of underground coal gasification is particularly relevant for the coal-mining regions of Ukraine, where a considerable share of reserves occurs under challenging mining and geological conditions, including thin seams, significant depths, and previously mined or otherwise hazardous zones [13-15]. Under such conditions, underground gasification may become one of the key directions for transforming the coal sector by combining energy efficiency with environmental and technical safety.

The efficiency, stability, and safety of this process are determined mainly by the parameters of the underground gasifier, where complex coupled thermal, physico-chemical, and gas-dynamic processes develop within the rock mass [16-18]. In this context, studying the geomechanical stability of the rock mass under the action of thermal and chemical processes accompanying gasification becomes especially important. Because the behaviour of the immediate roof rocks governs the stability of the reaction cavity, the safe operation of the gasifier, and the overall process performance, their condition requires comprehensive and rigorous integrated investigations.

saik.p.b@nmu.one; lozynskyi.v.h@nmu.one; berdnyk.m.g@nmu.one; klimov.d.h@nmu.one
Engineering Journal of Satbayev University. eISSN 2959-2348. Published by Satbayev University

In addition to purely technological factors, the relevance of underground coal gasification is strengthened by the need to ensure energy resilience and flexibility of energy supply systems under instability, where the role of decentralised approaches and optimisation of power generation control is increasing [19]. At the same time, the efficiency and controllability of the UCG process depend on the correct consideration of mass and heat balances in the reaction channel. This is particularly important under complicated geological conditions, including discontinuities and faults, which directly affect the formation of temperature fields and the energy performance of gasification [20, 21].

One of the key characteristics of underground gasifier operation is the formation of the gasification goaf, which directly influences the intensity of gasification reactions, the conditions of heat and mass transfer, and the filtration properties of the rock mass [22, 23]. The evolution of the gasification goaf is nonlinear. It is governed by the combined effects of mining and geological conditions, the physicochemical properties of coal, the composition of blowing mixtures, reactant injection regimes, and the thermodynamic parameters of the process [24].

2. Literature review

The influence of high temperatures on the physicomechanical properties of rocks is intensively studied in contemporary scientific literature. This interest is driven by the development of high-temperature mining technologies, in particular underground coal gasification and in situ coal combustion [22-24]. The implementation of these technologies is accompanied by substantial thermal, gas-dynamic, and chemical impacts on the coal seam and surrounding rocks. As a result, the stress-strain state changes, and strength parameters within the rock mass are redistributed [25-28]. The relevance of investigating rock-mass strength dynamics stems from the fact that roof and surrounding-rock stability within the thermally affected zone is a critical factor for predicting potential deformations, preventing uncontrolled caving, defining the boundaries of the reaction cavity, and assessing process safety. Under the combined action of high temperatures, thermochemical decomposition, and the formation of secondary porosity, the mechanical properties of rocks may vary over a wide range. This requires a comprehensive analysis that accounts for the rock mass's temporal and spatial heterogeneity. Therefore, given the growing interest in coal thermochemical conversion technologies in Ukraine and worldwide, assessing rock strength characteristics is particularly important.

Understanding the regularities of strength degradation in the rock mass and the formation of weakened zones is essential for developing reliable geomechanical models, optimising gasification operating regimes, and preparing recommendations for industrial implementation [29]. Studying the dynamics of rock-mass strength during underground coal gasification is an important scientific and applied task that provides a basis for improving the safety, efficiency, and controllability of these geotechnologies.

In contrast to combustion, underground gasification enables a controlled thermal regime and a more uniform distribution of chemical reaction zones along the reaction channel [30-32]. This can substantially reduce the thermal load on the rock mass and ensure a more stable development process, thereby improving overall safety. Underground coal gasification is characterised by continuous formation and migration of active zones within the reaction channel. Their dynamics are governed primarily by the temperature field in the underground gasifier. Experimental and laboratory studies [33, 34] describe the spatiotemporal temperature distribution around the gasifier in detail and demonstrate a consistent pattern of evolution that corresponds to the progression of chemical reactions across different sections of the reaction channel. Temperature variations determine the character, intensity, and position of the oxidizing and reducing zones, which, in turn, control thermochemical transformations and the geomechanical state of the surrounding rocks [35].

Laboratory and analytical studies have shown that the temperature gradient along the reaction channel varies widely depending on reaction activity [36-38]. In the oxidizing zone, the temperature ranges from 600 to 1050 °C. This zone is characterised by intensive exothermic oxidation of carbon ($C + O_2 \rightarrow CO_2 + q$, where $q \approx 394$ kJ/mol), which provides the primary input of thermal energy to the system. The temperature gradient within this section is 25-50°C/m, which is explained by the high rate of heat release concentrated in a limited volume.

Endothermic reactions, in particular, characterise the reducing zone:

$$C + H_2O \rightarrow CO + H_2 - q \ (\approx 131 \text{ kJ/mol}), \quad (1)$$

$$C + CO_2 \rightarrow 2CO - q \ (\approx 172 \text{ kJ/mol}). \quad (2)$$

In this part of the channel, the temperature gradually decreases to 412°C, and the gradient is 15-20°C/m. The lower rate of change is due to reactions consuming heat and to the limited availability of reagents from the blowing mixture. The transition zone between the exothermic and endothermic intervals is significant because it produces the most tremendous thermal impact on the rock mass. This zone is associated with peak thermal loading, resulting in the most intense changes in rock geomechanical properties.

Today, despite a substantial body of research on underground coal gasification, systematic investigation of the gasification goaf dynamics remains underdeveloped. Most existing approaches focus on individual aspects of the process, in particular on generalised characteristics of goaf growth [39]. They do not provide a unified methodological basis for analysing its temporal evolution and its expansion relative to the chemical reaction zones within an underground gasifier [40]. For example, study [41] substantiated the parameters governing the formation of bedding-separation cavities in roof rocks during underground coal gasification and established their dependence on reaction channel length. However, that approach did not account for the spatial arrangement of chemical reaction zones along the reaction channel, thereby limiting the scope for a comprehensive analysis of gasification goaf dynamics. Study [42] identified regularities in the formation of the gasification goaf during coal gasification through vertical wells. At the same time, the reported goaf parameters mainly describe the final stage of the process, namely the attenuation of gasification operations, which restricts analysis of the active stage. The authors of [43] demonstrated that the parameters of the gasification goaf, including its shape, dimensions, and the spatial position of active zones, are closely related to gasification process control regimes. This supports the need to predict gasification goaf geometry based on thermal and technological parameters as a prerequisite for improving controllability UCG.

Most studies on the effect of temperature on the physico-mechanical properties of rocks have been conducted under laboratory conditions [44, 45]. They typically do not account for the spatial variation of the temperature field along the combustion face of an underground gasifier. In many cases, the results of such experiments have been considered separately from the actual conditions that govern the formation of chemical reaction zones. This complicates direct transfer of the obtained data to field-scale objects [46-48]. At the same time, research on the effects of temperature on rock properties shows both common trends and pronounced differences. This allows the identification of regularities in the evolution of strength as a function of rock type, mineralogical composition, and structural features. In particular, most sedimentary rocks exhibit an initial increase in strength due to dehydration and changes in intercrystalline contacts. At higher temperatures, however, structural rearrangement, mineral decomposition, and crack formation are observed [49-52].

Study [53] established a clear relationship between temperature and sandstone strength. As the temperature increased from 25 to 800°C, the uniaxial compressive strength decreased from 95.6 to 49.5 MPa. A similar trend was reported for the elastic modulus, which decreased after 200°C and 400°C. The authors attributed these changes to rock dehydration, microcrack development, and the subsequent thermal decomposition of quartz and feldspar. Research [54] confirmed a reduction in sandstone tensile strength during heating. Up to 500°C, the changes remained relatively stable, whereas at 600°C, a sharp drop in strength of 22-23% was observed. Study [55] examined the behaviour of marble, limestone, and sandstone. The authors noted that the peak strength and elastic modulus of carbonate rocks decrease after 200-400°C, and that a sharp deterioration in mechanical properties occurs after 600°C. It was also emphasised that peak strain increases markedly when rocks are heated above 600°C. In [56] and [57], it was reported that the strength evolution depends strongly on rock mineralogy. Carbonate rocks may temporarily strengthen when heated to 150°C. With further temperature increases, dehydration begins, and intensive microcracking develops. Study [58] found that granite strength decreases by 80% when heated to 1000°C. The most pronounced change occurs in the 400-600°C range, which the authors associated with the quartz phase transition at 573°C.

Results for sandstone heated to 1100°C [59] indicate a more complex response. Strength increases up to 400°C by nearly a factor of two, but then drops sharply to 26 MPa. Claystone specimens show a different pattern. When heated to 400°C, strength increases due to water evaporation and rock densification, but above 400°C, it rapidly decreases, reaching 70 MPa [60]. Study [61] reported data on clay- and sandy-shale samples heated to 1000°C, where strength increased, attributed to dehydration and decarboxylation reactions. Studies on limestone properties [62] indicate that significant strength loss occurs already at 100°C, while further heating to 700-800°C produces little additional change in load-bearing capacity. Study [63] analysed changes in sandstone strength and permeability. Both were reported to increase up to 200°C, after which mechanical properties deteriorated due to microcrack development. Investigations of residual strains in sandstone at 700-1200°C [64] showed a sharp increase caused by profound changes in rock structure.

A synthesis of the above studies indicates that the effect of temperature on rock mechanical properties is complex and nonlinear. It depends strongly on mineralogical composition, texture, porosity, and the specific mechanisms of thermally induced reactions. Temperature-driven changes may manifest as temporary strengthening, especially in water-bearing rocks, or as abrupt structural weakening once critical temperature thresholds are reached. These thresholds are commonly associated with phase transformations and thermal decomposition of minerals [65]. Therefore, specialised experimental investigations are required for each specific mining and geological setting to account for rock-specific behaviour.

At the same time, without linking laboratory-derived regularities to the actual temperature distribution along the reaction channel of an underground gasifier, it is not possible to adequately reproduce the rock mass's mechanical response under UCG conditions. This emphasises the need for integrated studies that consider the spatial arrangement of chemical reaction zones, the nature of temperature gradients, and their influence on roof conditions. Such studies should also address the associated parameters governing gasification goaf formation in underground gasifiers. Because goaf geometry evolves in space and time and results from coupled thermal and geomechanical processes, its dynamics should be treated as an integral component when assessing reaction-cavity stability and gasification controllability. In this regard, an important scientific and practical task is to investigate the dynamics of the gasification goaf in an underground gasifier. Such investigations provide an integrated framework for analysing the temporal evolution of its parameters and lay the groundwork for improving the controllability and predictability of the underground gasification process.

In view of the above, this article aims to investigate changes in the strength characteristics of the immediate roof rocks of an underground gasifier due to high-temperature chemical reaction zones along the combustion face. It also aims to establish regularities in the formation and evolution of the gasification goaf area in space and time as a function of gasification duration and coal seam thickness.

Achieving this aim requires solving the following interrelated tasks:

– to determine the temperature dependence in the immediate roof rocks of the underground gasifier;

– to examine changes in the strength characteristics of the immediate roof of the underground gasifier along the combustion face length, where the roof is represented by siltstone;

– to propose a method for calculating the gasification goaf area of the underground gasifier;

– to establish relationships describing the formation and evolution of the gasification goaf area as a function of gasification duration and coal seam thickness.

3. Materials and methods

3.1. Temperature field and strength testing of the immediate roof rocks

The temperature-field distribution was investigated using a dedicated bench-scale test rig designed to reproduce conditions close to those of underground coal gasification [66]. Temperature was recorded by thermocouples embedded in the modelled immediate roof of the laboratory gasifier, which provided reliable data on the thermal regime along the reaction channel.

Changes in the physico-mechanical properties of the rock mass were evaluated through laboratory testing of rock samples collected from the immediate roof of seam n_7^n at the Mezhyrichanska mine of SE "Lvivvuhillia" (Ukraine). The immediate roof is represented by siltstone. This choice was motivated by the fact that, in most mines in the region, the immediate roof rock consists of approximately 80% siltstone, with claystone and sandstone each accounting for about 10%. The collected rock fragments were pre-processed using a TCM350 stone-cutting machine to prepare samples with the required geometry for further testing.

Heating prepared samples batches simulated thermal impact in an electric muffle furnace to preset temperatures characteristic of different chemical reaction zones along the combustion face of the underground gasifier. The investigated temperature range covered values typical of the chemical reaction zones in the underground gasifier. These values were defined at a distance of 0.55 m above the seam, which corresponds to half the thickness of the siltstone layer in the immediate roof.

This approach enabled reproducing the thermal impact on the rock under conditions as close as possible to natural ones. It enabled an objective assessment of how increased temperature affects the physico-mechanical properties of the rock mass within the underground gasifier's influence zone. The general view of the selected rock samples and their condition during laboratory testing is shown in Figure 1.

(a) (b)

Figure 1. General view of the selected rock samples (a) and the strength testing procedure (b)

Uniaxial compressive strength was determined using a KL 200/CE-Tecnotest testing press, which provides high-precision load control and enables reliable evaluation of rock mechanical behaviour before and after thermal treatment.

3.2. Determination of gasified space parameters during laboratory UCG modeling

The advance rate of the combustion face governs the dimensions of the gasification goaf in an underground gasifier. This rate is a variable parameter and depends on the location and activity of the chemical reaction zones. During the investigation of underground coal gasification, the following were determined. These included combustion face displacement parameters as a function of gasification duration, roof subsidence parameters in the underground gasifier, and the concentrations of combustible gases (CO, H_2, CH_4) in the producer gas.

Roof subsidence parameters were established from displacement measurements of reference sensors installed in the modelled immediate roof of the underground gasifier under laboratory conditions. The use of these sensors enabled accurate tracking of rock deformation and real-time analysis of accumulated laboratory data. Based on the maximum roof subsidence data over a given time interval, a detailed graphical reconstruction of the gasification goaf was performed. This reconstruction reflected the dynamics of combustion face advance. It enabled the identification of potential roof-caving zones and supported real-time assessment of structural changes in the underground gasifier's roof. Figure 2 presents an example schematic illustrating combustion face advance and the formation of the gasification goaf.

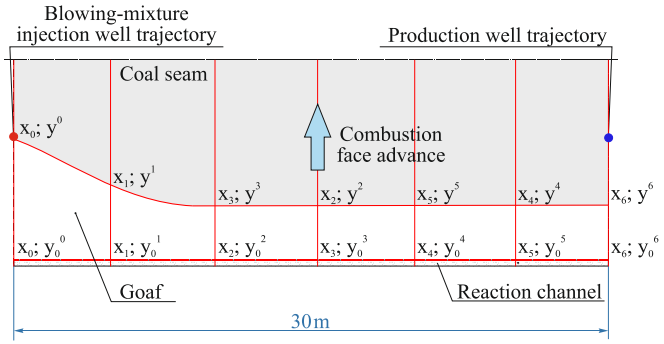

Figure 2. Schematic of combustion face advance and gasification goaf formation

Based on the obtained data (Figure 2) on the combustion face position (x_0, y^0;… x_6, y^6) and the reaction channel position (x_0, y_0^0;….; x_6, y_0^6), the area of the gasification goaf of the underground gasifier and the area of collapsed rocks are determined. During underground coal gasification, it is reasonable to distinguish three main zones within the gasification goaf. Each zone exhibits both standard and distinct features that govern the process behaviour.

The first zone is the combustion face zone, which is characterised by the combustion face area S_f. It forms adjacent to the combustion face and extends into the gasification goaf. The zone depends on the combustion face advance rate and the roof-caving step. It is the most active zone and the most critical for process control because the main chemical reactions converting coal into producer gas occur there.

The second zone is the caving zone, which is characterised by the caving area S_c. It covers regions where roof rocks lose stability and may collapse, potentially altering the geometry of the underground gasifier.

The third zone is the total gasification goaf area, ΣS, which encompasses the entire region where underground coal gasification occurs.

For optimising the blowing-mixture injection parameters, the S_f value is important. It is determined using the following equation:

$$S_f = \sum S - S_c \text{ , m}^2. \quad (3)$$

The boundaries of variation of ΣS are defined by the combustion face position, its length, and the reaction channel position. When these parameters are considered in a coordinate system, x represents the locations of the reference sensors along the combustion face length (30 m with a 5 m spacing). The coordinate y represents the combustion face position within the gasification panel. It changes over time and depends on the chemical reaction zone along the combustion face. The coordinate y_0 denotes the reaction channel position. Based on these coordinates, the gasification goaf area can be determined using the trapezoidal rule. As an example, the procedure for calculating the area of the ΣS zone is given below.

Area between the coordinates (x_0, y^0) and (x_1, y^1):

$$S_{x_0-x_1} = \frac{\left(y^0 + y^1\right)\left(x_1 - x_0\right)}{2}, \text{ m}^2; \quad (4)$$

Area between the coordinates (x_1, y^1) and (x_2, y^2):

$$S_{x_1-x_2} = \frac{\left(y^1 + y^2\right)\left(x_2 - x_1\right)}{2}, \text{ m}^2; \quad (5)$$

Area between the coordinates (x_5, y^5) and (x_6, y^6):

$$S_{x_5-x_6} = \frac{\left(y^5 + y^6\right)\left(x_6 - x_5\right)}{2}, \text{ m}^2; \quad (5)$$

$$\sum S = S_{x_0-x_1} + S_{x_1-x_2} + \ldots + S_{x_5-x_6}, \text{ m}^2; \quad (6)$$

The parameters of the S_c zone are determined using the same calculation scheme.

The calculated areas ΣS, S_f, and S_c characterise both the development of the gasified space and the onset of caving within the modelled roof. This enables the process to be interpreted in terms of controllability, because changes in S_f reflect the active reaction region that responds to the blowing-mixture regime. The following section presents the results and discusses the relationships among the gasified space evolution, the thermal field, and the roof-rock behaviour.

4. Results and discussion

4.1. Temperature field and strength variation of the immediate roof rocks

As a result of the conducted studies, data were obtained on the variation in the temperature field in the immediate roof rocks along the combustion face, at a distance of 0.55 m above the coal seam (Figure 3).

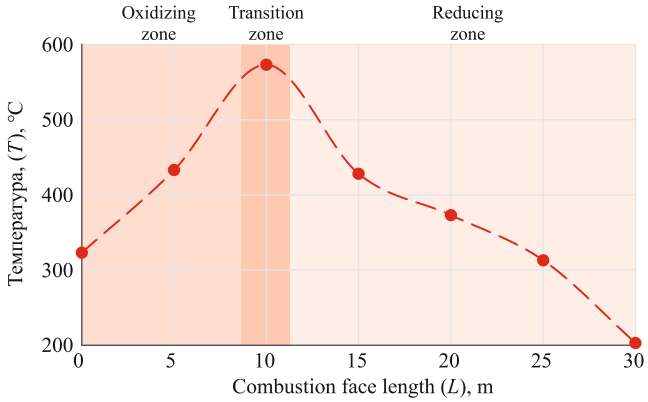

Figure 3. Dynamics of temperature variation in the immediate roof rocks

According to the analysis of the data shown in Figure 3, within the oxidizing zone (0-9 m), the temperature increases from approximately 320 to 550°C. This corresponds to the intensive development of exothermic carbon-oxidation reactions, which release substantial heat. At a distance of 9-11 m, the maximum temperature gradient is recorded. This interval corresponds to the transition zone, where the temperature reaches 575°C. In the reducing zone (1130 m), the temperature gradually decreases to 200°C. This decline results from endothermic reduction reactions, during which heat is actively absorbed.

The obtained results are consistent with previous studies reporting an asymmetric temperature-field distribution in the rock mass surrounding an underground gasifier. This asymmetry is caused by changes in the type and intensity of chemical reactions along the combustion face, which produces a complex spatial pattern of thermal impact on the roof rocks.

Further analysis that accounted for the spatial temperature distribution enabled the identification of regularities in the variation of rock strength characteristics along the combustion face length. This approach reproduced the actual pattern of thermal impact on the rock mass and enabled evaluation of the degree of weakening in the corresponding chemical reaction zones. This is critical for predicting rock-mass stability during underground gasifier operation. The dependence of the uniaxial compressive strength of rock specimens from the Mezhyrichanska mine of SE "Lvivvuhillia" on temperature, which corresponds to different chemical reaction zones of underground coal gasification, is shown in Figure 4.

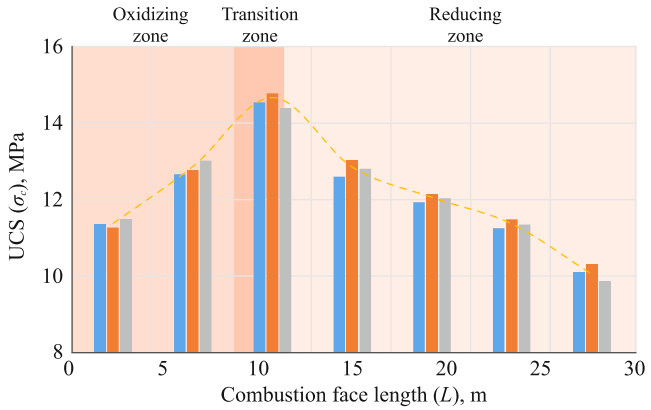

Figure 4. Data on the variation in rock uniaxial compressive strength across the chemical-reaction zones of underground coal gasification: 1-3 – rock samples; 4 – averaged value

Analysis of the data in Figure 4 shows a clear relationship between rock strength variation and temperature along the combustion face. In the oxidizing zone (0-9 m), strength increases. At 0 m, which corresponds to the location of the injection well, the average values are 11.3-11.5 MPa. At 5 m, strength increases to 12.7-13.1 MPa. At 10 m, corresponding to the maximum thermal impact within the transition zone, a strength peak of 14.50-14.89 MPa is observed, with an average strength of 14.8 MPa. In the reducing zone (11-30 m), strength decreases gradually from 12.9 to 10.1 MPa. The minimum values of 9.9-10.4 MPa correspond to the location of the production well of the underground gasifier. Therefore, along the combustion face length, the uniaxial compressive strength varies according to a polynomial relationship as follows:

$$UCS_c = 11.8 + 0.28L - 0.01L^2, \text{ MPa}, \quad (7)$$

where L is the combustion face length, m.

Along the combustion face of the underground gasifier, rock strength varies widely due to differences in the physicochemical processes in the corresponding reaction zones. Therefore, it is more appropriate to evaluate strength parameters separately for each interval rather than generalise them using a single polynomial relationship. With these considerations, separate relationships were obtained for the strength variation of the immediate roof rocks of the underground

gasifier for different chemical reaction zones. This enabled a more accurate description of rock mechanical behaviour under the temperature conditions characteristic of the oxidizing, transition, and reducing sections of the reaction channel.

Two characteristic temperature ranges were identified. The first range corresponds to the oxidizing zone and is characterized by a gradual increase in rock strength due to dehydration, partial densification, and strengthening of intercrystalline contacts. The second range corresponds to the reducing zone, where the temperature variation along the combustion face length results in only a minor increase in rock strength. Such a separation of temperature intervals enabled the correct interpretation of the results and the development of relationships that reflect the actual strength changes in the immediate roof rocks during underground coal gasification. The obtained results are shown in Figure 5.

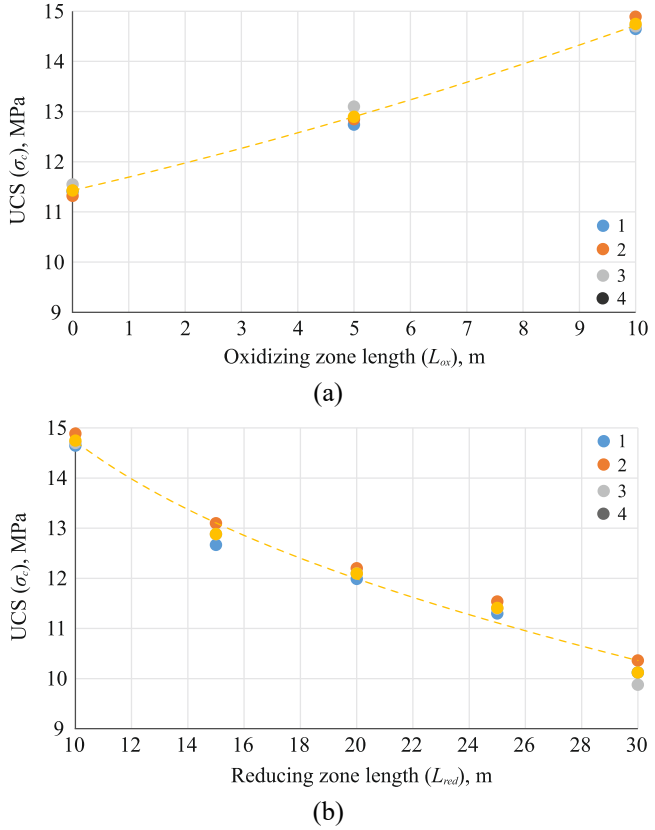

Figure 5. Variation in the uniaxial compressive strength of rocks along the length of the combustion face as a function of the temperatures in the chemical-reaction zones: (a) – oxidizing zone; (b) – reducing zone: 1-3 – rock samples; 4 – averaged value

Analysis of the data in Figure 5 shows that an exponential relationship of the form describes the strength variation in the oxidizing zone (a):

$$UCS_c^{ox} = 11.4\exp(0.023L^{ox}), \text{ MPa}, \quad (7)$$

where L_{ox} is the length of the oxidizing zone of the combustion face, m.

This curve shape reflects an intensive increase in strength under temperatures typical of this section of the reaction channel, where dehydration processes and changes in intercrystalline bonds dominate. In contrast, the strength variation of the immediate roof rocks in the reducing zone is described by a logarithmic relationship of the form:

$$UCS_c^{red} == 23.8 - 3.9\ln(L^{red}), \text{ MPa}, \quad (8)$$

where L_{red} is the length of the reducing zone of the combustion face, m.

Within the oxidizing zone up to the transition zone, the temperature rise leads to a 22-38% increase in rock strength compared with the initial mean value of 9.1 MPa. The maximum strength is reached in the transition zone of the underground gasifier. After that, towards the production well, the values begin to decrease. In the plane of the production well, the average rock strength increased by 10% (1.0 MPa). In general, an increase in the strength of the immediate roof rocks directly improves the overall stability of the rock mass. Stronger rocks can more effectively carry and redistribute stresses that arise during the formation of the reaction cavity in the underground gasifier. As a result, the probability of deformations, subsidence, and local caving is reduced, providing more stable operating conditions for the underground gasifier and improving operational safety.

4.2. Dynamics of gasified space formation and its relation to process control

Based on the obtained data, each experimental series included not only a graphical reconstruction of combustion face advance but also a detailed analysis of the formation of the gasified space over time. This covered the dynamics of temperature, pressure, and gas concentrations at different stages of gasification. In total, 216 graphical representations of process dynamics were developed. They enable determining the gasified area as a function of time, including the stage associated with roof caving, using the trapezoidal rule. Sectional profiles of the gasified space were also analysed, which enabled the accurate determination of its geometric parameters.

The data in Figure 6a indicate that after 6 h of gasification, the gasified space area is 12.6 m^2. When the reaction channel area is included, the total area equals 18.6 m^2. The combustion face advance rate is 0.07 m/h. The combustion face is linear, and the oxidizing-zone length is L_{ox} = 9.0 m. The blowing-mixture injection pressure is 0.4 MPa. The concentration of combustible gases is 37.9%.

During further gasification of the coal seam, an acceleration of combustion face advance in the oxidizing zone is observed (Figure 6b). At 10.5 h of gasification, a decrease in the concentration of combustible gases to 37.2% was recorded. For this reason, a decision was made to increase the blowing-mixture injection pressure. At an average pressure of 0.45 MPa, the concentration of combustible gases increased to 38.5% at 12.0 h of gasification. This indicates active interaction between the blowing-mixture components and the coal seam surface. An increase in pressure intensifies interphase contact, thereby promoting thermochemical gasification reactions.

Under these conditions, the gasified space area is 32.5 m^2. For a coal seam thickness of 1.0 m, the pressure increase of the blowing mixture started at 9.0 h of the process. For seam thicknesses of 0.8 m and 0.6 m, it started at 6.8 h and 5.8 h, respectively. The corresponding gasified space areas were 31.2 m^2, 32.1 m^2, and 34.2 m^2.

It should be noted that throughout the gasification process, which lasted 16.4 h (Fig. 6c), the gasified area increased, resulting in a total increase of 7.5 m^2.

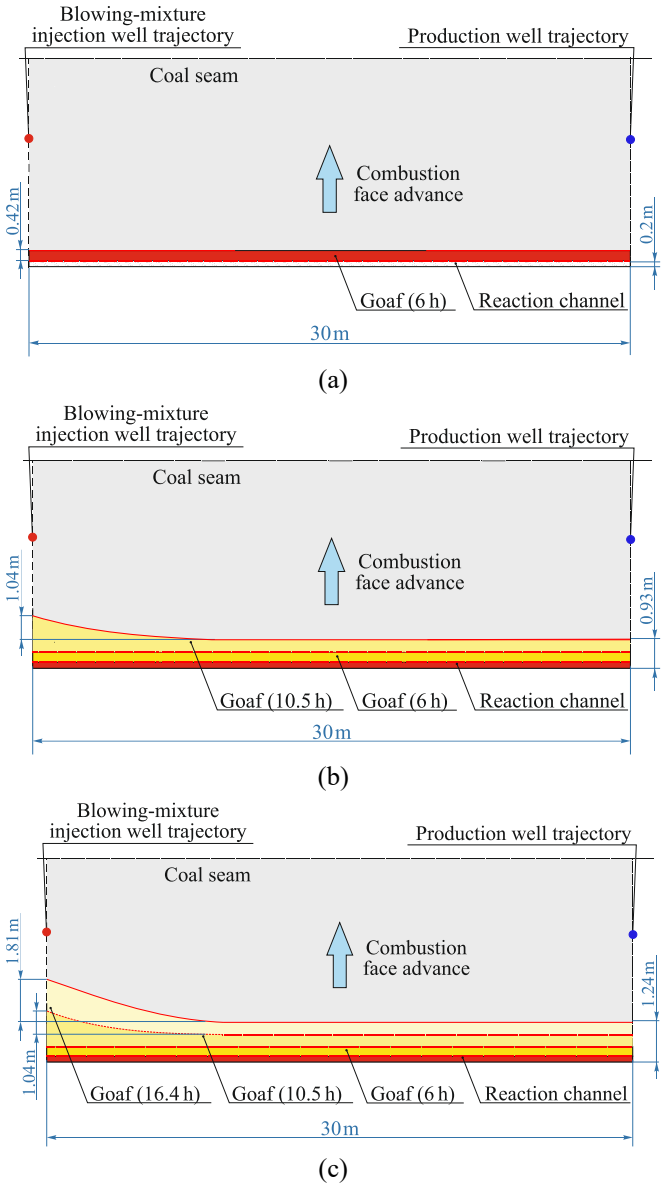

Figure 6. Schematic of combustion face advance at coal seam thickness m = 1.2 m, and blowing-mixture injection pressure P = 0.45 MPa for different gasification durations (a) – 6.0 h; (b) – 10.5 h; (c) – 16.4 h

This increase occurred while the blowing-mixture injection pressure remained stable at 0.45 MPa, which indicates high gasification efficiency under the given conditions. At 19.8 h of gasification, the concentration of combustible gases began to decrease, reaching 37.5%. Therefore, the blowing-mixture injection pressure was increased to 0.57 MPa. The gasified space area reached 53.0 m^2. For a seam thickness of 1.0 m, the pressure increase started at 16.9 h. For seam thicknesses of 0.8 m and 0.6 m, it started at 14.2 h and 11.2 h, respectively. The corresponding gasified space areas were 52.5 m^2, 53.4 m^2, and 51.5 m^2. The average blowing-mixture injection pressure was 0.57 MPa.

With further growth of the gasified space to 60.4 m^2 at 23.7 h (Figure 7), the blowing-mixture injection pressure reached 0.67 MPa. At the same time, roof subsidence was recorded on the injection-well side. A pressure of 0.67 MPa was applied for 5.5 h. The average combustible gas concentration was 39%. Measurements of the combustion product composition showed that CO_2 is a significant component of the producer gas.

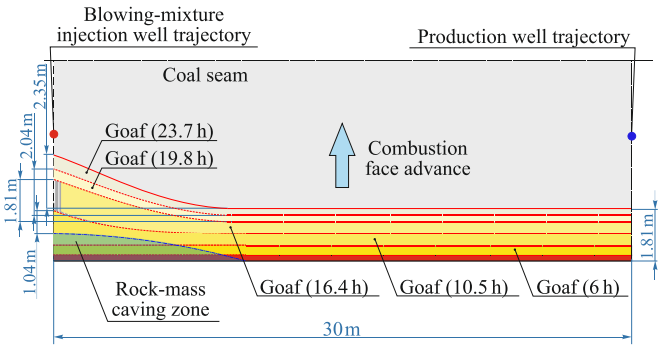

Figure 7. Schematic of combustion face advance at coal seam thickness m = 1.2 m, blowing-mixture injection pressure P = 0.65 MPa, and gasification duration t = 23.7 h

The CO concentration includes the contribution from the primary reaction, where CO is formed in the oxidizing zone. During the secondary reaction, CO is formed in the reducing zone involving carbon dioxide and carbon at gasifier channel wall temperatures of 800-1200°C. The CO content increases along the channel. After that, roof subsidence was recorded at different points of the seam roof, as shown in Figure 8.

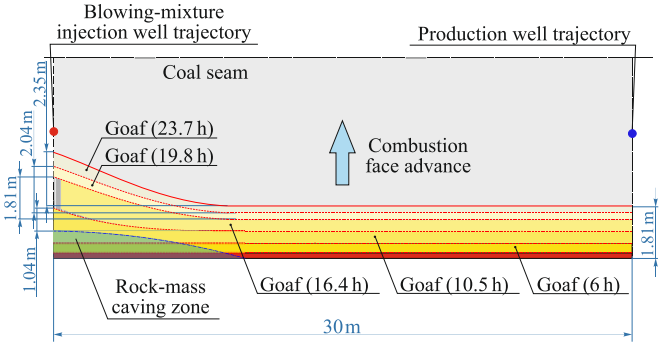

Figure 8. Schematic of combustion face advance at coal seam thickness m = 1.2 m; blowing-mixture injection pressure P = 0.45 MPa; nd gasification duration t = 29.2 h

Analysis of the data in Figure 8 indicates a decrease in the gasified space area. This decrease is associated with roof-rock caving that occurs at a specific step along the combustion face. Roof caving is non-uniform. In the reducing zone, the caving step varies from 1.23 to 1.37 m. In the oxidizing zone, it ranges from 1.4 to 2.75 m. The non-uniformity of the caving step is primarily due to temperature effects on the rock mass. During gasification of coal seams with thicknesses from 0.6 to 1.0 m, the caving-step parameters are similar. This indicates that temperature plays a decisive role in the roof-caving mechanisms. The obtained caving-step values are consistent with parameters reported previously [67, 68].

After roof caving was observed during the experiments, it was decided to reduce the blowing-mixture injection pressure to 0.4 MPa. During further gasification, after 11.2 h, the gas concentration decreased to 36.8%. When the pressure was increased to 0.47 MPa, the gas concentration began to rise. The same pattern was observed during gasification of seams with thicknesses from 0.6 to 1.0 m. At each stage of the experiments, four pressure-increase steps were recorded. These adjustments were made in response to changes in the gasified space size during the gasification process. Figure 9 presents the variation of the gasified space area S with gasification duration t and coal seam thickness m.

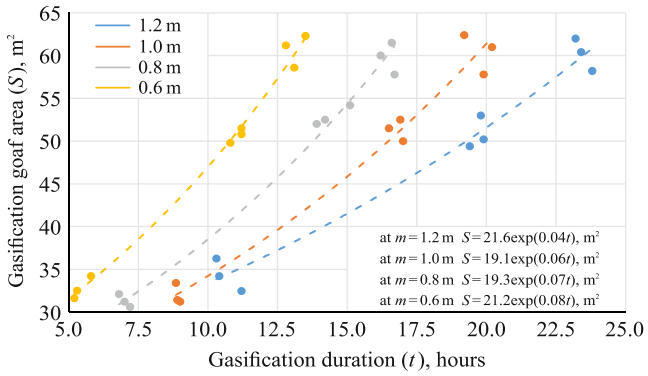

Figure 9. Relationships between the gasified space area and gasification duration and coal seam thickness

Analysis of the data in Figure 9 indicates an exponential increase in the gasified space area with gasification duration.

The established relationships enable the prediction of the gasified space expansion parameters as a function of gasification duration. They can also support controlled adjustment of underground coal gasification operating regimes, which improves process stability and efficiency.

4.3. Synthesis and implications for UCG process control and roof stability

The measured temperature pattern in the immediate roof along the combustion face reflects the canonical spatial separation of reaction zones in underground coal gasification. In UCG, the oxidizing zone near the injection side is dominated by exothermic oxidation reactions, which provide most of the heat input. Further downstream, the reducing zone is governed by endothermic gasification reactions that progressively consume heat, thereby reducing the thermal driving force for conductive heating of the surrounding rock mass. This zonation and the associated nonuniform heat release are widely reported as the main reasons for an asymmetric temperature field around the UCG reactor and for the presence of localized high gradients near the interface between exothermic and endothermic intervals [24, 69-71].

A key point for interpretation is that the temperatures reported in this study were registered in the roof rocks at 0.55 m above the coal seam rather than inside the reaction channel. Therefore, the absolute values in the roof are expected to be substantially lower than the commonly reported peak temperatures inside the UCG cavity, which may reach about 1000-1200°C depending on the operating regime and coal type. The observed maximum in the roof near the transition zone is nevertheless consistent with the general understanding that the highest thermal loading on the surrounding rocks is typically associated with the moving combustion front and the region of most intense change in reaction rate [24, 69, 70, 72].

The strength response of the immediate roof siltstone, namely a pronounced increase in uniaxial compressive strength toward the transition zone, followed by a decrease toward the production side, can be explained by competing temperature-driven mechanisms well known from high-temperature rock mechanics [73]. Many sedimentary rocks exhibit an initial strengthening stage as temperature increases, which is often attributed to dehydration, reduction of free and bound water, and changes in intergranular contacts that can temporarily increase stiffness and peak strength. With further thermal exposure, microcrack initiation and growth become dominant, driven by thermal expansion mismatch among mineral phases, thermal fatigue, and thermochemical alteration, which ultimately reduce strength and increase deformability. Comprehensive reviews and recent high-temperature datasets for siliciclastic rocks support this nonlinearity and the existence of temperature windows where strengthening and weakening may alternate depending on mineralogy, texture, and porosity [74, 75].

In the context of the present results, the peak strength near the transition zone is plausibly associated with the "strengthening-dominated" stage in the roof rock at the investigated offset distance. At the same time, the proximity of the peak temperature to ~573°C is noteworthy because it coincides with the α–β transition of quartz, which is often implicated in microcrack development and subsequent degradation in quartz-bearing rocks [76]. This supports the interpretation that the transition zone is not only the location of maximum thermal loading but also a likely trigger for accelerated damage accumulation. The downstream reduction in UCS toward the reducing zone can then be interpreted as the net effect of accumulated microdamage under repeated or prolonged heating and cooling, combined with stress redistribution caused by the evolving gasification goaf geometry [77, 78].

The dynamics of gasification goaf growth observed in the laboratory, including periods of rapid expansion and episodic decreases in effective area due to roof collapse, are consistent with the established concept that UCG cavity evolution is controlled by both chemical conversion of coal and thermo-mechanical failure of the surrounding materials. Cavity growth mechanisms discussed in the UCG literature typically include coal consumption, spalling from cavity walls and roof, rubble accumulation, and intermittent roof falls, which together produce a strongly nonlinear evolution of cavity shape and hydraulic connectivity. This nonlinearity is a core reason why many authors emphasize coupled thermo-mechanical modelling for predicting roof deformation, stress redistribution, and subsidence trends around UCG reactors [70, 71, 78-80].

The observed linkage between adjustments in blowing-mixture injection pressure and combustible gas concentration is also consistent with prior experimental and modelling studies. Laboratory UCG studies have demonstrated that operational changes in oxidant and steam delivery affect local temperatures, reaction rates, and, consequently, the syngas composition, including the balance between CO, H_2, CH_4, and CO_2. In particular, the expected roles of secondary reactions in the reducing zone, such as the Boudouard and water-gas reactions, provide a mechanistic explanation for changes in CO and H_2 yields along the reactor length. This supports the practical conclusion that process controllability requires adaptive operating regimes that respond to evolving goaf geometry and flow paths rather than fixed setpoints [66, 81-83].

From an engineering perspective, the combined trends in temperature and strength identified here highlight a critical implication for UCG design and monitoring. Even when the immediate roof experiences moderate temperatures relative to the cavity interior, localized gradients near the transition zone can produce the most pronounced changes in mechanical behaviour. Because cavity evolution and roof response are coupled, the gasification goaf geometry should be treated as a dynamic state variable in process control and in geomechanical risk assessment, particularly when evaluating the likelihood of roof falls that may alter permeability pathways and affect environmental containment.

5. Conclusions

Laboratory investigations established the spatial regularities of the temperature field in the immediate roof rocks of an underground gasifier, located 0.55 m above the coal seam. Within the oxidizing zone (0-9 m), temperature increases from approximately 323 to 550°C. In the transition zone (9-11 m), the maximum temperature gradient is observed, with temperatures reaching about 573°C. Within the reducing zone (11-30 m), temperature decreases to approximately 200°C. This profile reflects the change in the contribution of exothermic and endothermic reactions along the reaction channel.

It was shown that variations in the temperature regime across the combustion face lead to pronounced variability in the uniaxial compressive strength of the immediate roof rocks (siltstone). Strength increases in the oxidizing zone and attains a maximum near the transition zone, with an average value of about 14.75 MPa. In the reducing zone, strength decreases gradually toward the production well, reaching about 10 MPa.

The strength evolution should be described in a zone-specific manner rather than by a single generalised relationship. In the oxidizing zone, strength variation is best represented by an exponential function, reflecting intensive structural transformations in the rock, including dehydration and strengthening of intercrystalline contacts. In the reducing zone, strength changes are smoother and best described by a logarithmic function, consistent with the lower thermal impact intensity.

The formation and expansion of the gasification goaf were confirmed to be dynamic and strongly nonlinear. The gasification goaf area varies over time and is controlled by the combustion face advance rate, the blowing-mixture injection regime including pressure, and the coal seam thickness.

Under the investigated conditions, the increase in the gasification goaf area with gasification duration is predominantly exponential. This provides a basis for predicting the geometric parameters of the gasification goaf and for process control through adjustment of operating regimes.

It was demonstrated that stabilisation and correction of the blowing-mixture injection pressure are key factors for intensifying gasification. An increase in pressure is accompanied by a higher concentration of combustible components in the producer gas and promotes a more uniform advance of the combustion face.

Regularities of roof-rock caving were identified. They manifest as non-uniform caving steps along the combustion face and differ between the oxidizing and reducing zones. This confirms the controlling role of the temperature field in deformation and caving mechanisms and justifies incorporating the caving step into predictions of geomechanical stability and gasification goaf management.

Author contributions

Conceptualization: PS; Data curation: MB, DK; Formal analysis: VL, MB, DK; Funding acquisition: PS; Investigation: PS, VL; Methodology: PS; Project administration: PS; Resources: DK; Supervision: PS; Validation: VL, MB; Visualization: PS; Writing – original draft: PS, VL; Writing – review & editing: PS, VL, M.B, D.K. All authors have read and agreed to the published version of the manuscript.

Funding

The scientific and practical results presented, obtained within the framework of projects implemented by the Ministry of Education and Science of Ukraine “Geomechanical and technological foundations for the mining and processing of critical raw materials based on the principles of the circular economy” (No.0226U001998) and “Scientific substantiation and development of georeactor systems for the integrated processing of coal preparation waste with a focus on the recovery of critical raw materials” (No.0126U000998).

Acknowledgements

This study was conducted within the framework of the project “Belt and Road Initiative Center for Chinese-European Studies (BRICCES)” and was supported by the Guangdong University of Petrochemical Technology. The authors sincerely thank the Editor of the Engineering Journal of Satbayev University and the two reviewers for their valuable comments, constructive suggestions, and thorough evaluation of the manuscript, which significantly improved the quality of this work.

Conflicts of interest

Author VL declared that he was Deputy Editor in Chief of the Engineering Journal of Satbayev University at the time of submission. This had no impact on the peer review process and the final decision.

Data availability statement

The original contributions presented in this study are included in the article. Further inquiries can be directed to the corresponding author.

References

[1] Liu, Y., Li, Y., Jiang, J., Liu, F., & Liu, Y. (2026). Underground Coal Gasification Technology: A Review of Advantages, Challenges, and Economics. *Energies*, *19*(1), 199. https://doi.org/10.3390/en19010199

[2] Wang, D., Tian, J., Yang, S., Zou, J., Wei, B., Li, X., Tong, H., Zhang, Y., & Xu, C. (2026). Research review of underground coal gasification: principles, challenges and prospects. *Fuel*, *406*, 136823. https://doi.org/10.1016/j.fuel.2025.136823

[3] Saik, P., Dychkovskyi, R., Lozynskyi, V., Falshtynskyi, V., & Ovcharenko, A. (2024). Achieving climate neutrality in coal mining regions through underground coal gasification. *E3S Web of Conferences*, *526*, 01004. https://doi.org/10.1051/e3sconf/202452601004

[4] Falshtynskyi, V., Dychkovskyi, R., Saik, P., Lozynskyi, V., Sulaiev, V., & Cabana, E. C. (2019). The Concept of Mining Enterprises Progress on the Basis of Underground Coal Gasification Method Characteristic. *Solid State Phenomena*, *291*, 137-147. https://doi.org/10.4028/www.scientific.net/ssp.291.137

[5] Petlovanyi, M., Ruskykh, V., Sai, K., & Malashkevych, D. (2024). Prompt determination of predictive parameters for mining-technogenic landscape objects. *IOP Conference Series: Earth and Environmental Science*, *1348*(1), 012035. https://doi.org/10.1088/1755-1315/1348/1/012035

[6] Gorova, A., Pavlychenko, A., & Borysovs’ka, O. (2013). The study of ecological state of waste disposal areas of energy and mining companies. *Annual Scientific-Technical Colletion - Mining of Mineral Deposits*, 169-172. https://doi.org/10.1201/b16354-29

[7] Popovych, V., Voloshchyshyn, A., Lysyi, N., Petlovanyi, M., & Shuplat, T. (2024). Natural phytomelioration processes on rock dumps of abandoned coal mines (Ukraine). *Rudarsko-geološko-naftni zbornik*, *39*(5), 63-73. https://doi.org/10.17794/rgn.2024.5.4

[8] Pavlychenko, A., & Kovalenko, A. (2013). The investigation of rock dumps influence to the levels of heavy metals contamination of soil. *Annual Scientific-Technical Collection – Mining of Mineral Deposits*, 237-238. https://doi.org/10.1201/b16354-43

[9] Gorova, A., Pavlychenko, A., Kulyna, S., & Shkremetko, O. (2012). Ecological problems of post-industrial mining areas. *Geomechanical Processes During Underground Mining*, 35-40. https://doi.org/10.1201/b13157-7

[10] Hu, H. (2025). Research Progress and Future Development Direction of Deep Underground Coal Gasification. *Combustion Science and Technology*, 1-24. https://doi.org/10.1080/00102202.2025.2534442

[11] Cui, C., Liu, Y., Chai, X., & Tian, L. (2025). Investigation on performance characteristics and thermal analysis of underground coal gasification in porous media based on non-steady flow. *Fuel*, *389*, 134629. https://doi.org/10.1016/j.fuel.2025.134629

[12] Li, H., Cao, J., Tang, C., Guo, G., Chen, Y., Zha, J., Huang, W., Yuan, Y., & Huang, J. (2025). Methods for enhancing resource recovery efficiency in underground coal gasification to promote its large-scale utilization. *Geomechanics for Energy and the Environment*, *41*, 100651. https://doi.org/10.1016/j.gete.2025.100651

[13] Falshtynskyi, V.S., Dychkovskyi, R.O., Lozynskyi, V.H., Saik, P.B., & Lozynska, M.I. (2025). Substantiating applicability of Western Donbas coal seams (Ukraine) for underground coal gasification. *Engineering Journal of Satbayev University*, *147*(1), 31-42. https://doi.org/10.51301/vest.su.2025.i1.05

[14] Bondarenko, V., Lozynskyi, V., Sai, K., & Anikushyna, K. (2015). An overview and prospectives of practical application of the biomass gasification technology in Ukraine. *New Developments in Mining Engineering 2015: Theoretical and Practical Solutions of Mineral Resources Mining*, 27-32. https://doi.org/10.1201/b19901-6

[15] Salieiev, I., Bondarenko, V., Kovalevska, I., Malashkevych, D., & Galkov, R. (2025). Principles of mining-geological classification for maintaining mine workings in conditions of weakly metamorphosed rocks. *Mining of Mineral Deposits*, *19*(1), 26-36. https://doi.org/10.33271/mining19.01.026

[16] Lozynskyi, V. (2025). Multi-criteria assessment of coal seams suitability for co-gasification using the preference selection index. *Heliyon*, *11*(10), e43368. https://doi.org/10.1016/j.heliyon.2025.e43368

[17] Dychkovskyi, R., Dyczko, A., & Borojević Šoštarić, S. (2024). Foreword: Physical and Chemical Geotechnologies – Innovations in Mining and Energy. *E3S Web of Conferences*, *567*, 00001. https://doi.org/10.1051/e3sconf/202456700001

[18] Sakhno, I., Sakhno, S., & Vovna, O. (2025). Surface Subsidence Response to Safety Pillar Width Between Reactor Cavities in the Underground Gasification of Thin Coal Seams. *Sustainability*, *17*(6), 2533. https://doi.org/10.3390/su17062533

[19] Fedoreiko, V., Kravchenko, O., Sala, D., Zahorodnii, R., Pyzalski, M., & Dychkovskyi, R. (2026). Management and Optimization of Bio-Resource Decentralized Energy Generation Under Political Instability. *Energies*, *19*(3), 737. https://doi.org/10.3390/en19030737

[20] Lysyi, N., Helesh, A., Popovych, V., Saik, P., & Dmytruk, O. (2025). Thermodynamic research of coal mining waste gasification processes. *Mining of Mineral Deposits*, *19*(3), 132-143. https://doi.org/10.33271/mining19.03.132

[21] Lozynskyi, V., Saik, P., Petlovanyi, M., Sai, K., Malanchuk, Z. & Malanchuk, Y. (2018). Substantiation into mass and heat balance for underground coal gasification in faulting zones. *Inzynieria Mineralna*, *19*(2), 289-300. https://doi.org/10.29227/IM-2018-02-36

[22] Perkins, G. (2018). Underground coal gasification – Part I: Field demonstrations and process performance. *Progress in Energy and Combustion Science*, *67*, 158-187. https://doi.org/10.1016/j.pecs.2018.02.004

[23] Saik, P., Lozynskyi, V., Anisimov, O., Akimov, O., Kozhantov, A., & Mamaykin, O. (2023). Managing the process of underground coal gasification. *Naukovyi Visnyk Natsionalnoho Hirnychoho Universytetu*, (6), 25-30. https://doi.org/10.33271/nvngu/2023-6/025

[24] Bhutto, A.W., Bazmi, A.A., & Zahedi, G. (2013). Underground coal gasification: From fundamentals to applications. *Progress in Energy and Combustion Science*, *39*(1), 189-214. https://doi.org/10.1016/j.pecs.2012.09.004

[25] Tomás, R., Benavente, D., Martínez-Ibáñez, V., & Garrido, M. E. (2025). How do high temperatures affect rock properties? A comprehensive review of experimental thermal effects and underlying mechanisms. *Engineering Geology*, *357*, 108323. https://doi.org/10.1016/j.enggeo.2025.108323

[26] Ding, Q.L., Wang, P., & Cheng, Z. (2021). Influence of temperature and confining pressure on the mechanical properties of granite. *Powder Technology*, *394*, 10-19. https://doi.org/10.1016/j.powtec.2021.08.036

[27] Jin, J., Liu, J., Chen, W., Li, G., Cheng, W., Zhang, X., & Luo, Y. (2024). The impact of high temperature on mechanical properties and behaviors of sandstone. *Frontiers in Earth Science*, *12*, 1322495. https://doi.org/10.3389/feart.2024.1322495

[28] Bondarenko, V.I., Salieiev, I.A., Kovalevska, I.A., Vivcharenko, I.O., & Sheka, I.V. (2025). Substantiation of geomechanical principles for predicting outgassing during complex mining of mineral raw materials. *Mineral Resources of Ukraine*, (3), 10-16. https://doi.org/10.31996/mru.2025.3.10-16

[29] Abdiev, A.R., Wang, J., Mambetova, R.S., Abdiev, A.A., & Abdiev, A.S. (2025). Geomechanical assessment of stress-strain conditions in structurally heterogeneous rock masses of Kyrgyzstan. *Engineering Journal of Satbayev University*, *147*(2), 31-39. https://doi.org/10.51301/ejsu.2025.i2.05

[30] Kačur, J., & Kostúr, K. (2017). Approaches to the gas control in UCG. *Acta Polytechnica*, *57*(3), 182-200. https://doi.org/10.14311/ap.2017.57.0182

[31] Lozynskyi, V. (2024). Numerical simulation of carbonaceous raw material combustion in a coal seam channel. *Mining of Mineral Deposits*, *18*(4), 109-124. https://doi.org/10.33271/mining18.04.109

[32] Xiao, Y., Yin, J., Hu, Y., Wang, J., Yin, H., & Qi, H. (2019). Monitoring and Control in Underground Coal Gasification: Current Research Status and Future Perspective. *Sustainability*, *11*(1), 217. https://doi.org/10.3390/su11010217

[33] Saik, P.B., Dychkovskyi, R.O., Lozynskyi, V.G., Malanchuk, Z.R., & Malanchuk, Ye.Z. (2016). Revisiting the underground gasification of coal reserves from contiguous seams. *Naukovyi Visnyk Natsionalnoho Hirnychoho Universytetu*, (6), 60-66.

[34] Pershad, S., Pistorius, J., & van der Riet, M. (2018). Majuba underground coal gasification project. *Underground Coal Gasification and Combustion*, 469-502. https://doi.org/10.1016/b978-0-08-100313-8.00014-1

[35] Saik, P.B., & Berdnyk, M.H. (2024). Mathematical model for heat transfer during underground coal gasification process. *Naukovyi Visnyk Natsionalnoho Hirnychoho Universytetu*, (5), 19-24. https://doi.org/10.33271/nvngu/2024-5/019

[36] Lozynskyi, V. (2023). Critical review of methods for intensifying the gas generation process in the reaction channel during underground coal gasification (UCG). *Mining of Mineral Deposits*, *17*(3), 67-85. https://doi.org/10.33271/mining17.03.067

[37] Svetkina, Y., Falshtyns'kyy, V., & Dychkovs'kyy, R. (2010). Features of selectivity process of borehole underground coal gasification. *New Techniques and Technologies in Mining*, 219-222.

[38] Saik, P., & Berdnyk, M. (2024). mathematical model of temperature distribution in rock sample during heating. *Scientific papers of DonNTU Series: "The Mining and Geology*," 1(31)-2(32), 70-77. https://doi.org/10.31474/2073-9575-2024-1(31)-2(32)-70-77

[39] Fang, H., Liu, Y., Ge, T., Zheng, T., Yu, Y., Liu, D., Ding, J., & Li, L. (2022). A Review of Research on Cavity Growth in the Context of Underground Coal Gasification. *Energies*, *15*(23), 9252. https://doi.org/10.3390/en15239252

[40] Khan, M., Mmbaga, J., Shirazi, A., Trivedi, J., Liu, Q., & Gupta, R. (2015). Modelling Underground Coal Gasification – A Re-

view. *Energies*, *8*(11), 12603-12668. https://doi.org/10.3390/en81112331

[41] Falshtynskyi, V., Lozynskyi, V., Saik, P., Dychkovskyi, R., & Tabachenko, M. (2016). Substantiating parameters of stratification cavities formation in the roof rocks during underground coal gasification. *Mining of Mineral Deposits*, *10*(1), 16-24. https://doi.org/10.15407/mining10.01.016

[42] Saik, P., & Yankin, D. (2025). On the issue of the rational planning of mining operations for underground coal gasification. *Collection of Research Papers of the National Mining University*, *80*, 81-92. https://doi.org/10.33271/crpnmu/80.081

[43] Laciak, M., Kačur, J., & Durdán, M. (2022). Modeling and Control of Energy Conversion during Underground Coal Gasification Process. *Energies*, *15*(7), 2494. https://doi.org/10.3390/en15072494

[44] Dreus, A.Yu., Sudakov, A.K., Kozhevnikov, A.A., & Vakhalin, Yu.N. (2016). Study on thermal strength reduction of rock formation in the diamond core drilling process using pulse flushing mode. *Naukovyi Visnyk Natsionalnoho Hirnychoho Universytetu*, (3), 5-10.

[45] Lu, Y., & Cha, M. (2022). Thermally induced fracturing in hot dry rock environments-Laboratory studies. *Geothermics*, *106*, 102569. https://doi.org/10.1016/j.geothermics.2022.102569

[46] Shahbazi, M., Najafi, M., Fatehi Marji, M., & Abdollahipour, A. (2025). Thermo-Mechanical Analysis of Crack Propagation Process in Heterogeneous Brittle Coal and Its Effects on the UCG Cavity Growth Rate. *Energy Science & Engineering*, *13*(3), 1062-1078. https://doi.org/10.1002/ese3.2002

[47] Xin, L., Li, H., Niu, M., Yang, M., Xu, W., Wang, X., & Diao, T. (2025). Experimental and numerical investigation of thermal cracking of overlying rock in underground coal gasification. *Engineering Fracture Mechanics*, *315*, 110808. https://doi.org/10.1016/j.engfracmech.2025.110808

[48] Wu, J., Xu, H., Cao, C., Chen, Y., Xin, F., & Yin, Z. (2026). A novel method for predicting permeability in quartz-bearing rocks at high temperatures during underground coal gasification. *Fuel*, *404*, 136195. https://doi.org/10.1016/j.fuel.2025.136195

[49] Bukowska, M., & Sygała, A. (2015). Deformation properties of sedimentary rocks in the process of underground coal gasification. *Journal of Sustainable Mining*, *14*(3), 144-156. https://doi.org/10.1016/j.jsm.2015.11.003

[50] Chepiga, D., Podkopaiev, S., Gogo, V., Shashenko, O., Skobenko, O., Demchenko, O., & Podkopayev, Y. (2024). Dualistic effect of the deformation of protective structures made of broken rock in mine workings under static load. *Mining of Mineral Deposits*, *18*(2), 122-131. https://doi.org/10.33271/mining18.02.122

[51] Liu, S., Zhang, S., Chen, F., Wang, C., & Liu, M. (2014). Variation of coal permeability under dehydrating and heating: a case study of ulanqab lignite for underground coal gasification. *Energy & Fuels*, *28*(11), 6869-6876. https://doi.org/10.1021/ef501696e

[52] Ma, H., Song, Y., Yang, J., Zheng, J., Shen, F., & Shao, Z. (2023). Experimental investigation on acoustic emission and damage characteristics of dehydrated lignite in uniaxial compression test. *Bulletin of Engineering Geology and the Environment*, *82*(8), 292. https://doi.org/10.1007/s10064-023-03315-z

[53] Luo, J., & He, J. (2022). Mechanical characteristics of sandstone under high temperature and cyclic loading in underground coal gasification. *Minerals*, *12*(10), 1313. https://doi.org/10.3390/min12101313

[54] Feng, G., Wang, X., Kang, Y., Luo, S., & Hu, Y. (2019). Effects of temperature on the relationship between mode-I fracture toughness and tensile strength of rock. *Applied Sciences*, *9*(7), 1326. https://doi.org/10.3390/app9071326

[55] Zhang, L., Mao, X., & Lu, A. (2009). Experimental study on the mechanical properties of rocks at high temperature. *Science in China Series E: Technological Sciences*, *52*(3), 641-646. https://doi.org/10.1007/s11431-009-0063-y

[56] Yavuz, H., Demirdag, S., & Caran, S. (2010). Thermal effect on the physical properties of carbonate rocks. *International Journal of Rock Mechanics and Mining Sciences*, *47*(1), 94-103. https://doi.org/10.1016/j.ijrmms.2009.09.014

[57] Sygała, A., Bukowska, M., & Janoszek, T. (2021). High temperature versus geomechanical parameters of selected rocks – the present state of research. *Journal of Sustainable Mining*, *12*(4), 9. https://doi.org/10.46873/2300-3960.1291

[58] Chen, Y.-L., Ni, J., Shao, W., & Azzam, R. (2012). Experimental study on the influence of temperature on the mechanical properties of granite under uniaxial compression and fatigue loading. *International Journal of Rock Mechanics and Mining Sciences*, *56*, 62-66. https://doi.org/10.1016/j.ijrmms.2012.07.026

[59] Korzeniowski, W., & Skrzypkowski, K. (2012). Investigations of changes of selected geo-mechanical properties of rocks under the influence of temperature up to 1100 ºC in the aspect of potential underground coal gasification process. *Przeglad Gorniczy*, (68), 44-53.

[60] Zhang, L., Mao, X., Liu, R., Guo, X., & Ma, D. (2013). The mechanical properties of mudstone at high temperatures: an experimental study. *Rock Mechanics and Rock Engineering*, *47*(4), 1479-1484. https://doi.org/10.1007/s00603-013-0435-2

[61] Małkowski, P., Niedbalski, Z., & Hydzik-Wiśniewska, J. (2013). Zmiany właściwości strukturalnych i cieplnych skał poddanych wysokim temperaturom w rejonie projektowanego georeaktora. *Archives of Mining Sciences*, *58*(2), 465-480. https://doi.org/10.2478/amsc-2013-0031

[62] Mao, X., Zhang, L., Li, T., & Liu, H. (2009). Properties of failure mode and thermal damage for limestone at high temperature. *Mining Science and Technology (China)*, *19*(3), 290-294. https://doi.org/10.1016/s1674-5264(09)60054-5

[63] Guo, J., Lei, Y., Yang, Y., Cheng, P., Wang, Z., & Wu, S. (2023). Effects of high temperature treatments on strength and failure behavior of sandstone under dynamic impact loads. *Sustainability*, *15*(1), 794. https://doi.org/10.3390/su15010794

[64] Bukowska, M., & Sygała, A. (2021). Deformation properties of sedimentary rocks in the process of underground coal gasification. *Journal of Sustainable Mining*, *14*(3). https://doi.org/10.46873/2300-3960.1239

[65] Brovko, D., Makareiko, R., Sakhno, S., Yanova, L., & Pischikova, O. (2024). Modeling the stability of air flows in inclined workings in case of fire. *Mining of Mineral Deposits*, *18*(3), 52-62. https://doi.org/10.33271/mining18.03.052

[66] Dychkovskyi, R., Falshtynskyi, V., Saik, P., Lozynskyi, V., Sala, D., Hankus, Ł., Magdziarczyk, M., & Smoliński, A. (2025). Control of contour evolution, burn rate variation, and reaction channel formation in coal gasification. *Scientific Reports*, *15*(1). https://doi.org/10.1038/s41598-025-93611-3

[67] Kadirov, V.R., Nurboboev, Y.T., Umirzoqov, A.A., Muhammadiyev Elbek (2022). Rock displacement at underground coal gasification. *International Journal on Human Computing Studies*, *1*(4), 72-82. https://doi.org/10.31149/ijhcs.v4i1.2688

[68] Bondarenko, V., Dychkovskiy, R., & Falshtynskiy, V. (2009). Synthetic stowing of rockmass at borehole underground coal gasification (BUCG). *Deep Mining Challenges*, 169-177. https://doi.org/10.1201/NOE0415804288-24

[69] Couch, G.R. (2009). Underground coal gasification. IEA Clean Coal Centre, London, UK. Report No. *Contract No.: CCC/151*, 129.

[70] Perkins, G. (2018). Underground coal gasification–Part II: Fundamental phenomena and modeling. *Progress in Energy and Combustion Science*, *67*, 234-274. https://doi.org/10.1016/j.pecs.2018.03.002

[71] Yang, D., Sarhosis, V., & Sheng, Y. (2014). Thermal-mechanical modelling around the cavities of underground coal gasification. *Journal of the Energy Institute*, *87*(4), 321-329. https://doi.org/10.1016/j.joei.2014.03.029

[72] Prabu, V., & Jayanti, S. (2014). Heat-affected zone analysis of high ash coals during ex situ experimental simulation of underground coal gasification. *Fuel*, *123*, 167-174. https://doi.org/10.1016/j.fuel.2014.01.035

[73] Ishchenko, O., Novikov, L., Ponomarenko, Y., Konoval, V., Kinasz, R., & Ishchenko, K. (2026). Research into fracture mechanism of complex-structured crystalline mass under triaxial compression. *Mining of Mineral Deposits*, *20*(1), 1-12. https://doi.org/10.33271/mining20.01.001

[74] Zhang, Y., Zhang, C., Jia, J., & Zhou, C. (2024). Experimental investigation of high-temperature effects on the physical and mechanical properties of granite, sandstone, and limestone. *Applied Energy*, *357*, 122532. https://doi.org/10.1016/j.apenergy.2023.122532

[75] Birawidha, D.C., Amin, M., Miswanto, A., Jaya, F.H., Dewi, S.U., Nariswari, M.K., & Putri, D.M. (2025). Variations in alumina-based material composition and heating temperature of refractory bricks in mullite formation. *Mining of Mineral Deposits*, *19(*4), 130-138. https://doi.org/10.33271/mining19.04.130

[76] Peng, Z., & Redfern, S.A.T. (2013). Mechanical properties of quartz at the α–β phase transition: Implications for tectonic and seismic anomalies. Geochemistry, Geophysics, *Geosystems*, *14*(1). doi: https://doi.org/10.1029/2012GC004482

[77] Elahi, S. M., Nassir, M., & Chen, Z. (2017). Effect of various coal constitutive models on coupled thermo-mechanical modeling of underground coal gasification. *Journal of Petroleum Science and Engineering*, *154*, 469-478. https://doi.org/10.1016/j.petrol.2017.02.016

[78] Otto, C., & Kempka, T. (2015). Thermo-Mechanical Simulations of Rock Behavior in Underground Coal Gasification Show Negligible Impact of Temperature-Dependent Parameters on Permeability Changes. *Energies*, *8*(6), 5800-5827. https://doi.org/10.3390/en8065800

[79] Daggupati, S., Mandapati, R. N., Mahajani, S. M., Ganesh, A., Mathur, D. K., Sharma, R. K., & Aghalayam, P. (2010). Laboratory studies on combustion cavity growth in lignite coal blocks in the context of underground coal gasification. *Energy*, *35*(6), 2374-2386. https://doi.org/10.1016/j.energy.2010.02.015

[80] Prabu, V., & Jayanti, S. (2014). Heat-affected zone analysis of high ash coals during ex situ experimental simulation of underground coal gasification. *Fuel*, *123*, 167-174. https://doi.org/10.1016/j.fuel.2014.01.035

[81] Falshtynskyi, V., & Dychkovskyi, R. (2014). Some aspects of technological processes control of an in-situ gasifier during coal seam gasification. *Progressive Technologies of Coal, Coalbed Methane, and Ores Mining*, 109-112. https://doi.org/10.1201/b17547-20

[82] Daggupati, S., Mandapati, R.N., Mahajani, S.M., Ganesh, A., Sapru, R.K., Sharma, R.K., & Aghalayam, P. (2011). Laboratory studies on cavity growth and product gas composition in the context of underground coal gasification. *Energy*, *36*(3), 1776-1784. https://doi.org/10.1016/j.energy.2010.12.051

[83] Kumari, G., & Vairakannu, P. (2017). Laboratory scale studies on CO2 oxy-fuel combustion in the context of underground coal gasification. *Journal of CO2 Utilization*, *21*, 177-190. https://doi.org/10.1016/j.jcou.2017.06.021

Температуралық-беріктік өзгерістердің тікелей төбе жыныстарындағы динамикасы және жерасты газ генераторы астындағы газсызданған кеңістіктің қалыптасуы

П. Саик[1,2], В. Лозинский[1,2*], М. Берник[1], Д. Климов[1]

[1]*«Бір бел, бір жол» бастамасы Қытай-Еуропа зерттеулер орталығы (BRICCES), Гуандунь мұнай-химия технологиялары университеті, Маомин, Қытай*

[2]*Ұлттық «Днепровск политехникасы» техникалық университеті, Днепр, Украина*

**Корреспонденция үшін автор: lozynskyi.v.h@nmu.one*

Аңдатпа. Жұмыстың мақсаты – отты кенжарбойындағы химиялық реакциялар аймақтарының әсерінен тікелей төбе жыныстарының температуралық өрісі мен беріктігінің өзгеру заңдылықтарын анықтау, сондай-ақ газификацияның ұзақтығына, үрлеу қоспасын беру қысымына және көмір қабатының қалыңдығына байланысты газсызданған кеңістік ауданының уақыт бойынша қалыптасуы мен өзгеру тәуелділіктерін белгілеу. Зерттеулер отты кенжар фронтының ілгерілеуі мен төбе жыныстары деформацияларын қайта жаңғырта отырып, жерасты газификациясының зертханалық қондырғысында орындалды. Модельденген тікелей төбеде температура реакциялық арна бойымен термодатчиктер арқылы тіркелді. Украина, «Львовуголь» МК (ГП) құрамындағы «Межиричанская» шахтасының $n_7^н$ қабатының тікелей төбесінен алынған алевролит үлгілері термиялық өңдеуден өткізіліп, KL 200/CE-Tecnotest прессінде біросьті сығуға сынақтан өткізілді. Газсызданған кеңістіктің геометриясы төбенің төмен түсуін өлшейтін реперлік датчиктер деректері, әртүрлі уақыт мезеттеріндегі контурларды графикалық визуализациялау және генераторлық газдың құрамы мен концентрациясын ескере отырып, трапециялар әдісімен ауданды есептеу негізінде анықталды. $n_7^н$ қабатынан 0,55 м қашықтықта тотығу аймағында (0–9 м) температура шамамен 323-тен 550°C-қа дейін өсетіні, өтпелі аймақта (9–11 м) шамамен 573°C-қа жететіні, ал қалпына келтіру аймағында (11–30 м) ~200°C-қа дейін төмендейтіні анықталды. Алевролиттердің беріктігі кенжар бойымен өтпелі аймақ маңында максимумға жетіп, кейін қалпына келтіру аймағында азаяды; бұл ретте тотығу аймағы үшін экспоненциалдық, ал қалпына келтіру аймағы үшін логарифмдік тәуелділік тән. Газсызданған кеңістік ауданының газификация ұзақтығына және қабат қалыңдығына байланысты сызықтық емес, негізінен экспоненциалды түрде өзгеретіні және үрлеу қоспасын беру қысымы режимімен әрі төбе жыныстарының құлау көріністерімен байланысты екені көрсетілді. Алынған заңдылықтар жерасты газификациясының басқарылатын режимдерін негіздеу кезінде газсызданған кеңістік параметрлерін болжау және төбенің орнықтылығын бағалау үшін пайдаланылуы мүмкін.

Негізгі сөздер: *көмірдің жерасты газификациясы, газсызданған кеңістік, температуралық өріс, тау жыныстары, біросьті сығуға беріктік, отты кенжар.*

Динамика температурно-прочностных изменений непосредственной кровли и формирование выгазованного пространства подземного газогенератора

П. Саик[1,2], В. Лозинский[1,2*], М. Берник[1], Д. Климов[1]

[1]*Центр китайско-европейских исследований инициативы «Пояс и путь» (BRICCES), Гуандунский университет нефтехимических технологий, Маомин, Китай*

[2]*Национальный технический университет «Днепровская политехника», Днепр, Украина*

**Автор для корреспонденции: lozynskyi.v.h@nmu.one*

Аннотация. Целью работы является установление закономерностей изменения температурного поля и прочности пород непосредственной кровли под воздействием зон химических реакций вдоль огневого забоя, а также определение зависимостей формирования и изменения площади выгазованного пространства во времени в зависимости от продолжительности газификации, давления подачи дутьевой смеси и мощности угольного пласта. Исследования выполнены на лабораторной установке подземной газификации с воспроизведением продвижения фронта огневого забоя и деформаций кровли. Температуру в смоделированной непосредственной кровле регистрировали термодатчиками вдоль реакционного канала. Образцы алевролитов из непосредственной кровли пласта $n_7^н$ шахты «Межиричанская» (ГП «Львовуголь», Украина) подвергали термообработке и испытывали на одноосное сжатие на прессе KL 200/CE-Tecnotest. Геометрию выгазованного пространства определяли по данным реперных датчиков опускания кровли, графической визуализации контуров в различные моменты времени и расчета площади методом трапеций с учетом состава и концентрации генераторного газа. Установлено, что на расстоянии 0,55 м от пласта температура в окислительной зоне (0-9 м) возрастает примерно от 323 до 550°C, в переходной зоне (9-11 м) достигает около 573°C, а в восстановительной зоне (11-30 м) снижается до ~200°C. Прочность алевролитов изменяется вдоль забоя с максимумом в районе переходной зоны и последующим уменьшением в восстановительной зоне, причем для окислительной зоны характерна экспоненциальная, а для восстановительной – логарифмическая зависимость. Показано, что площадь выгазованного пространства изменяется нелинейно, преимущественно экспоненциально, в зависимости от продолжительности газификации и мощности пласта и связана с режимом давления подачи дутьевой смеси и проявлениями обрушения пород кровли. Полученные закономерности могут быть использованы для прогнозирования параметров выгазованного пространства и оценки устойчивости кровли при обосновании управляемых режимов подземной газификации.

Ключевые слова: *подземная газификация угля; выгазованное пространство; температурное поле; горные породы; прочность на одноосное сжатие; огневой забой.*

Publisher's note

All claims expressed in this manuscript are solely those of the authors and do not necessarily represent those of their affiliated organizations, or those of the publisher, the editors and the reviewers.

SATBAYEV UNIVERSITY

Engineering Journal of Satbayev University

Volume 148 (2026), Issue 1, 29-37

https://doi.org/10.51301/ejsu.2026.i1.04

Hydrogeological characteristics of the Alakol groundwater deposit for resort infrastructure development

M.M. Alzhigitova*, E.M. Kuldeyeva, A.Zh. Ismagulova, M.R. Zapparov, N. Tleuberdi

Satbayev University, Almaty, Kazakhstan

**Corresponding author: m.alzhigitova@satbayev.university*

Abstract. The paper presents the results of a comprehensive geological and hydrogeological assessment of the Alakol groundwater deposit in the Alakol Depression, southeastern Kazakhstan. This deposit represents one of the principal groundwater sources for the rapidly developing resort infrastructure on the southern shore of Lake Alakol. It is therefore of considerable socio-economic importance for the region. The study examines the geomorphological setting of the area, the lithological composition and thickness of aquifer-bearing deposits, groundwater occurrence conditions, and the main factors governing groundwater recharge, flow, and discharge. The groundwater regime in both recharge and discharge zones is characterized, and the principal filtration flow directions and hydraulic relationships between groundwater and surface waters are identified. In addition, the paper evaluates the configuration of existing water intake facilities, groundwater abstraction rates, and the influence of pumping on the regional hydrogeological balance. Particular attention is paid to the rational use and protection of groundwater resources under conditions of increasing recreational pressure. The results may serve as a scientific basis for the further development of resort infrastructure and sustainable groundwater management in the southern coastal zone of Lake Alakol.

Keywords: *groundwater; groundwater regime; aquifers; groundwater balance; water intake, deposit.*

Received: 12 August 2025
Accepted: 14 February 2026
Available online: 28 February 2026

1. Introduction

Ensuring a sustainable water supply in arid regions of Kazakhstan, such as the foothill plains of the Dzungarian Alatau, is a key task of regional development. In conditions of surface water scarcity, the rational use of groundwater becomes particularly important, especially for agricultural and irrigated farming needs. The problem is exacerbated by the fact that most of the land suitable for agricultural use is located above the zone where spring water flows form, where natural moisture is insufficient, and supplying water through traditional irrigation canals is associated with high financial costs. Taking these factors into account, the development of oasis irrigation based on groundwater is becoming a priority. Such work enables effective use of water resources in areas far from swampy or saline areas, creating favorable engineering and geological conditions and minimizing the risk of flooding. Of particular interest is the experience with groundwater from the Alakol deposit, which is considered one of the key sources of water supply and irrigation in the region [1].

This article discusses the characteristics of water intakes, the geological conditions at their locations, and the prospects for using groundwater for sustainable agricultural development in the region. In geological and structural terms, the exploration area lies in the southwestern part of the vast Alakol intermountain basin, which is bounded on the southwest by the Dzungarian Fault. To the northeast, beyond the study area's boundaries, lies the Tarbagatai mountain range. The Alakol Depression is composed of a thick layer of loose Cenozoic sediments and, in turn, within the territory of the Alakol groundwater deposit, is located on a provincial sloping plain formed by sediments from large and small rivers flowing down from the northeastern slopes of the Dzungarian Alatau, and on flat alluvial-lake and partially lake plains formed as a result of periodic transgressions of ancient and modern lake basins. The largest lakes bordering the deposit, Sasykkol and Alakol, are at the same hypsometric level, 347 and 340 m, respectively. Therefore, there is a weak flow from Lake Sasykkol to Lake Alakol through a system of intermediate lakes (Uyaly, Kashkarkol, etc.). The shores of the lakes are mostly low and marshy, only in the south, where Lake Alakol erodes the foothill plain, its shores are steep and precipitous [2]. The depth of hand-dug valleys within the deposit varies from several tens of meters in the upper part of the foothill plain to 5-10 m at its periphery and up to 1-2 m in the deltas. The study area covers the coastal zone of Lake Alakol and adjacent land areas. From the southwest, the boundaries of the area run along the 800 m contour line to the outlet of the Tenteq River alluvial fan.

In the village of Zhaypak, the boundary follows the 380 m contour line, bypassing areas under irrigated agriculture. Near the village of Kainar, it reaches the southern shore of Lake Koshkarkol, crosses the Shubartobek tract, and then

m.alzhigitova@satbayev.university; e.kuldeyeva@satbayev.university; a.ismagulova@satbayev.university; m.zapparov@satbayev.university; n.tleuberdi@satbayev.university
Engineering Journal of Satbayev University. eISSN 2959-2348. Published by Satbayev University

follows the shoreline of this lake. In the area of the village of Uyal, the border runs along the northern shore of Lake Alakol, including the Urzhar River delta, the Uyal River floodplain, and continues to the village of Koktal, located approximately 8 km from the shoreline [3]. Then the line runs horizontally for 360 m, crossing the Emel River floodplain and the Kossayshagyl tract. The eastern border runs along a 400 m contour line to the southern part of the Yrgayty River delta, then turns southwest and continues until it intersects with the 800 m contour line (Figure 1).

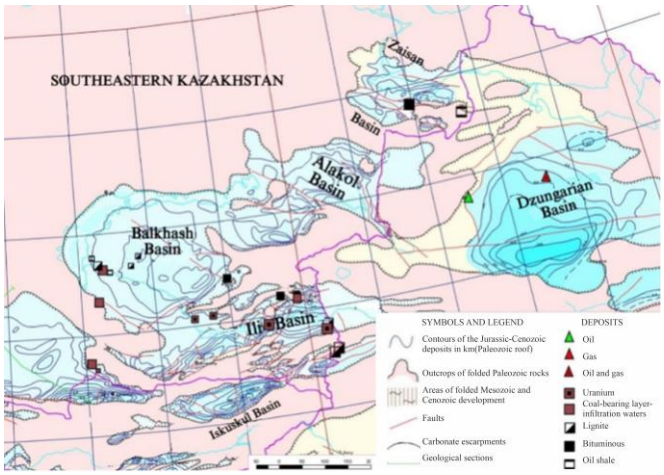

Figure 1. Example map of the Alakol depression

From a structural-tectonic perspective, the Alakol underground water deposit is confined to the southwestern structural zone, which is oriented northwesterly. This zone is a typical foreland depression formed because of prolonged tectonic subsidence. On the northern and northeastern sides, the deposit is bounded by a central tectonic zone that manifests as a mountainous uplift, also elongated in a northwesterly direction.

Based on drilling and geophysical studies of the roof of the Miocene-Pliocene deposits, composed mainly of clayey rocks, at least two additional tectonic uplifts have been identified. These structures are transitional forms between the central and southwestern zones and confirm the complex structure of the aquifer roof [4].

Significant faults, such as the Dzungarian Fault (in the southwest) and the Central Zone Fault (in the northeast), played a key role in shaping the deposit's hydrogeological structure. They caused significant subsidence of the earth's crust, contributed to the accumulation of a thick layer of coarse-grained alluvial deposits, and created favorable conditions for the formation of aquifers. Currently, these tectonic structures serve as natural hydrogeological boundaries of the deposit [5].

From a stratigraphic point of view, the Alakol underground water deposit is confined to a complex of alluvial-proluvial and alluvial-lacustrine deposits of the Quaternary system, which form the upper structural-hydrogeological level in the Alakol artesian basin section. Within the deposit, Quaternary deposits are represented by all stratigraphic subdivisions, from the lower to the modern, but their contributions to groundwater formation and accumulation vary significantly.

Lower Quaternary deposits lie on top of Pliocene and Miocene-Pliocene rocks and comprise two main facies: alluvial-proluvial and lacustrine-alluvial. The thickness of these deposits varies from 70 m on the elevated tectonic blocks in the northern part of the field to 190-200 m in the central, tectonically depressed areas and in the axial zones of the Tente and Zhamantinsky cones [6-7].

Alluvial-proluvial deposits associated with mountain foothills are composed mainly of a homogeneous layer of boulder-pebble material with high filtration capacity. As one moves away from the mountain front, layers of loam with lower permeability appear in the section, contributing to the formation of local areas of groundwater accumulation [8].

Alluvial-lacustrine deposits, along with clayey and gravelly rocks, widely contain sands and sandy loams, which play an essential role in the formation of aquifers. Middle Quaternary deposits are similar to Lower Quaternary deposits in terms of lithological and facies characteristics, but differ in their increased thickness. In the foothill areas, their thickness reaches 300 m, decreasing to 120-150 m in the north. These data are confirmed by the geological section (Figure 2).

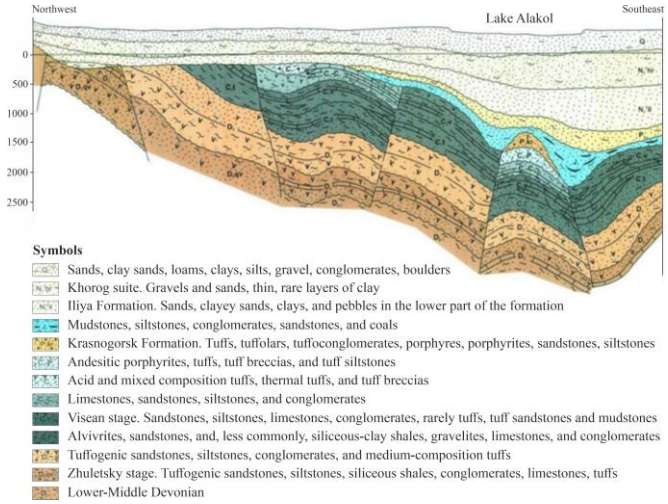

Figure 2. Geological section of the Alakol depression NW-SE

Therefore, this study aims to provide a comprehensive hydrogeological assessment of the Alakol groundwater deposit as a water supply source for the resort infrastructure of the southern Lake Alakol coastal zone. The study examines the geological and hydrogeological setting of the deposit, the structure and hydraulic connectivity of aquifers, groundwater regime features, recharge and discharge components, and the suitability of groundwater for practical use.

2. Materials and methods

The study is based on a comprehensive analysis of geological, hydrogeological, engineering geological, and climatic data obtained from open geoinformation sources, archival materials from hydrogeological surveys, and modern remote and field observations. The following methods were used in the course of the work.

Interpretation of stratigraphic and lithological sections of Quaternary deposits based on archival drilling data.

Classification of groundwater regimes according to D.M. Kats' scheme, adapted to the conditions of the Alakol Depression. Classification of groundwater regimes (according to D.M. Kats' scheme, adapted to the conditions of the Alakol Depression).

The method for classifying groundwater regimes proposed by D.M. Kats is widely used in hydrogeological studies. It is based on an analysis of fluctuations in levels, recharge sources, water yield characteristics, and seasonal dynamics. According to this scheme, the following types of groundwater regimes are distinguished (Table 1).

Table 1. Types and characteristics of groundwater regimes in the Alakol Depression

№	Area / plot	Type of groundwater regime	Mode characteristics
1	Koktuma tract	Free	Groundwater reacts quickly to precipitation and fluctuations in lake level.
2	The area of the village Akshi	Semi-stable	The water level is weakly dependent on precipitation; it feeds from afar
3	The central part of the coast	Mixed	Combined type of nutrition, moderate fluctuations in levels
4	The eastern section of the coast	Free	Intensive nutrition due to infiltration of precipitation and lake water
5	West of the village. Kabanbai	Semi-stable	Low seasonal fluctuations, weak connection with surface waters

Three groundwater regimes have been established in the Alakol Depression, adapted to local natural features. The most stable groundwater regime is observed in the lake-alluvial zone- these areas can be used for the permanent water supply of resort infrastructure facilities.

The most vulnerable areas are dune and coastal zones, where sharp drops in water levels and the risk of pollution are possible. Alluvial fans, despite fluctuations, are highly productive and can be used effectively with the proper water intake and regulation system. Methods used for the hydrogeological assessment of the Alakol groundwater deposit. The research methods included:

1) Conducting preliminary and detailed exploration of the Alakol underground water deposit. During the exploration work, four exploratory and experimental production wells were drilled, experimental work was conducted to assess the water yield and filtration capacity of the aquifers, and groundwater level and quality were monitored.

2) Analysis of groundwater regime. The classification of the groundwater regime of the deposit is based on the scheme developed by D.M. Kats, with modifications tailored to the deposit's specific conditions. This scheme takes into account the interaction of natural and artificial regime-forming factors. The groundwater regime is considered separately for the zone of its formation and discharge.

3) Assessment of groundwater conditions and balance. The groundwater balance equation for the deposit was recorded as follows:

$$q_f + x_i + Q_1 = E + q_{dr} + Q_2, \quad (1)$$

where: q_f is surface water filtration; x_i is atmospheric precipitation infiltration; Q_1 is underground inflow; E is evaporation of groundwater; q_{dr} is groundwater drainage; Q_2 is underground drainage.

To determine surface runoff losses, data from UGMs and temporary hydrometric stations operated by the expedition's hydrological team were used. The station on the Tentek River – the Tunkuruz collective farm, which has been operating since 1932, was taken as the reference point. To align the data from other stations with the long-term series, a 44-year reference period (1932-1977) was selected for the Tente River (Tunkuruz station). These data were used to determine the corrective relationships between the reference and other hydrological stations, regression equations, relationship graphs, tables for calculating the ordinates of the theoretical supply curve, and supply curves for the average annual discharge of rivers and streams.

The source materials for determining evaporation from the groundwater level were lysimeter observations at the Aksu groundwater deposit and a map of groundwater depths based on actual survey and exploration data. Evaporation graphs of groundwater levels for various vegetation types, based on groundwater depth, were used for the Aksu deposit. These data were subsequently used to estimate evaporation from the Alakol groundwater deposit, which has conditions similar to those of the Aksu deposit.

4) Assessment of groundwater quality. To characterize the quality of groundwater at the site and determine its suitability for irrigation, its primary purpose, and possible domestic and drinking water supply, water samples were taken during pumping from wells for general, spectral, and complete chemical analysis. In addition, samples were collected to determine trace element content, and radiological and bacteriological analyses were performed. The sampling methodology, as well as the methods for determining the content of chemical elements and bacteriological indicators, were carried out in accordance with the requirements of GOST 18963-73 and GOST 4979-49 (31.32). According to the requirements for groundwater quality used for irrigation, mineralization should not exceed 2.5 g/L. When the sodium and potassium cation content exceeds 70% of the total cation content, it should not exceed 1.5 g/l. The temperature of groundwater for irrigation should not exceed +350°C, and the irrigation coefficient should not be less than 18. The content of the main components determined in groundwater intended for water supply, as well as the permissible concentrations of several chemical substances entering water sources with domestic, industrial, and agricultural pollution, organoleptic and bacteriological indicators are controlled by GOST 2762-57, 2874-73, and since July 1, 1978, by GOST 17.13.03-77. Engineering-geological assessment of the stability of areas near proposed water intakes, taking into account geomorphological factors (slopes, flooding, erosion, seismic activity).

Hydrogeological zoning – aquifers suitable for exploitation have been identified. Groundwater in the deposit accumulates mainly in Lower and Middle Quaternary sediments. Based on stratigraphic and genetic characteristics, the following aquifers have been identified:

– Lower Quaternary alluvial
– proluvial deposits;
– Lower Quaternary alluvial-lacustrine deposits;
– Middle Quaternary alluvial-proluvial deposits;
– Middle Quaternary alluvial-lacustrine deposits.

In hydrogeological terms, these aquifers form a virtually single entity (aquifer complex). Near the mountains, this is a homogeneous layer of boulder and pebble deposits, in which the groundwater has a common free surface. At some distance from the mountains, the single aquifer is divided into separate aquifers in the form of lenses separated by relatively impermeable interlayers. At the same time, the aquifers are hydraulically connected [9].

3. Results and discussion

The groundwater regime was analyzed based on data from 18 observation and exploration wells drilled in 1976–1978. Four single and seven paired wells are located in the recharge zone, mainly on the alluvial fans of the Tentek and Zhamanta rivers. Wells No. 201 and 202a (310 and 307 m deep) overlap the Lower and Middle Quaternary aquifers. Well No. 208, located in the inter-cone space, is equipped with filters at depths of 156–186 m and reflects the behavior of the Middle Quaternary horizon.

The regime in these wells is characterized by low-amplitude level fluctuations due to the deep location of the filters and by the smoothing effect of infiltration flows from irrigation and rivers. The main rise in groundwater levels is recorded in June–September, coinciding with the irrigation season and the flood period. Minimum levels are observed in winter, which is associated with the cessation of water supply and the winter low water period. In general, stable water yield is recorded, and levels stabilize at the same marks annually, indicating the presence of a single aquifer system in the recharge zone. In the discharge zone, where irrigation is not used, four types of regimes are observed. Hydrological fluctuations in levels are associated with the water level in the Tentek River.

The amplitudes range from 0.5 to 1.6 m. Climatic-seasonal fluctuations are caused by meltwater runoff and spring atmospheric precipitation, and by evaporation in summer. Amplitude is 0.8-1.6 m. Irrigation – sharp rises in levels during the irrigation period (May-September), with an amplitude of 0.7-1.2 m. Characteristic of the isthmus between Lake Koshkarkol and Lake Alakol; levels are stable, depth of occurrence is 4-7 m, replenishment is limited, and outflow is formed by evapotranspiration.

It has also been established that a significant part of the underground flow is lost to evaporation in swampy and saline areas, reducing the total outflow. This confirms that increasing irrigation water withdrawals can improve the reclamation status of adjacent areas. The primary source of groundwater is the filtration of surface runoff in the foothill zone, enhanced by irrigation above the discharge zone [10-11]. According to data from the regional water management authority, water withdrawal for irrigation within the deposit during the growing season averages 39.10 m^3/sec, i.e., the average annual water withdrawal for irrigation was 19.55 m^3/sec. At the same time, irrigation water withdrawal does not depend on the year's water content.

Thus, out of the total amount of 31.25 m^3/sec of total surface runoff losses at 50% reliability and 23.13 m^3/sec of losses at 85% reliability, 19.55 m^3/sec is lost on average in canals and irrigation fields. Water losses directly in river beds due to filtration and evapotranspiration amount to 11.70 m^3/sec at 50% reliability and 3.58 m^3/sec at 85% reliability, respectively, in Table 2.

Table 2. Surface runoff losses

Naming of watercourses	Cost of posts m^3/sec				Loss of surface runoff, m^3/sec	
	Upper gate		Lower gate		Reliability 50%	Reliability 85%
	Reliability 50%	Reliability 85%	Reliability 50%	Reliability 85%		
Tentek River	46.94	34.74	24.39	18.05	22.55	16.69
The river of Zhamanty	5.39	3.99	0	0	5.39	3.99
Total expenses of small rivers and streams	3.31	2.45	0	0	3.31	2.45
Total losses of river flow	–	–	–	–	31.25	23.13

By analogy with other deposits of a similar type (Aksu, Lugovskoye, Merken, Khorgos, etc.), we assume that 80% of the total channel losses are directly replenished to groundwater and 20% are lost to evaporation and soil wetting. Consequently, the amount of water supplied by filtering riverbeds across the entire field will be 9.36 m^3/sec at 50% availability and 2.66 m^3/sec at 85% availability. The flow losses of the Tentech River must be reduced by the flow of the Aksopa MK, which flows from the left bank of the river beyond the boundaries of the field.

According to data from the regional water management agency, the efficiency coefficient of the primary and distribution channels is 76%. The amount of groundwater replenishment due to losses in irrigation fields within the cones of depression varies from 60 to 80% of the water supply to irrigation fields, with an average of 65% (by analogy with the Khorgos field). Consequently, the amount of groundwater recharged from main channels will be 4.70 m^3/sec, and from irrigation fields 9.65 m^3/sec, for a total of 14.35 m^3/sec. Thus, within the cones of groundwater discharge at the Alakol deposit, 23.71 m^3/sec of the total 31.25 m^3/sec of surface runoff losses at 50% reliability and 17.71 m^3/sec out of a total of 23.13 m^3/sec of losses at 85% reliability (Figure 3).

Precipitation infiltration during the winter-spring period occurs in March-April, and during the summer period, it evaporates completely. The replenishment of groundwater through atmospheric precipitation infiltration was determined only in the area of groundwater flow formation, which creates a certain margin of safety in the calculations, since atmospheric precipitation infiltration also occurs in the area of groundwater transit and discharge.

In the area where underground runoff from the Alakol deposit forms, the aeration zone consists of boulders and gravel, with sandy fill and almost no loamy cover. The average adequate precipitation, according to data from the Usharal weather station, was 125.4 mm in a typical year and 89 mm in a dry year, with 85% reliability.

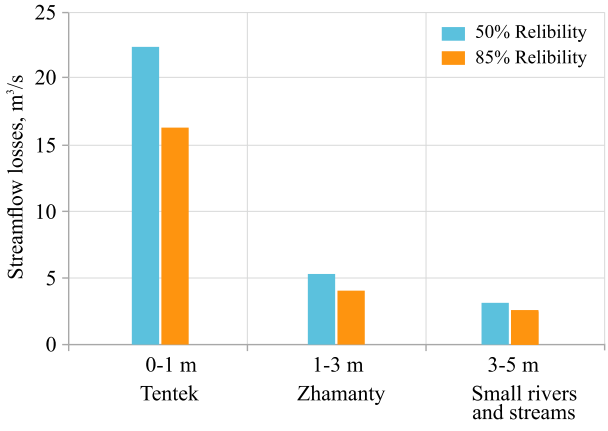

Figure 3. Losses of surface runoff by the watercourse

The area of the foothill plain, which is almost entirely devoid of fine-grained cover deposits, amounts to 815 km^2. The results of the calculations of groundwater recharge due to atmospheric precipitation infiltration are presented in Table 3. Figures 4-6 illustrate the distribution of groundwater recharge parameters by groundwater depth interval, showing variations in total recharge, effective precipitation, and the infiltration coefficient.

Table 3. Groundwater recharge due to atmospheric precipitation infiltration

Groundwater depth intervals	Area, km^2	Effective precipitation, mm	Infiltration coefficient	Infiltration nutrition	
				mm	mln. m^3
0-1	442	125.4	0.60	75.24	33.15
1-3	878	125.4	0.25	43.9	38.54
3-5	60	125.4	0.10	12.54	0.72
Total	–	–	–	131.7	72.4

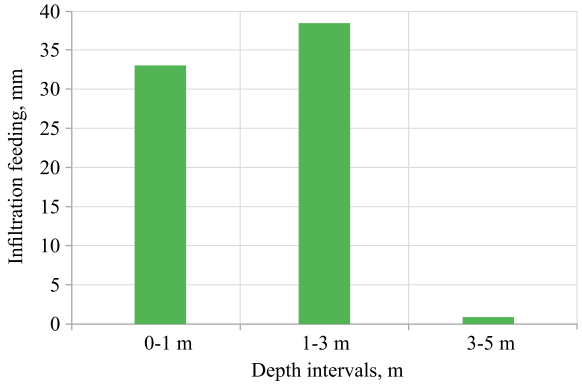

Figure 4. Infiltration of groundwater at different depths

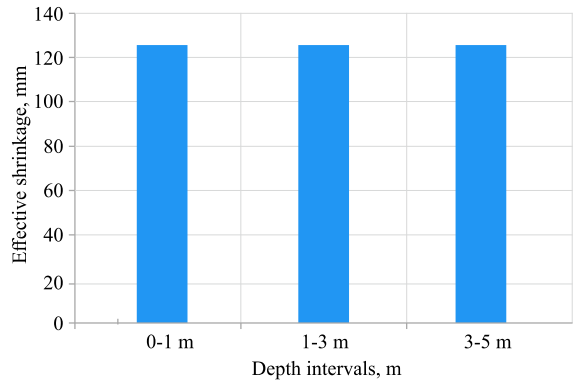

Figure 5. Effective precipitation by groundwater depth interval

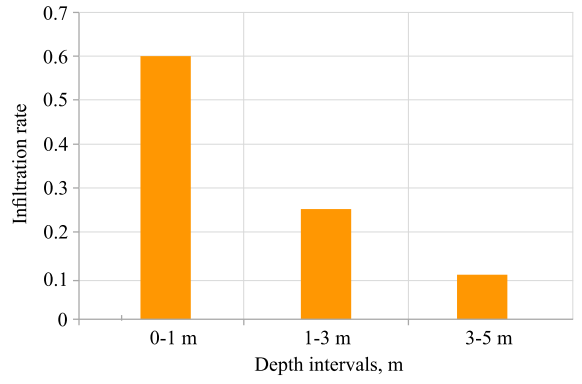

Figure 6. Infiltration coefficient by groundwater depth interval

Adequate precipitation remains constant across all groundwater depth intervals (125.4 mm), whereas the infiltration coefficient decreases with depth, from 0.60 to 0.10.

Infiltration of atmospheric precipitation within this zone is 131.7 mm per year or 30.644 million m^3 (0.97 m^3/sec) in a normal year in terms of water content, and 26.7 mm or 21.761 million m^3 (0.69 m^3/sec) in a dry year with 85% reliability. It's impossible to figure out how much underground water flows from the mountains into the foothill plains. It was assumed that there is no deep underground flow from the mountainous border to the deposit under consideration. This leads to a slight underestimation of natural resources and creates a certain reserve of "engineering" strength.

The expenditure items in the groundwater balance under undisturbed conditions include evaporation (evapotranspiration) and groundwater discharge into rivers and springs. Groundwater evaporation occurs in areas where it lies close to the surface, mainly located below the zone of groundwater formation. Table 4 below shows the results of determining evaporation from the groundwater surface [12].

Table 4. Evaporation from the surface of groundwater

Groundwater depth ranges	Area, km^2	Average evaporation of groundwater, mm.	Total evaporation of groundwater	
			mln. m^3	m^3/sec
0-1	442	800	353.6	11.22
1-3	878	300	263.4	8.35
3-5	60	50	3	0.1
Total	–	–	620.0	19.67

Figure 7 presents total groundwater evaporation and average evaporation by groundwater depth interval. The most significant moisture losses occur where groundwater lies within 1 m of the surface. Evaporation decreases significantly with increasing depth, indicating a strong dependence of evaporation intensity on groundwater level. Despite lower average evaporation in the 1-3 m range, the large area compensates, contributing significantly to the total evaporation volume. At depths greater than 3 m, moisture loss through evaporation is almost negligible. The deeper the water, the less evaporation, as the availability of water for evaporation decreases. The highest average annual evaporation occurs in waters at 0-1 m depth. The closer the water is to the surface, the easier it evaporates. Although evaporation is lower in the 1-3 m interval, due to the large area, it produces almost the same amount of evaporation as the 0-1 m interval. m^3/sec is the conversion of total evaporation into flow over time.

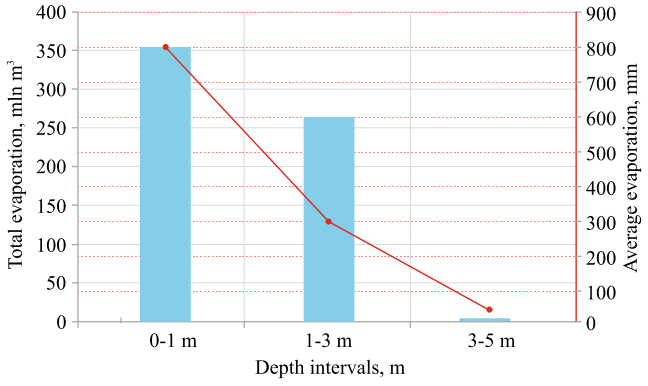

Figure 7. Evaporation from the surface of groundwater at different depths

Total evaporation is 620 million m^3/year or 19.67 m^3/sec and also includes evaporation of atmospheric precipitation that has filtered down to the water table in the shallow groundwater zone [13-14].

Discharge of groundwater into springs, Karasu rivers, and surface water bodies. The spring zone can be traced along the periphery of the Tenteq River's alluvial fan, roughly along a line passing through the settlements of Usharal, Zhagatal, Obukhovka, Chistopolskoye, Socialdy, and Izendy. Merging, the springs form small Karasu rivers, on which temporary hydrometric stations have been installed to record spring discharge. Hypsometrically below the line of springs is an area of surface discharge, which occupies the entire northeastern half of the deposit and is bounded by the lakes Alakol, Uyal, Kashkarkol, and Sasykol. This zone consists of extensive swamps, the most significant of which is located in the form of a strip 3 to 8 km wide and 26 km long, directly adjacent to the spring wedge line.

Groundwater depth varies across the study area. Regular hydrometric measurements of discharge were carried out every ten days using a hydrometric propeller device. The average annual value of the measured spring flow is 12.0 m^3/s. The total length of the spring line is approximately 60 km, corresponding to an average discharge rate of 0.20 m^3/s per kilometer of groundwater emerging as springs and feeding the Karasu River. In the area of the Zhaypak spring, the zone of groundwater discharge approaches the shoreline of Lake Alakol and is further controlled by the coastal line up to the Zhamanty River. These observations indicate a strong hydraulic connection between the aquifer system and surface water bodies, highlighting the importance of springs as a major outlet of the regional groundwater flow. The shore of Lake Alakol in this area is steep, rising 3-5 meters or more. At the base of the cliff, composed of large pebbles, groundwater seepage can be observed everywhere, but it is not possible to take this discharge into account. The erosion zone apparently extends below the lake's waterline, as the slope below it is also composed of large pebbles. Assuming that the intensity of wedging in this zone remains the same, approximately 4.0 m^3/sec of groundwater is discharged along the 20 km of coastline from the Zhaypak spring to the Zhamanty River. Thus, the total spring discharge is 16 m^3/sec. The total amount of groundwater discharge at the deposit will be 18.06 m^3/sec. The groundwater balance of the deposit is presented in Table 5.

Table 5. Groundwater balance of the Alakol groundwater deposit

Name of income and expense items	Groundwater flow rate	
	Reliability 50%	Reliability 85%
Losses of river runoff for filtration	11.08 9560.83	3.58 247.10
Filtration of water from the main channels	4.54 392.26	4.54 392.26
Filtration losses in irrigation fields	9.36 9560.83	9.36 9560.83
Infiltration of atmospheric precipitation	19.67 83.81	0.69 59.62
Total revenue items	44.65 2093.47	17.45 1507.68
Discharge of groundwater into springs, rivers, "Karasu" and surface reservoirs	18.06 1560.4	12.91 1115.42
Evaporation and transpiration	19.67 660.96	8.34 720.58
Total expenditure items	37.73 2222.7	21.25 1836
Balance discrepancy	6.92 127.87	3.80 328.32

Under the 50% reliability scenario, the main components of groundwater inflow are atmospheric precipitation infiltration (19.67 m^3/s) and river runoff losses (11.08 m^3/s). The principal discharge components are evaporation and groundwater discharge into surface water bodies. The calculated balance discrepancy amounts to 6.92 m^3/s (approximately 15.5%), reflecting the difference between total inflow and discharge and likely due to accounting uncertainties or unconsidered subsurface flows.

Under the 85% reliability (dry-year) scenario, precipitation infiltration decreases significantly to 0.69 m^3/s. As a result, the total inflow is reduced by nearly 2.5 times. Although total discharge also decreases, a balance discrepancy of 3.80 m^3/s remains. Thus, under conditions of average water availability (50%), recharge from precipitation plays a substantial role, whereas under dry conditions (85%), the groundwater balance is considerably reduced but remains positive.

The imbalance requires further analysis (possible losses due to deep drainage or underestimation of individual items). The expenditure items for the 85% security balance are approximately determined based on the dependence of total groundwater discharge through springs on aquifer recharge. The imbalance in the balance of 6.92 m^3/sec for normal conditions and 3.80 m^3/sec at 85% security is 6.1% and 21.5%, which is quite acceptable, given the degree of accuracy in determining the expenditure items of the balance [15].

To increase the reliability and accuracy of calculating the total groundwater discharge from springs with 85% confidence, a series of spring discharge observations was conducted over three years (1976-1978) in the area of intensive discharge. The average total discharge was 12 m^3/s. Analyzing data on surface runoff and precipitation in this area, the spring discharge period corresponds to a water content range of 55%-65%. The value of 12 m^3/s was taken as the average annual discharge in the area of intensive spring discharge.

The results determined the structure of aquifers and provided data on water abundance, permeability, and long-term stability of reserves.

Application of the regime classification scheme according to D.M. Kats, taking into account local conditions. Separate consideration of recharge and discharge zones based on the results revealed the characteristics of the interaction between natural and anthropogenic factors. It was established that the groundwater regime is seasonal, with elevated levels in spring and summer.

To assess the recharge and water balance of groundwater at the Alakol deposit, the following balance equation was used:

$$q + \xi_i + Q_1 = E + q + Q_2, \quad (2)$$

The calculations were based on data from the Hydrometeorological Service and hydrometric observations on the Tentek River (Tunkuruz station) over a 44-year period. It was established that the main recharge of aquifers is provided by infiltration of atmospheric precipitation and filtration of river water, with evaporation and drainage losses accounting for a significant part of the water balance.

Evaporation from the groundwater level was estimated based on lysimeter data from the Aksu deposit and graphs showing the dependence of evaporation on water depth and vegetation cover. It was established that at depths <2 m, evaporation reaches maximum values similar to those in Aksu and significantly reduces available groundwater resources.

The quality of groundwater was determined through a comprehensive analysis of samples collected during pumping, including chemical, spectral, radiological, and bacteriological testing. Compliance was assessed in accordance with GOST standards 18963-73, 4979-49, 2762-57, 2874-73, and others. The results showed that the water mostly meets the requirements for irrigation, with mineralization <2.5 g/l, but for drinking water supply, additional purification is needed to meet specific indicators.

The engineering-geological assessment of the area around the water intakes included an analysis of relief slopes, flooding zones, erosion processes, and seismic activity. Overall, the area is stable, but it is advisable to restrict construction near slopes and to provide erosion control measures.

Hydrogeological zoning of the deposit was performed based on stratigraphic and genetic analyses of sections, identifying the structure and interrelationships among the aquifers. It was established that groundwater is confined to a single aquifer complex formed by alluvial-proluvial and alluvial-lacustrine deposits of the Lower and Middle Quaternary age, with a pronounced hydraulic connection between the layers.

The capacity of water supply points in the Alakol basin ranges from 2.5 to 50 dm^3/s. The flow rates of self-spilling wells reach 50 dm^3/s. The waters are mainly sodium and calcium bicarbonate, with mineralization not exceeding 0.7 g/dm^3. Sediments of stratigraphic-genetic complexes associated with accumulative hummocky-ridge and flat concave plains are linked to groundwater with a level depth (depending on the relief) ranging from 0 to 20 m or more. The mineralization and chemical composition of groundwater are highly diverse. As groundwater flows toward the center of the depressions, water salinity increases, ranging from 1 to 10 g/dm^3. Accordingly, the composition changes from calcium bicarbonate to magnesium-sodium sulfate-chloride.

Groundwater, mostly occurring at shallow depths (1-5m), is associated with alluvial deposits. In floodplains and river deltas, the groundwater level depth is no more than 1 m. The thickness of alluvial aquifers does not exceed 30 m. The water content of rocks varies widely. Flow rates of tenths of a liter per second prevail, and only in the upper reaches of rivers, where the water-bearing rocks are pebbles, do well flow rates reach 3 dm^3/s. The mineralization of the waters reaches 5-10 g/dm^3 and, in some cases, even 50 g/dm^3. The composition of the water is sulfate and sodium chloride [16, 17].

The natural regime of groundwater is characterized by smooth, shallow-amplitude (0.5-1.0 m) fluctuations in levels throughout the year, with weakly expressed spring maxima and summer minima. The central autumn-winter maximum is due to the filtration flow of irrigation and wastewater from irrigated areas. The level rise is 1.8-2.2 m, and in areas of rice crop rotations, it reaches 5 m. An irrigation-type groundwater regime has developed over a large area.

Modern geological processes and phenomena in the region are mainly associated with human engineering and economic activities, particularly land reclamation and construction. Until the 1960s, the development of DGPs was episodic. The erosive activity of water flows was observed only during spring floods and heavy rains, leading to bank erosion and collapse. Deflation was evident in the eolian processing of alluvial-lacustrine sediments, resulting in the formation of blow basins, dunes, wind ripples, and other microrelief forms [18, 19]. Salinization and waterlogging occurred through the extensive development of salt marshes, sores, and puffs in areas with shallow groundwater levels.

Abrasion was intensely observed on the southern and eastern shores of Lake Alakol. The southern shore of the lake (near the village of Koktuma) has moved more than 200 m over 20 years. As a result of the washout and collapse of the coastal ledge, part of the village was destroyed. The shoreline of the lake has advanced very close to the railway track. Abrasion is activated by frequent hurricane winds and an increase in the lake's surface area. According to measurements from 1862 and 1931, the lake's length and width increased by 5 km. Even more intensive growth of the water area was established by the 1951 measurements. Over 20 years, the lake's length increased by 15 km, its width by 5 km, and its depth significantly as well [20].

4. Conclusions

The study established the hydrogeological structure of the Alakol groundwater deposit. It clarified the main characteristics of its aquifer system, including water abundance, permeability, and the long-term stability of groundwater reserves. The results confirmed the existence of a hydraulically connected single aquifer complex formed by Lower and Middle Quaternary alluvial-proluvial and alluvial-lacustrine deposits.

The groundwater regime was found to be predominantly seasonal, with higher groundwater levels during spring and summer. The primary sources of aquifer recharge are infiltration of atmospheric precipitation and filtration of river water, whereas evaporation and drainage constitute major components of groundwater discharge. Evaporation from the groundwater table is especially significant when groundwater occurs at depths of less than 2 m, substantially reducing the volume of available water resources.

The study also demonstrated the critical role of both natural and anthropogenic factors in shaping the groundwater regime and balance. In particular, irrigation-related infiltration contributes noticeably to groundwater recharge, while shallow groundwater occurrence in lowland and swampy areas enhances evaporation losses.

In terms of water-use potential, groundwater in the Alakol deposit generally meets irrigation requirements, with mineralization in most cases remaining below 2.5 g/L. At the same time, its use for drinking water supply may require additional treatment depending on specific chemical indicators. Overall, the obtained results confirm the practical significance of the Alakol groundwater deposit as a promising source of water supply for irrigation development in the region, provided that groundwater abstraction is managed with consideration of recharge conditions, evaporation losses, and local hydrogeological constraints.

Author contributions

Conceptualization: MMA, MRZ; Data curation: MMA, EMK; Formal analysis: MRZ, AZI, EMK; Funding acquisition: MMA, MRZ; Investigation: MMA, EMK; Methodology: MMA, NT; Project administration: MMA, MRZ; Resources: NT, EMK; Software: AZI, EMK; Supervision: MRZ, AZI; Validation: MMA, AZI; Visualization: NT, EMK; Writing – original draft: MMA, MRZ; Writing – review & editing: NT, EMK. All authors have read and agreed to the published version of the manuscript.

Funding

This research received no external funding.

Acknowledgements

The authors express their sincere gratitude to the editor and anonymous reviewers for their constructive comments and valuable suggestions, which have significantly improved the quality of this manuscript.

Conflicts of interest

The authors declare no conflict of interest.

Data availability statement

The original contributions presented in this study are included in the article. Further inquiries can be directed to the corresponding author.

References

[1] Sanatbekov, M.E., Zholtaev, G., Tileuberdi, N., Auelkhan, E.S. & Imansakipova, Z.B. (2024). Study of geodynamic and hydrogeological criteria for assessing the hydrocarbon potential of the Alakol depression. *Naukovyi Visnyk Natsionalnoho Hirnchoho Universytetu*, *(4),* 5-10. https://doi.org/10.33271/nvngu/2024-4/005

[2] Alzhigitova, M.M., Zapparov, M.R., & Mirlas, V.M. (2021). Impact of anthropogenic activity on the condition of Lake Alakol. *Engineering Journal of Satbayev University*, *143*(2), 44-51. https://doi.org/10.51301/vest.su.2021.i2.06

[3] Alzhigitova, M.M., & Zapparov, M.R. (2020). Engineering and hydrogeological features of the Alakol depression. *Vestnik Kaznitu, 142(6),* 35-42.

[4] Baibatsha, A.B., & Kurkina, L.A. (2003). General Engineering Geology. Almaty, *Scientific and Publishing Center «Gylym».*

[5] Bariinov, A.V. (2003). Emergency Situations of Natural Character and Protection from Them. *Moscow: Publishing House «Vlados-Press».*

[6] Tarikhazer, S. A., Karimova, E. J., & Kuchinskaya, I. Y. (2022). Quantitative assessment of mudflow risk in the Greater Caucasus of Azerbaijan (on the example of the northeastern slope). *Journal of Geology, Geography and Geoecology, 31(4),* 722-735. https://doi.org/10.15421/112268

[7] Valeyev A., Karatayev M., Abitbayeva A., Uxukbayeva S., Bektursynova A., Sharapkhanova Z. (2019). Monitoring Coastline Dynamics of Alakol Lake in Kazakhstan Using Remote Sensing Data. *Geosciences*, *9*(9), 404. https://doi.org/10.3390/geosciences9090404

[8] Zaripov, A.S., & Luchnikov, A.I. (2021). Investigation of the dynamics of bank failure of the Kama and Votkinskoye reservoirs as a result of abrasion using aerial photography materials. *Georisk, 15(1),* 58-66. https://doi.org/10.25296/1997-8669-2021-15-1-58-66

[9] Khalykov, E.E., Ly, Y.F., Abitbaeva, A.D., Togys, M.M., & Valeev, A.G. (2021). Determination of the dynamics of reworking the shore escarpment of Lake Alakol using a laser scanner. *Geography and Water Resources, (4),* 23-32.

[10] Valeev, A.G., Akiyanova, F.J. & Sagintaev, J. (2020). Modern relief-forming processes of the shore zone of Lake Alakol. *Hydrometeorology and ecology, 2(97),* 125-145.

[11] Chaklikov6 A.Y., Korobkin6 V.V., Ismailov6 A.A., Buslov, M.M., & Tulemissova6 Z.S. (2024). Specifics of the Geological Structure of the Alakol Basin and the Choice of Drilling Well Design. *Kazakhstan Journal for Oil & Gas Industry, 6(1),* 18-34. https://doi.org/10.54859/kjogi108695

[12] Zhiyembayeva, J.A., Zhanakova, R.K., Sarybayev, M.A., Nurtay, G. & Yelzhanov, E.A. (2024). Investigation of hazardous geologic processes at the Kaskelen-Talgar polygon by geodetic methods. *Bulletin of Kazgasa, 1(91),* 108-121

[13] Kozhnazarov, A.D. (2004). Engineering Geodynamics. *Almaty: KazNTU*

[14] Maltseva, K.A., & Maltsev, A.V. (2023). Efficiency of application of geophysical methods of soil investigation of landslide massifs. *In XLIX Samara Regional Student Scientific Conference, 1(S),* 155-156. https://journals.eco-vector.com/osnk-sr2023/article/view/425810

[15] Gulkayyr, T. & Rakhmedinov, E.E. (2023). Large landslides in active structures of southwestern Tien Shan (Batken oblast). *Bulletin of the Institute of Seismology of the National Academy of Sciences of the Kyrgyz Republic, 1,* 21

[16] Zakirova, D.A., Satybaev, A.D. & Satybaldiev, B.S. (2024). Analysis of Causes of the origin of the sinkhole movement process (on the example of Nookat district of Osh oblast). *Bulletin of Science and Practice, 10(9),* 80-89,

[17] Semyachkov, A.I., Pochechun, V.A., & Semyachkov, K.A. (2023). Hydrogeoecological conditions of technogenic groundwater in waste disposal sites. *Notes of the Mining Institute,* (260)*,* 168-179.

[18] Bielova, N., Mykytyn, T. & Dolynko, N. (2023). Monitoring of Modern Exogenous Processes in Precarpathia. *In 17th International Conference Monitoring of Geological Processes and Ecological Condition of the Environment, 1,* 1-5. https://doi.org/10.3997/2214-4609.2023520165

[19] Hablovskyi, B., Hablovska, N., Shtohryn, L., Kasiyanchuk, D. & Kononenko, M. (2023). The Long-Term Prediction of Landslide Processes within the Precarpathian Depression of the Cernivtsi Region of Ukraine. *Journal of Ecological Engineering, 24(7),* 254-262. http://dx.doi.org/10.12911/22998993/164753

[20] Cascini, L., Scoppettuolo, M. R. & Babilio, E. (2022). Forecasting the landslide evolution: from theory to practice. *Landslides, 19(12),* 2839-2851. https://doi.org/10.1007/s10346-022-01934-3

Курорт инфрақұрылымының қажеттіліктері үшін Алакөл жерасты суы кен орнының гидрогеологиялық сипаттамасы

М.М. Альжигитова*, Е.М. Кульдеева, А.Ж. Исмагулова, М.Р. Заппаров, Н. Тілеуберді

Satbayev University, Алматы, Қазақстан

**Корреспонденция үшін автор: m.alzhigitova@satbayev.university*

Аңдатпа. Мақалада Қазақстанның оңтүстік-шығысындағы Алакөл ойысында орналасқан Алакөл жер асты су кен орнының геологиялық және гидрогеологиялық ерекшеліктеріне кешенді зерттеу жүргізілген. Аталған жер асты су көзі Алакөл көлінің оңтүстік жағалауында қарқынды дамып келе жатқан курорттық инфрақұрылымды сумен қамтамасыз етудің негізгі көздерінің бірі болып табылады және аймақтың әлеуметтік-экономикалық дамуы үшін маңызды рөл атқарады. Зерттеу барысында аумақтың геоморфологиялық ерекшеліктері, су қабаттарының литологиялық құрамы

мен қалыңдығы, олардың жату жағдайлары және жер асты суларының түзілуі мен динамикасына әсер ететін факторлар талданды.Жер асты суларының режимі олардың қоректену және ағызылу аймақтары бойынша қарастырылып, сүзгілеу ағынының негізгі бағыттары мен жер асты және жер үсті суларының гидродинамикалық байланысы анықталды. Ерекше назар курорттық аймақтағы құрылыстардың тұрақтылығына әсер ететін инженерлік-геологиялық жағдайларды бағалауға және антропогендік факторлардың әсерінен су балансының өзгеруіне аударылды. Жер асты суларының химиялық құрамы мен физика-химиялық қасиеттеріне талдау жүргізіліп, олардың ауыз су және ауыл шаруашылығы қажеттіліктеріне жарамдылығы анықталды. Нәтижелер бойынша, Алакөл кен орнының суы санитарлық-гигиеналық нормаларға сай келеді, минералдану деңгейі орташа және оны топыраққа зиян келтірмей суару мақсатында пайдалануға болады. Зерттеуде қолданыстағы су тарту құрылыстарының конфигурациясы, жер асты суының өндіру көлемі қарастырылған. Сондай-ақ, жер асты суларын ұтымды және тұрақты пайдалану мәселелеріне, су ресурстарын қорғау шараларын әзірлеуге ерекше назар аударылған. Алынған нәтижелер Алакөл көлінің оңтүстік жағалауының курорттық және аграрлық инфрақұрылымын одан әрі дамытуда пайдаланылуы мүмкін.

Негізгі сөздер: *жер асты сулары; жер асты суларының режимі; сулы қабаттар; жер асты суларының балансы; су алу; кен орны.*

Гидрогеологическая характеристика Алакольского месторождения подземных вод для нужд курортной инфраструктуры

М.М. Альжигитова*, Е.М. Кульдеева, А.Ж. Исмагулова, М.Р. Заппаров, Н. Тілеуберді

Satbayev University, Алматы, Казахстан

**Автор для корреспонденции: m.alzhigitova@satbayev.university*

Аннотация. В статье представлено комплексное исследование геологических и гидрогеологических характеристик подземного водозабора Алаколь, расположенного в пределах Алакольской впадины на юго-востоке Казахстана. Данное месторождение подземных вод служит одним из основных источников водоснабжения быстро развивающейся курортной инфраструктуры на южном берегу озера Алаколь и имеет важное значение для социально-экономического развития региона. В работе проанализированы геоморфологические особенности территории, литологический состав и мощность водоносных горизонтов, условия их залегания, а также факторы, влияющие на формирование и динамику подземных вод. Рассмотрен режим подземных вод в зонах питания и разгрузки, определены основные направления фильтрационного потока и особенности гидродинамической связи между подземными и поверхностными водами. Особое внимание уделено оценке инженерно-геологических условий, влияющих на устойчивость сооружений курортной зоны, а также изменениям водного баланса под воздействием антропогенных факторов. Проведён анализ химического состава и физико-химических свойств подземных вод с целью определения их пригодности для питьевого водоснабжения и сельскохозяйственного использования. Результаты показали, что вода Алакольского месторождения в целом соответствует санитарно-гигиеническим нормам для питьевых целей, имеет умеренную минерализацию и может применяться для орошения сельскохозяйственных угодий без ущерба для почв. Особое внимание уделено вопросам рационального и устойчивого использования подземных вод, а также разработке перспективных мер по охране водных ресурсов. Полученные результаты могут быть использованы при планировании дальнейшего развития курортной и аграрной инфраструктуры южного побережья озера Алаколь.

Ключевые слова: *подземные воды; режим подземных вод; водоносные горизонты; баланс подземных вод; водозабор; месторождение.*

Publisher's note

All claims expressed in this manuscript are solely those of the authors and do not necessarily represent those of their affiliated organizations, or those of the publisher, the editors and the reviewers.

SATBAYEV UNIVERSITY

Engineering Journal of Satbayev University

Volume 148 (2026), Issue 1, 38-47

https://doi.org/10.51301/ejsu.2026.i1.05

Numerical modelling of critical conditions for the onset of a limit state in the rock mass surrounding unfilled underground voids in iron ore deposits

M. Petlovanyi*, K. Sai

Dnipro University of Technology, Dnipro, Ukraine

**Corresponding author: petlovanyi.m.v@nmu.one*

Abstract. The purpose of this study is to develop an approach for the quantitative assessment and prediction of rock mass condition surrounding unfilled underground voids, with a focus on a limit state associated with potential instability and ground surface collapse, using numerical modelling techniques. The investigation was carried out using finite element modelling of the stress-strain state of a stratified rock mass in the RS2 software package. To adequately reproduce the mechanical behaviour of fractured rocks of the Kryvyi Rih Iron Ore Basin, the stratified geological structure of the rock mass was incorporated into the model. The nonlinear Hoek-Brown failure criterion was applied, accounting for the Geological Strength Index (GSI). The existence of a transitional (near-failure) geomechanical state of the rock mass surrounding unfilled underground voids has been established. This state develops between stable and unstable conditions and is characterised by mechanical interaction between the void and the ground surface. A stable logarithmic relationship between the lower and upper bounds of the critical ratio H/L_c and the void depth has been identified, quantitatively reflecting the increase in rock mass resistance as the depth increases toward the limit state. An exponential relationship between the width of the ground surface subsidence trough and the parameter H/Lc has been identified, enabling the prediction of the extent of the potential collapse zone. An exponential relationship between the required strength of the cemented paste backfill and the H/L_c ratio has been established, defining the minimum bearing capacity of the backfill under near-failure conditions. For the first time, the existence of a distinct near-failure geomechanical regime of the rock mass surrounding unfilled underground voids has been quantitatively substantiated as an independent state preceding progressive ground surface collapse. The obtained relationships enable predicting the geomechanical condition of the rock mass above unfilled voids, determining the range of their critical geometric parameters, and timely identifying voids in a near-failure state. The developed approach can be applied in engineering practice to justify the parameters of cemented paste backfill from the surface to prevent sudden ground surface collapse.

Keywords: *numerical modelling; underground void; stratified heterogeneous rock mass; Hoek-Brown failure criterion; near-failure state; ground surface collapse; cemented paste backfill.*

Received: 3 November 2025
Accepted: 22 February 2026
Available online: 28 February 2026

1. Introduction

Ukraine possesses strategically important proven iron ore reserves. More than 45% of these reserves (8.6 billion t) are located in Dnipropetrovsk Oblast, with the greater part concentrated within the large Kryvyi Rih Iron Ore Basin (Kryvbas). The mining and processing of iron ores form the backbone of Ukraine's metallurgical industry. In contrast, the produced iron ore feedstock and concentrate are supplied to both the domestic market and export. A substantial share of the extracted ore and beneficiation products is exported, generating significant foreign-currency revenues for the state budget and supporting the country's external economic balance; in 2021, these revenues amounted to USD 3.91 billion. At present, approximately 70% of Ukraine's total iron ore production is mined annually in the Kryvyi Rih Iron Ore Basin, with 90% extracted by open-pit mining and 10% by underground mining [1-3].

Over more than a century of intensive iron ore mining in the Kryvyi Rih Basin, the subsurface and the ground surface have undergone large-scale anthropogenic transformation. In the rock mass, a complex set of geomechanical processes has developed, including the formation of extensive zones of strata movement and discontinuities, the accumulation of unfilled underground voids, and a progressive deterioration of rock mass stability. At the surface, gradual soil depletion and degradation, destruction of natural ecosystems, and large-scale stockpiling of mining and beneficiation wastes are observed, accompanied by contamination of groundwater, surface waters, and the atmosphere [4-8]. Under these conditions, the design and implementation of environmentally oriented mining technologies become important tasks [9-12].

The most pressing issue remains elevated anthropogenic and geomechanical hazards, manifested by recurrent sudden rockfall events and slope failures, the formation of collapse

petlovanyi.m.v@nmu.one; sai.k.s@nmu.one
Engineering Journal of Satbayev University. eISSN 2959-2348. Published by Satbayev University

zones and subsidence troughs, and the resulting threats to infrastructure, the environment, and public safety. Owing to the long-term operation of deposits in the Kryvyi Rih Iron Ore Basin, many of which were developed by underground mining without adequate closure of the mined-out space, a considerable number of blind and isolated ore bodies and lenses have been extracted, and the resulting voids pose a significant geomechanical and anthropogenic risk to the region.

At present, approaches to assessing the stability of a rock mass containing voids created by the extraction of ore deposits, as prescribed in existing scientific and methodological documents [13, 14], are generally based on determining the conditions for the formation of primary sinkholes. These approaches allow only the identification of the transition of the system into an unstable state, with a likelihood of deformation reaching the ground surface in the form of collapse funnels, and effectively reduce the geomechanical state of the rock mass to two categories: stable and unstable.

However, as practical experience in the Kryvbas demonstrates, sudden ground surface collapses are periodically recorded even after the extraction of reserves from blind, isolated ore bodies has been completed [15, 16]. The occurrence of such collapses indicates the presence of an intermediate state, namely, a near-failure state of the rock mass surrounding unfilled underground voids, in which the rock mass is weakened but still retains residual stability and is capable of an abrupt transition to an unstable regime. These formed and unfilled underground voids may suddenly destabilise, leading to sinkholes or the development of subsidence troughs at the ground surface. These sudden events are particularly hazardous in urbanised areas, where industrial or civil infrastructure, as well as natural assets, may be located above the voids. Therefore, there is a need for geomechanical forecasting that enables the identification of underground voids in a near-failure state and supports scientifically grounded decisions on their timely stabilisation.

The importance of timely identification of formed voids that are in a near-failure state lies in the opportunity to implement preventive measures and thereby avert ground surface collapse. A practical mitigation measure is the placement of cemented paste backfill into unfilled voids from the ground surface through a drilled backfilling borehole [4, 17-19], as such voids are typically located at a relatively shallow depth. The paste backfill mixture is prepared from fine-grained iron ore beneficiation tailings (65-80%) recovered from dewatered tailings storage facilities, locally available binders (3-10%) such as cement, ground slag, and fly ash and 15-30% water [20]. These components are mixed at a surface backfilling plant and then delivered by pressurized pipeline transport to technogenic voids, in this case, unfilled underground voids left after the extraction of blind, separated, and isolated ore bodies.

Identification of a near-failure rock mass state surrounding unfilled voids is advisable using finite-element numerical modelling in modern geomechanical software packages. Studies by Kryvyi Rih researchers have made a significant contribution to understanding the deformation patterns of the rock mass during ore extraction [21-23]. However, most investigations were local in scope, focused on stoping chambers, and were performed mainly under the assumption of linear-elastic rock mass behaviour. Given the hard-rock and fractured nature of the Kryvbas formations, the application of generalised nonlinear strength criteria, particularly the Hoek-Brown failure criterion, is promising. This approach provides a more accurate representation of the influence of rock mass structural disturbance and improves the prediction of strata movement zones and potential collapses.

2. Materials and methods

At present, the following research approaches can be distinguished for solving geomechanical problems in mining engineering: analytical methods [24, 25], physical modelling [26-28] and numerical modelling [29-32]. The most widespread approach is finite element numerical modelling due to its ability to realistically reproduce phenomena and processes, provide reliable results, and reduce labour intensity.

One of the most suitable strength criteria for hard rock and fractured rock masses is the empirical Hoek-Brown failure criterion, which accounts for rock mass quality through the Geological Strength Index (GSI), jointing, and the degree of disturbance. E. Hoek and E. T. Brown developed the Hoek-Brown criterion in 1980 [33]. It was proposed as an empirical alternative to the Mohr-Coulomb criterion to describe the strength of intact rock and rock masses exhibiting nonlinear behaviour, while accounting for fracturing, structure, and disturbance.

Today, the Hoek-Brown failure criterion is widely used for modelling rock mass behaviour in geomechanical analyses. Its direct implementation is available in major specialised software packages, including FLAC3D, RS2, RS3, and Slide2/3 (Rocscience), as well as UDEC and 3DEC (Itasca), where it is provided as a core function with options to account for strength degradation and staged excavation.

Within this study, the numerical calculations were performed using the RS2 software package, which provides a range of strength criteria, including the Hoek-Brown criterion [34]. A key parameter of the Hoek-Brown criterion is the Geological Strength Index (GSI), which provides an integrated assessment of rock mass structural disturbance and accounts for scale effects.

To model the stability of rocks surrounding unfilled voids in the Kryvbas, the GSI values for different lithologies were estimated as GSI = 3045 based on an analysis of the rock mass structure and the condition of discontinuity surfaces observed in exposures within collapse zones, using photo documentation and supplementary data. This range is justified because it reflects a combined weakening effect relative to the natural rock mass state, for which GSI is typically assessed as 60-70 increased weathering due to the shallow depth of the voids, and additional anthropogenic damage to the rock mass caused by historical blasting during mining operations.

For the study, a geomechanical model was developed that includes unconsolidated overburden deposits, a stratified hard-rock mass, and an unfilled underground void left after the extraction of a blind, isolated ore body, according to the averaged stratigraphic section of the central (Saksahan) iron ore district of the Kryvbas. The model domain was set to 600 m in the vertical direction and 800 m in the horizontal direction.

The unfilled void considered in this work is located within the V iron-bearing horizon, which is characterised by the highest ore-bearing coefficient and the greatest concentration of ore bodies in the Saksahan district of the Kryvbas. Given an average thickness of about 60 m for the rocks of the V iron-bearing horizon and an average ore body thickness of

20-30 m, it is evident that, in a cross-strike section toward the hanging wall, the model must include rock layers of adjacent iron-bearing and shale horizons up to the lateral boundary of the domain; therefore, the geomechanical model is represented as a stratified rock mass.

In the model, the stratigraphic sequence starts with arkosic sandstones of the Skelevatska Suite. Upsection, chlorite-amphibolite schists represent the III-V shale horizon. This is followed by an alternation of productive and barren units: the V iron-bearing horizon consists of martite ores and jaspilites; the VI shale horizon is composed of silicate schists; and the VI iron-bearing horizon comprises martite hornfels. The sequence in the model is completed by the VII shale horizon, which contains chlorite-biotite schists with barren hornfels, and the VII iron-bearing horizon, represented by amphibole-magnetite and martite hornfels. The constructed finite element model is shown in Figure 1.

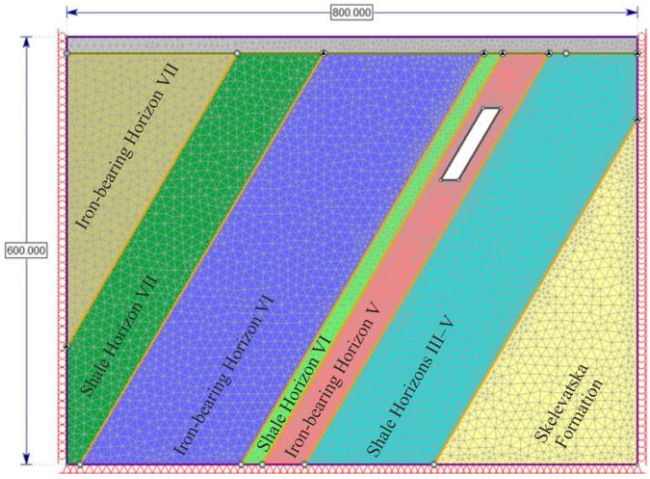

Figure 1. Finite element model of a stratified rock mass containing an unfilled underground void

The numerical modelling scheme involves systematically varying the geometric parameters of underground voids formed by mining blind ore bodies to assess rock mass stability. Five depths of the void roof below the ground surface are considered (50, 100, 150, 200, and 250 m), with an ore body dip of 60° and an average horizontal ore body thickness of 25 m. The void length along the dip is varied as follows: an initial excavation length of 50 m is modelled, after which the length is gradually increased in 10-15 m increments until a size is reached at which the rock mass and the ground surface lose integrity completely.

The geomechanical model employs the physical and mechanical properties of Kryvbas rocks, generalised from the scientific and technical literature. Because the behaviour of the fractured hard-rock mass is described using the Hoek-Brown failure criterion, the built-in RS2 calculator is used to automatically convert the laboratory properties of intact rock (uniaxial compressive strength, σ_{ci}, and Young's modulus, E_i) and rock mass quality indices (GSI, D) into the dimensionless Hoek-Brown parameters required for analysis (mb, s, and a). This approach ensures the correct application of the criterion based on the fundamental rock characteristics. For each lithology, the model specifies both the derived rock mass parameters according to the adopted Hoek-Brown failure criterion (computed using the above procedure) and additional general mechanical properties (density, deformation modulus, compressive strength, and Poisson's ratio). The generalised physical and mechanical properties are presented in Table 1.

In addressing the stated geomechanical problem, rock strength is not treated as a variable parameter. This is because, for relatively weak rocks ($f < 5$), the rock mass above unfilled voids created by mining blind ore bodies several decades ago would, with a high probability, have already collapsed. However, where rock strength is higher ($f = 10$-15), a void may remain in either a stable or a near-failure (collapse-prone) state depending on several controlling factors, including the void depth, the horizontal thickness of the extracted ore body, its extent along the dip, and the dip angle. Therefore, numerical modelling with systematic variation of these conditions enables the identification of potential stress-strain states of the rock mass and the assessment of the risk of ground surface collapse.

Within this study, a two-factor criterion-based approach is proposed to determine the critical void length along the dip, L_c. This approach allows defining the range corresponding to a controlled near-failure state of the rock mass. The bounds of this range are determined by:

– the onset of an unacceptable risk to surface facilities due to ground surface damage, U_{surf};

– the loss of geomechanical stability of the void roof (crown contour), U_{cont}. Together, these criteria define an interval of critical void lengths along the dip within which preventive measures, timely stabilisation/closure of the void using a backfill mixture, are required [35].

Table 1. Physical and mechanical properties of rocks based on the modified Hoek-Brown failure criterion

Rock type	Suite, horizon	GSI	m_b	S	a	E_i, GPa	γ, t/m^3	σ_{ci}, MPa	E_i, GPa	ν
Arkosic sandstones	Skelevatska suite	45	1.99 / 1.16	0.0012 / 0.00024	0.51 / 0.53	7.8	2.63	130	49	0.25
Chlorite-amphibolite schists	III-V shale horizon	30	0.49 / 0.29	0.00041 / 0.000079	0.52 / 0.56	3.0	3.0	110	36	0.22
Martite ores	V iron-bearing horizon	45	1.68 / 0.98	0.0022 / 0.00042	0.5 / 0.52	7.4	3.8	65	33	0.2
Martite jaspilites		45	2.1 / 1.23	0.0022 / 0.00042	0.5 / 0.52	21.2	3.45	170	95	0.18
Silicate schists	VI shale horizon	40	0.7 / 0.41	0.0012 / 0.00024	0.51 / 0.53	7.9	3.2	100	50	0.21
Martite hornfels	VI iron-bearing horizon	35	1.86 / 1.09	0.00073 / 0.00014	0.51 / 0.54	9.1	3.36	150	80	0.21
Chlorite-biotite schists with barren hornfels	VII shale horizon	38	1.09 / 0.64	0.001 / 0.00019	0.51 / 0.53	5.5	2.9	85	39	0.24
Amphibole-magnetite and martite hornfels	VII iron-bearing horizon	40	1.99 / 1.16	0.0012 / 0.00024	0.51 / 0.53	15.1	3.25	140	95	0.21

The first criterion is defined as $U_{surf} \geq 0.2$ m and is based on principles of structural mechanics and safety, and it correlates with regulatory limit deformations for subgrades and foundations [36-38]. Exceeding this threshold indicates the onset of unacceptable deformations that pose a direct risk to the serviceability and integrity of industrial buildings and structures, and also lead to degradation of valuable soils.

The second criterion is the limit displacement of the void contour, U_{cont}, which represents the loss of structural integrity of the void roof (crown) associated with instability of the exposed hanging-wall rocks. The limit displacement is taken as 15% of the horizontal ore-body thickness ($m_h = 25$ m). In our case, $U_{cont} \leq 3.75$ m [39-41]. The adopted displacement limit separates two fundamentally different geomechanical states of the rock mass: before reaching this limit, the roof retains residual load-bearing capacity and behaves as a single quasi-stable structure; once the limit is exceeded, local shear and fracture zones coalesce into a continuous slip surface, and the roof enters a stage of progressive, uncontrolled failure, with the likelihood of ground surface collapse depending on the void depth [42-44].

Geomechanical assessment of the rock mass condition is performed using three indicators that enable both quantitative and qualitative characterisation of the stability of the "void-ground surface" system:

– SF_{surf} is the ground-surface strength factor above the void, which reflects the ratio of the available shear strength of the rocks to the actual shear stresses acting in the near-surface layer of the rock mass;

– U_{surf} is the maximum vertical settlement of the ground surface, indicating the degree of its deformation;

– U_{cont} is the maximum displacement of the contour of the hanging-wall rocks as a response to the loss of support due to the formation of the void.

To justify the required strength of the cemented paste backfill for closing an unfilled void, the contours of the maximum and minimum principal stresses are analysed directly along the rock mass contour, and their quantitative values are obtained using the query function.

3. Results and discussion

As a result of the numerical calculations, a large set of total displacement contours and strength factor contours was obtained for void roof depths in the range of 50-250 m (at 50 m intervals). To avoid excessive graphical loading, contour plots are presented only for the case in which the void roof is located at a depth of $H = 50$ m below the ground surface. For greater depths, the main geomechanical trends are discussed in the text. An analysis of the numerical modelling results for an ore body dip angle of $\alpha = 60°$ and a depth of $H = 50$ m reveals the following features (Figure 2).

To accurately determine the void length along the dip that characterises the near-failure state range and satisfies the adopted criteria ($U_{surf} \geq 0.2$ m, $U_{cont} \leq 3.75$ m), linear interpolation between discrete modelling steps was applied. Because the numerical analysis was performed using fixed increments of the void length along the dip ($L = 52.1$; 78.1; 91.2; 104.2 and 117.2 m), this approach made it possible to reliably estimate the critical length L_c within the interval between adjacent iterations. As a result, the onset of stability loss in the system could be identified with improved mathematical precision, and the lower and upper bounds of the near-failure state could be established.

At a depth of $H = 50$ m, the rock mass exhibits a progressive instability mechanism. Up to a void length of $L = 78.1$ m, the system remains in a stable state (SF > 2.7, $U_{surf} \approx 0$). However, at $L = 91.2$ m, the strength factor decreases to SF = 1.48, ground surface settlement appears ($U_{surf} = 0.26$ m), and local contour displacement develops ($U_{cont} = 1.01$ m). This indicates the initiation of a deformation path within the hanging wall.

Further extension of the void to $L = 104.2$ m leads to a pronounced increase in deformations ($U_{surf} = 2.75$ m, $U_{cont} = 6.0$ m), while at $L = 117.2$ m, a limit state is reached with rock mass collapse ($U_{surf} = 6.9$ m, $U_{cont} = 14.5$ m, SF = 1.0). An increase to $L = 130.2$ m results in complete failure: U_{surf} increases to 12.0 m, and contour displacements reach 24.0 m.

At a depth of $H = 100$ m, the failure stages shift to larger void lengths. Specifically, at $L = 104.2$ m, the system remains stable (SF > 2.6), whereas at L = 117.2 m, a deformation path is already formed ($U_{surf} = 1.2$ m, $U_{cont} = 12.5$ m). The critical state is reached at $L = 130.2$ m (SF = 1.0, $U_{surf} = 3.75$ m, $U_{cont} = 12.6$ m).

At $H = 150$ m, the rock mass shows a further increase in resistance to deformation: the limit state is recorded only at $L = 143.3$ m, while ground surface settlement remains moderate ($U_{surf} = 6.7$ m) relative to internal displacements ($U_{cont} = 24.6$ m), indicating the formation of a natural arch (self-supporting roof).

At depths of $H = 200$-250 m, the system transitions to an internal collapse regime without breakthrough to the ground surface. Even at the maximum analysed void length ($L = 169.3$ m), substantial internal deformations are recorded ($U_{cont} = 26$-28 m), whereas the ground surface remains almost unchanged ($U_{surf} = 1.1$-1.2 m). This indicates a fully developed arching effect and effective attenuation of deformation transmission to the surface.

It is important to note that the loss-of-stability process becomes more abrupt: the system remains stable over a relatively long interval, after which even a minor further increase in void length triggers an avalanche-like transition to complete rock mass collapse, potentially accompanied by the propagation of deformations to the ground surface.

At an ore body (and bedding) dip angle of 60°, the failure mechanism is combined, in which high shear stresses are superimposed on bending stresses. Failure initiates at the void contour, with tensile cracking and the onset of hanging-wall sliding. As a result, the collapse channel propagates along an inclined trajectory, and an asymmetric subsidence trough forms at the ground surface.

Based on the step-by-step analysis of the numerical modelling results, the transition point of the system from a stable state to an intensive deformation-development phase was identified. Ranges of the critical void length along the dip, L_c, were determined, quantitatively characterising the attainment of a near-failure rock mass state. These ranges are summarised in Table 2.

Because the near-failure rock mass state is reached predominantly within the void-depth interval of $H = 50$-150 m, additional simulations were performed at depths of 75 m and 125 m to provide a more detailed representation of deformation development in the rock mass between the void and the ground surface. This densified depth increment yielded more reliable data. The results for the variation of the void length along the dip at $H = 75$ m and $H = 125$ m complement those obtained for $H = 50$, 100, and 150 m.

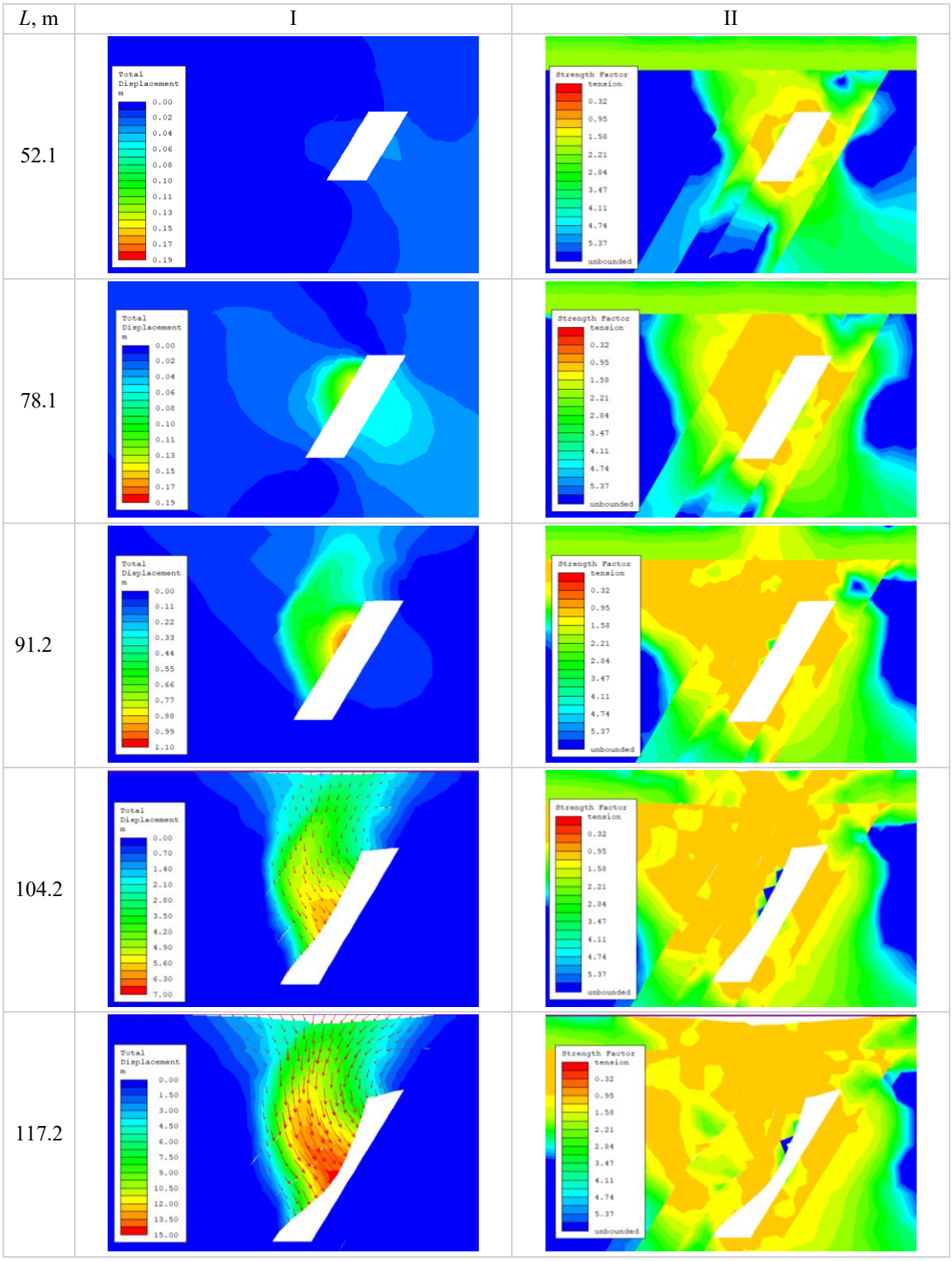

Figure 2. Numerical modelling results (α = 60°): I – total displacement contours; II – strength factor contours

Table 2. Determined ranges of the critical void length along the dip, Lc, characterising the near-failure state of the rock mass between the void and the ground surface

Dip angle, °	Depth (H), m	Range			
		Lower bound, m		Upper bound, m	
		L_c	H/L_c	L_c	H/L_c
60	50	96.2	0.52	106.4	0.47
	75	107.1	0.7	113.6	0.66
	100	117.6	0.85	120.5	0.83
	115	122.3	0.94	125.0	0.92

The conducted set of studies makes it possible to identify regularities in the evolution of the geomechanical state of the rock mass from the formed unfilled underground void (Figure 3), created by mining blind and isolated ore bodies, up to the ground surface, and to directly determine the near-failure state of the rock mass under conditions where sudden ground surface collapse is likely to occur, thereby supporting more reliable prediction and timely implementation of preventive stabilisation measures.

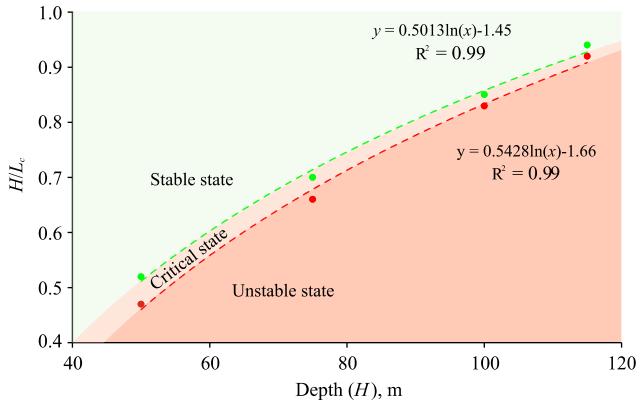

Figure 3. Relationships between the lower and upper bounds of the critical ratio H/Lc and the void depth H for an ore body dip angle of 60°

Analysis of Figure 3 shows a stable nonlinear relationship between the void depth H and the stability parameter H/L_c. The high coefficients of determination ($R^2 = 0.99$) indicate that logarithmic functions accurately approximate these relationships. The main identified regularity is that, as H increases, the ratio H/L_c also increases, directly indicating an increase in geomechanical stability with depth: transition to a limit state at greater depth requires a substantially larger critical void length L_c. Thus, for a dip angle of 60°, the bounds of H/L_c increase from 0.47-0.52 at $H = 50$ m to 0.92-0.94 at $H = 115$ m.

The numerical modelling results also make it possible to predict the ground surface area that is likely to be affected in the absence of preventive measures such as cemented paste backfilling, as well as the potential transition of a void-containing rock mass from a near-failure state to progressive collapse due to degradation of mechanical properties under external factors. During simulations of the near-failure-to-collapse transition, the subsidence trough width across the strike of the ore body was recorded for each geomechanical model. These values were then correlated with the H/L_c ratio and the ore body dip angle α. To establish the governing trends, the upper bound of the near-failure state closest to the onset of rock collapse was adopted. The resulting relationships are shown in Figure 4.

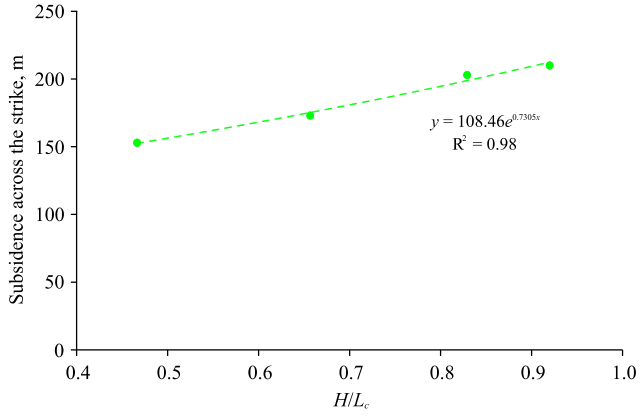

Figure 4. Relationship between the ground surface subsidence trough width and the H/Lc ratio at α = 60° under progressive collapse conditions

The analysis of Figure 4 indicates that the subsidence trough width across the strike of the ore body exhibits a stable exponential increase with increasing geomechanical parameter H/L_c, which is confirmed by the obtained regression equations with high goodness of fit ($R^2 = 0.98$). The area of the potential collapse zone can be estimated by multiplying the across-strike subsidence trough width determined from this relationship by the extent of the underground void along the strike. It was established that during the transition to progressive collapse at a dip angle of 60°, the surface subsidence trough width varies between 150 and 210 m.

To determine the required strength of the backfill mass, a preliminary analysis of the stress distribution after weakening of the surrounding rocks is performed. First, the zone where the load is actually transferred to the backfill is identified, i.e., without the influence of arching effects and local clamping zones near the void corners. In the edge regions of the void, σ_1 may increase artificially due to the contact geometry; however, such stresses do not represent the load that will act on the backfill mass.

The realistic loading on the backfill is associated with the central part of the void contour, away from the corner clamping zone, where $\sigma_3 \approx 0$ and σ_1 are governed primarily by self-weight and by the reduced load-bearing capacity of the hanging wall after degradation. The degraded rock mass zone that will impose the load on the backfill can be delineated by analysing the maximum shear strain contours, in which the constraint region in the corner parts of the void is clearly identifiable. An example is shown in Figure 5.

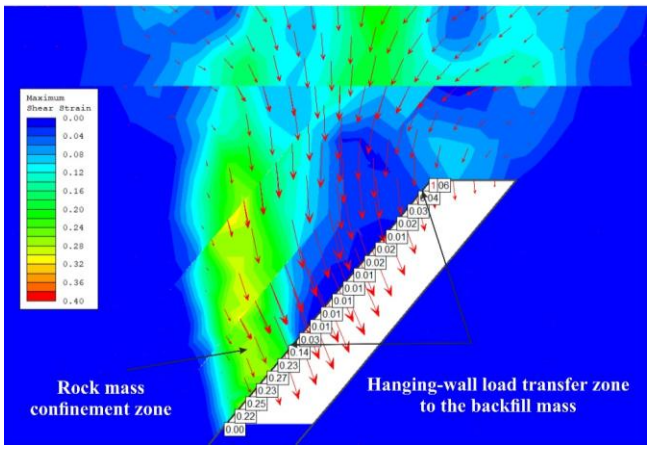

Figure 5. Delineation of the zones of effective rock-to-backfill loading and corner clamping within an underground void based on maximum shear strain contours under rock mass weakening to a collapse state

Analysis of the stress state in the central part of the hanging-wall contour (Figure 5) indicates the development of conditions close to uniaxial compression, where the minimum principal stress $\sigma_3 \approx 0$. Under such conditions, the maximum principal stress σ_1 governs the critical load acting on the backfill mass, which it must sustain without loss of integrity. Therefore, the required uniaxial compressive strength (UCS) of the backfill should satisfy the condition UCS $\geq \sigma_1$.

After identifying the near-failure state of the void for each combination of the H/L_c parameters, the maximum value of σ_1 was determined along the void contour within the effective loading zone (Figure 6), where $\sigma_3 \approx 0$. This value was taken as the required UCS of the backfill mass. Processing the obtained data enabled establishing a relationship between backfill strength and the H/L_c ratio.

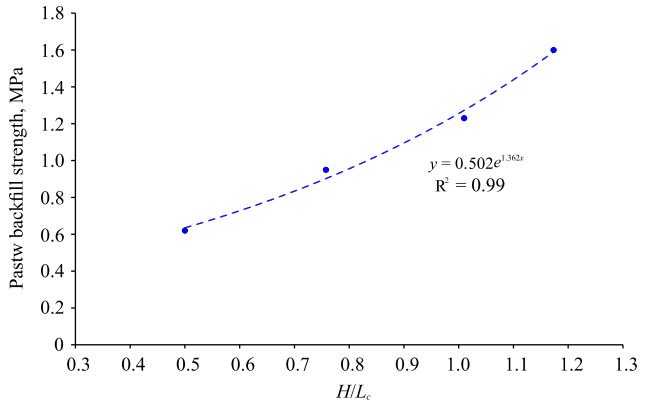

Figure 6. Relationship between the required cemented paste backfill strength and the H/Lc ratio for an ore body dip angle of α = 60°

Analysis of Figure 6 shows a clear exponential relationship between the required cemented paste backfill strength and the geomechanical parameter H/Lc, which characterises the rock mass stress level. As the H/L_c ratio increases (i.e., as the rock mass approaches a near-failure state), the required backfill strength increases nonlinearly, indicating a sharp rise in loads acting on the supporting structure as stability is lost.

Thus, based on the conducted numerical investigations and the derived relationships (Figures 3 and 6), it was established that unfilled underground voids formed by mining blind and isolated ore bodies may be associated not only with stable and unstable geomechanical states of the rock mass, but also with a distinct near-failure state. This state represents the onset of integrity loss and is characterised by a developed deformation coupling between the void and the surface.

The near-failure state occurs within the critical range H/L_c = 0.5-1.2 and is defined by lower and upper bounds that increase logarithmically with void depth. In contrast, the interval between these bounds decreases with increasing ore body dip angle. In this state, the required cemented paste backfill strength exhibits an exponential dependence on H/Lc, increasing as the dip angle decreases. The obtained relationships provide a scientifically grounded basis for identifying voids in a near-failure state, selecting the required backfill strength, and proactively preventing the development of progressive ground surface deformations.

A promising direction for further research is to extend the present analysis to establish more general regularities governing the transition of the rock mass to a near-failure state. In particular, it is advisable to perform similar numerical modelling for ore bodies with other dip angles, such as 50° and 70°, which would allow a quantitative assessment of the influence of this crucial geometric factor. A comprehensive synthesis of the resulting data would support the development of a more universal and reliable methodology for predicting the stability of rock masses above unfilled underground voids and for improving the robustness of geomechanical risk assessment.

For the large iron ore basin considered in this study, a topical problem is the development of deep ground-surface collapse zones induced by active underground mining. Therefore, it is reasonable to numerically model the further evolution of collapse zones and hanging-wall deformations as the mining depth increases, and to evaluate how the formation of a monolithic cemented paste backfill mass within the created voids can alter the geomechanical setting as an engineering measure to block or attenuate deformation propagation.

4. Conclusions

A numerical modelling methodology was developed based on a two-dimensional finite-element geomechanical model of the stratified hard-rock mass of the Kryvbas, which contains an unfilled underground void. The model accounts for the failure behaviour of fractured rocks by applying the Hoek-Brown failure criterion and representing the actual weakened rock mass condition using a justified Geological Strength Index (GSI). This modelling approach enables parametric studies by systematically varying void depth and size, allows identification of the conditions under which the rock mass enters a hazardous near-failure state, and provides direct predictions of ground surface stability.

It was established that unfilled underground voids formed by mining blind and isolated ore bodies are associated not only with stable and unstable geomechanical states of the rock mass, but also with a distinct near-failure state at the threshold of integrity loss, characterised by a developed deformation linkage with the ground surface. The near-failure state develops within the critical range H/L_c = 0.5-1.2 and is bounded by lower and upper limits that increase logarithmically with increasing void depth. In contrast, the interval between these bounds decreases as the ore body dip angle increases. Within the near-failure state, the required cemented paste backfill strength exhibits an exponential dependence on H/L_c, increasing as the dip angle decreases.

Author contributions

Conceptualization: MP; Data curation: KS; Formal analysis: MP; Funding acquisition: MP; Investigation: MP, KS; Methodology: MP; Project administration: MP; Resources: KS; Supervision: MP; Validation: MP, KS; Visualization: KS; Writing – original draft: MP, KS; Writing – review & editing: MP, KS. All authors have read and agreed to the published version of the manuscript.

Funding

Research was carried out within the framework of the applied scientific project “Development of novel applied and regulatory solutions for resource-efficient utilization of technogenic waste and elimination of mining-induced voids in ore-mining regions within the context of the circular economy” (State registration No. 0126U001271), funded by the Ministry of Education and Science of Ukraine.

Acknowledgements

The authors sincerely thank the reviewers for their thorough evaluation of the manuscript and for their constructive comments and suggestions, which substantially improved the scientific quality of this paper. The authors also express their appreciation to the Editor for coordinating the review process and for valuable guidance during the revision stage.

Conflicts of interest

The authors declare no conflict of interest.

Data availability statement

The original contributions presented in this study are included in the article. Further inquiries can be directed to the corresponding author.

References

[1] Initiative to ensure vision for shoe wearers in Ukraine for 2021. (2023). Report. Kyiv, Ukraine: Ministry of Energy of Ukraine, 581 p.

[2] Peremetchyk, A., Chukharev, S., Dmytrenko, V., Pysmennyi, S., Fedorenko, S., & Mutambo, V. (2024). Application of geometrization to estimate mineral deposit reserves. *IOP Conference Series: Earth and Environmental Science*, *1415*(1), 012025. https://doi.org/10.1088/1755-1315/1415/1/012025

[3] Petlovanyi, M., Sai, K., Khalymendyk, O., Borysovska, O., & Sherstiuk, Y. (2023). Analytical research of the parameters and characteristics of new "quarry cavities – backfill material" systems: Case study of Ukraine. *Mining of Mineral Deposits*, *17*(3), 126-139. https://doi.org/10.33271/mining17.03.126

[4] Bazaluk, O., Petlovanyi, M., Sai, K., Chebanov, M., & Lozynskyi, V. (2024). Comprehensive assessment of the earth's surface state disturbed by mining and ways to improve the situation: case study of Kryvyi Rih Iron-ore Basin, Ukraine. *Frontiers in Environmental Science*, 12. https://doi.org/10.3389/fenvs.2024.1480344

[5] Batur, M., & Babii, K. (2022). Spatial assessment of air pollution due to mining and industrial activities: A case study of Kryvyi Rih, Ukraine. *IOP Conference Series: Earth and Environmental Science*, *970*(1), 012004. https://doi.org/10.1088/1755-1315/970/1/012004

[6] Ivanchenko, A.V. (2025). Utilization of waste from iron ore mining: the example of the Pokrovska mine in the Kryvyi Rih basin. *Mineral Resources of Ukraine*, (3), 46-50. https://doi.org/10.31996/mru.2025.3.46-50

[7] National report on the state of the natural environment in Ukraine in 2021. (2022). Kyiv, Ukraine: Ministry of Environmental Protection and Natural Resources of Ukraine, 514 p.

[8] Popovych, V., Kuzmenko, O., Voloshchyshyn, A., & Petlovanyi, M. (2018). Influence of man-made edaphotopes of the spoil heap on biota. *E3S Web of Conferences*, *60*, 00010. https://doi.org/10.1051/e3sconf/20186000010

[9] Babii, K.V., & Malieiev, Ye. V. (2024). The new engineering and technological decisions for mine technical reclamation of deep open pits to regenerate mesorelief. *Mineral Resources of Ukraine*, (4), 82-87. https://doi.org/10.31996/mru.2024.4.82-87

[10] Zhienbayev, A., Takhanov, D., Zharaspaev, M., Kuttybayev, A., Rakhmetov, B., & Ivadilinova, D. (2025). Identifying rational locations for field mine workings in the zone influenced by mined-out space during repeated mining of pillars. *Mining of Mineral Deposits*, *19*(1), 1-12. https://doi.org/10.33271/mining19.01.001

[11] Hrinov, V.H., & Khorolskyi, A.O. (2022). Determination the feasibility of mining deposits at the stage of pre-project studies of a rational strategy for their development. *Mineral Resources of Ukraine*, (2), 12-17. https://doi.org/10.31996/mru.2022.2.12-17

[12] Malashkevych, D., Petlovanyi, M., Sai, K., & Zubko, S. (2022). Research into the coal quality with a new selective mining technology of the waste rock accumulation in the mined-out area. *Mining of Mineral Deposits*, *16*(4), 103-114. https://doi.org/10.33271/mining16.04.103

[13] Kuznetsov, M.A., Akimov, A.G., Kuzmin, V.I., Panteleev, M.G., & Chernyshov, M.F. (1971). *Rock displacement at ore deposits*. Nedra, 224 p.

[14] Rules for the protection of structures and natural objects from the harmful effects of underground mining in the Kryvyi Rih iron ore basin. (1975). VNIMI, 67 p.

[15] Kalinichenko, V., Dolgikh, O., Dolgikh, L., & Pysmennyi, S. (2020). Choosing a camera for mine surveying of mining enterprise facilities using unmanned aerial vehicles. *Mining of Mineral Deposits*, *14*(4), 31-39. https://doi.org/10.33271/mining14.04.031

[16] Petlovanyi, M. (2024). Features of surface subsidence zones formed under the influence of underground mining of steeply dipping ore deposits in the Kryvyi Rih iron ore basin. *Collection of Research Papers of National Mining University*, *79*, 63-83. https://doi.org/10.33271/crpnmu/79.063

[17] Petlovanyi, M., & Sai, K. (2024). Research into cemented paste backfill properties and options for its application: Case study from a Kryvyi Rih Iron-ore Basin, Ukraine. *Mining of Mineral Deposits*, *18*(4), 162-179. https://doi.org/10.33271/mining18.04.162

[18] Akhmetkanov, D.K., Bitimbayev, M.Zh., Lozynskyi, V., Rysbekov, K.B., & Amralinova, B.B. (2023). New variants for wide orebodies highcapacity mining systems with controlled and continuous in-line stoping. *News of the National Academy of Sciences of the Republic of Kazakhstan, Series of Geology and Technical Sciences*, *3*(459), 6-21. https://doi.org/10.32014/2023.2518-170X.295

[19] Petlovanyi, M.V., Zubko, S.A., Popovych, V.V., & Sai, K.S. (2020) Physicochemical mechanism of structure formation and strengthening in the backfill massif when filling underground cavities. *Voprosy Khimii i Khimicheskoi Tekhnologii*, (6), 142-150. https://doi.org/10.32434/0321-4095-2020-133-6-142-150

[20] Wang, Y., & Xiao, B. (2024). Mechanical properties of hardening cemented paste backfill (CPB). *Cemented Paste Backfill*, 137-202. https://doi.org/10.1016/b978-0-443-16054-7.00005-9

[21] Stupnik, M.I., Kalinichenko, V.O., Muzyka, I.O., Fedko, M.B., & Pysmennyi, S.V. (2015). Investigation of the stress-deformed state of the mine massif of magnetite quartzites in the mines of the Gigant-Glyboka mine of PJSC "TsGZK". *Metallurgy and Mining Industry*, (5), 85-88.

[22] Pysmennyi, S., Fedko, M., Peremetchyk, A., Chukharev, S., Pilchyk, V., & Mutambo, V. (2024). Improvement of the stoping technology in mining magnetite quartzite by underground methods. *E3S Web of Conferences*, (526), 01023. https://doi.org/10.1051/e3sconf/202452601023

[23] Stupnik, M., Kalinichenko, O., Kalinichenko, V., Pysmennyi, S., & Morhun, O. (2018). Choice and substantiation of stable crown shapes in deep-level iron ore mining. *Mining of Mineral Deposits*, *12*(4), 56-62. https://doi.org/10.15407/mining12.04.056

[24] Khomenko, O., Kononenko, M., & Petlovanyi, M. (2015). Analytical modeling of the backfill massif deformations around the chamber with mining depth increase. *New Developments in Mining Engineering 2015*, 265-269. https://doi.org/10.1201/b19901-47

[25] Khomenko, O., Kononenko, M., & Petlyovanyy, M. (2014). Investigation of stress-strain state of rock massif around the secondary chambers. (2014). *Progressive Technologies of Coal, Coalbed Methane, and Ores Mining*, 253-258. https://doi.org/10.1201/b17547-43

[26] Zhang, Z.X., Xu, Y., Kulatilake, P.H.S.W., & Huang, X. (2012). Physical model test and numerical analysis on the behavior of stratified rock masses during underground excavation. *International Journal of Rock Mechanics and Mining Sciences*, (49), 134-147. https://doi.org/10.1016/j.ijrmms.2011.11.001

[27] Einstein, H. (2024). Physical Modelling in Rock Mechanics and Rock Engineering. *Rock Mechanics and Rock Engineering*, *57*(12), 10187-10204. https://doi.org/10.1007/s00603-024-04106-y

[28] Stupnik, M.I., Kalinichenko, V.O., Pysmennyi, S.V., & Kalinichenko, O.V. (2018). Determining the qualitative composition of the equivalent material for simulation of Kryvyi Rih iron ore basin rocks. *Naukovyi Visnyk Natsionalnoho Hirnychoho Universytetu*, (4), 21-27. https://doi.org/10.29202/nvngu/2018-4/4

[29] Petlovanyi, M., Sai, K., Malashkevych, D., Popovych, V., & Khorolskyi, A. (2023). Influence of waste rock dump placement on the geomechanical state of underground mine workings. *IOP Conference Series: Earth and Environmental Science*, *1156*(1), 012007. https://doi.org/10.1088/1755-1315/1156/1/012007

[30] Li, S.C., Feng, X.D., & Li, S.C. (2013). Numerical model for the zonal disintegration of the rock mass around deep underground workings. *Theoretical and Applied Fracture Mechanics*, 65-73. https://doi.org/10.1016/j.tafmec.2013.11.005

[31] Moldabayev, S.K., Sdvyzhkova, O.O., Babets, D.V., Kovrov, O.S., & Adil, T.K. (2021). Numerical simulation of the open pit stability based on probabilistic approach. *Naukovyi Visnyk Natsionalnoho Hirnychoho Universytetu*, (6), 29-34. https://doi.org/10.33271/nvngu/2021-6/029

[32] Bondarenko, V.I., Sheka, I.V., Khorolskyi, A.O., Salieiev, I.A., Kovalevska, I.A., & Stoliarska, O.V. (2025). Substantiation of

rational parameters for composite support in mine workings. *Naukovyi Visnyk Natsionalnoho Hirnychoho Universytetu*, (3), 58-64. https://doi.org/10.33271/nvngu/2025-3/058

[33] Hoek, E., & Brown, E.T. (2019). The Hoek-Brown failure criterion and GSI – 2018 edition. *Journal of Rock Mechanics and Geotechnical Engineering*, *11*(3), 445-463. https://doi.org/10.1016/j.jrmge.2018.08.001

[34] Sdvyzhkova, O., Moldabayev, S., Babets, D., Bascetin, A., Asylkhanova, G., Nurmanova, A., & Prykhodko, V. (2024). Numerical modelling of the pit wall stability while optimizing its boundaries to ensure the ore mining completeness. *Mining of Mineral Deposits*, *18*(2), 1-10 https://doi.org/10.33271/mining18.02.001

[35] Kuzmenko, O., Dychkovskyi, R., Petlovanyi, M., Buketov, V., Howaniec, N., & Smolinski, A. (2023). Mechanism of Interaction of Backfill Mixtures with Natural Rock Fractures within the Zone of Their Intense Manifestation while Developing Steep Ore Deposits. *Sustainability*, 15(6), 4889. https://doi.org/10.3390/su15064889

[36] Kratzsch, H. (2012). *Mining subsidence engineering*. Berlin: Springer Science & Business Media, 546 p. https://doi.org/10.1007/978-3-642-81923-0

[37] Subsidence engineer's handbook. (1975). London: National Coal Board, 111 p.

[38] Ministry of Regional Development and Construction of Ukraine. (2009). *State Building Codes of Ukraine DBN V.2.1-10:2009. Foundations and bases of structures*. Basic design provisions]. Kyiv, Ukraine.

[39] Sofianos, A.I. (1996). Analysis and design of an underground hard rock voussoir beam roof. *International Journal of Rock Mechanics and Mining Sciences & Geomechanics Abstracts*, *33*(7), A316. https://doi.org/10.1016/0148-9062(96)83532-7

[40] Reddish, D.J., & Whittaker, B.N. (2012). *Subsidence: occurrence, prediction and control*. New York: Elsevier, 525 p.

[41] Brady, B.H., & Brown, E.T. (2006). *Rock mechanics: For underground mining*. Queensland: Springer, 614 p.

[42] Abdiev, A.R., Wang, J., Mambetova, R.S., Abdiev, A.A., & Abdiev, A.S. (2025). Geomechanical assessment of stress-strain conditions in structurally heterogeneous rock masses of Kyrgyzstan. *Engineering Journal of Satbayev University*, *147*(2), 31-39. https://doi.org/10.51301/ejsu.2025.i2.05

[43] Uakhitova, B., Almatova, B., Balgynova, A., Shilmagambetova, Z., Arystan, I., Kurantayeva, A., & Karabatyrova, A. (2025). Comprehensive geomechanical assessment of pillar and roof stability during secondary extraction by the room-and-pillar method. *Mining of Mineral Deposits*, *19(*3), 144-160. https://doi.org/10.33271/mining19.03.144

[44] Petlovanyi, M., Chebanov, M., Sai, K., & Khalymendyk, O. (2025). A new approach to restoring the earth's surface heavily disturbed by mining activities. *IOP Conference Series: Earth and Environmental Science*, *1481*(1), 012004. https://doi.org/10.1088/1755-1315/1481/1/012004

Темір кені кен орындарындағы жерасты қуыстарының айналасында тау жыныстары массивінің шекаралық күйінің қалыптасуының критикалық шарттарын сандық модельдеу

М. Петлёваный*, К. Сай

Ұлттық «Днепровск политехникасы» техникалық университеті, Днепр, Украина

**Корреспонденция үшін автор: petlovanyi.m.v@nmu.one*

Аңдатпа. Жұмыстың мақсаты – сандық модельдеу негізінде орнықтылықтың жоғалуына және жер бетінің опырылуына қауіпті шекті күйдегі, жойылмаған жерасты қуыстарының айналасындағы тау жыныстары массивінің жай-күйін сандық бағалау және болжау тәсілін әзірлеу. Зерттеу RS2 бағдарламалық кешенінде соңғы элементтер әдісімен қабатты жыныстар массивінің кернеулі-деформацияланған күйін (КДК) сандық модельдеу арқылы орындалды. Кривой Рог теміркен бассейніндегі жарықшақты жыныстардың механикалық мінез-құлқын барабар қайта жаңғырту үшін массивтің стратиграфиялық ерекшеліктері ескерілді. Геологиялық беріктік индексін (GSI) ескере отырып, Хоек–Брауннның сызықтық емес беріктік критерийі қолданылды. Жойылмаған жерасты қуыстарының айналасында орнықты және орнықсыз күйлердің арасында қалыптасатын, жер бетімен деформациялық байланысының болуымен сипатталатын тау жыныстары массивінің шекаралық (бұзылуға жақын) геомеханикалық күйі бар екені анықталды. Қуыстың жату тереңдігіне байланысты H/Lкр критикалық қатынасының төменгі және жоғарғы шекараларының орнықты логарифмдік тәуелділігі анықталды; бұл тереңдік артқан сайын массивтің шекті күйге өтуіне қарсылығының сандық тұрғыдан ұлғаюын көрсетеді. H/Lкр көрсеткішіне байланысты жер бетінің шөгу мульдасы өлшемінің экспоненциалдық тәуелділігі белгіленді, бұл әлеуетті опырылу аймағының ауданын болжауға мүмкіндік береді. Қажетті пасталы закладка массиві беріктігінің осы қатынасқа экспоненциалдық тәуелділігі анықталып, шекаралық күй жағдайында оның ең төменгі көтергіш қабілетіне қойылатын талаптарды айқындайды. Алғаш рет жойылмаған жерасты қуыстарының айналасындағы тау жыныстары массивінің шекаралық күйінің жер бетінің үдемелі опырылуына дейінгі дербес геомеханикалық күй ретінде бар екені сандық тұрғыда негізделді. Алынған тәуелділіктер жойылмаған қуыстар үстіндегі массивтің геомеханикалық жай-күйін болжауға, олардың критикалық геометриялық параметрлерінің ауқымын анықтауға және шекаралық күйдегі қуыстарды уақтылы айқындауға мүмкіндік береді. Әзірленген тәсіл жер бетінің кенет опырылуын болдырмау мақсатында жер бетінен цементтелген пасталы закладка параметрлерін инженерлік негіздеуде қолданылуы мүмкін.

Негізгі сөздер: *сандық модельдеу, жерасты қуысы, қабатты әртекті тау жыныстары массиві, Хоек–Браун критерийі, шекаралық күй, құлау, пасталы закладка.*

Численное моделирование критических условий формирования предельного состояния массива горных пород вокруг подземных пустот железорудных месторождений

М. Петлёваный*, К. Сай

Национальный технический университет «Днепровская политехника», Днепр, Украина

**Автор для корреспонденции: petlovanyi.m.v@nmu.one*

Аннотация. Целью работы является разработка подхода к количественной оценке и прогнозированию состояния массива горных пород вокруг непогашенных подземных пустот в предельном состоянии, опасном к потере устойчивости и обрушения земной поверхности, на основе численного моделирования. Исследование выполнено с использованием численного моделирования напряженно-деформированного состояния (НДС) слоистого скального массива методом конечных элементов в программном комплексе RS2. Для адекватного воспроизведения механического поведения трещиноватых пород Криворожского железорудного бассейна учтены стратиграфические особенности массива. Применен нелинейный критерий прочности Хоека-Брауна с учетом индекса геологической прочности (GSI). Установлено существование приграничного (приближенного к разрушению) геомеханического состояния массива горных пород вокруг непогашенных подземных пустот, формирующегося между устойчивым и неустойчивым и характеризующегося наличием деформационной связи с земной поверхностью. Выявлена устойчивая логарифмическая зависимость нижней и верхней границ критического соотношения $H/L_{кр}$ от глубины залегания пустоты, количественно отражающая возрастание сопротивления массива переходу в предельное состояние с увеличением глубины. Установлена экспоненциальная зависимость размера мульды сдвижения земной поверхности от показателя $H/L_{кр}$, что позволяет прогнозировать площадь потенциальной зоны обрушения. Выявлена экспоненциальная зависимость требуемой прочности пастового закладочного массива от соотношения, определяющая минимальные требования к его несущей способности в условиях приграничного состояния массива. Впервые количественно обосновано существование приграничного состояния массива горных пород вокруг непогашенных подземных пустот как самостоятельного геомеханического состояния, предшествующего прогрессирующему обрушению земной поверхности. Полученные зависимости позволяют осуществлять прогноз геомеханического состояния массива над непогашенными пустотами, определять диапазон их критических геометрических параметров и своевременно идентифицировать пустоты, находящиеся в приграничном состоянии. Разработанный подход может быть использован для инженерного обоснования параметров цементированной пастовой закладки с поверхности с целью предупреждения внезапных обрушений земной поверхности.

Ключевые слова: *численное моделирование; подземная пустота; слоистый неоднородный массив; критерий Хоека-Брауна; приграничное состояние; обрушение; пастовая закладка.*

Publisher's note

All claims expressed in this manuscript are solely those of the authors and do not necessarily represent those of their affiliated organizations, or those of the publisher, the editors and the reviewers.

SATBAYEV UNIVERSITY

Engineering Journal of Satbayev University

Volume 148 (2026), Issue 1, 48-55

https://doi.org/10.51301/ejsu.2026.i1.06

Implementation of the 1992 Helsinki Convention in Transboundary Groundwater Management: A Comparative Analysis with the Case of the Shu Basin

D.K. Adenova[1*], Ye.Zh. Murtazin[1], J. Sagin[2], E.V. Sotnikov[1], S.R. Tazhiyev[1], A.M. Baikadamova[1]

[1]*Institute of Hydrogeology and Geoecology named after U.M. Akhmedsafin, Almaty, Kazakhstan*

[2]*Departmant of Geological and Environmental Sciences, Western Michigan University, Kalamazoo, USA*

**Corresponding author: adenovadinara@gmail.com*

Abstract. In the context of increasing freshwater scarcity and climate change, effective transboundary water management, including groundwater resources, is particularly important. The 1992 Helsinki Convention provides an international legal basis for states to cooperate to protect and rationally use transboundary watercourses and aquifers. This article is aimed at a comparative analysis of the practice of implementing the provisions of the Convention in different regions of the world - Europe, Central Asia and Africa - with an emphasis on hydrogeological aspects. Particular attention is paid to the Shuya transboundary basin, located on the territory of Kazakhstan and Kyrgyzstan, as a case of partial implementation of international standards. Based on a systemic analysis of groundwater management, monitoring, and protection practices, recommendations are proposed to integrate the Convention's provisions into regional water policies and institutional mechanisms. The study aims to conduct a comparative analysis of the practice of applying the 1992 Helsinki Convention in various regions of the world, with an emphasis on transboundary groundwater, highlighting the problems and prospects of its implementation using the example of the Shuya basin. The study confirmed that the application of the 1992 Helsinki Convention varies significantly across geographical and political-institutional contexts.

Keywords: *transboundary groundwater, water security, legal regulation, Central Asia.*

Received: 23 June 2025
Accepted: 14 February 2026
Available online: 28 February 2026

1. Introduction

Rational use and protection of transboundary water resources are key tasks in sustainable water management, especially amid increasing global environmental challenges and climate change. Today, against the backdrop of increasing anthropogenic impact, urbanization, agricultural pressure and changing hydroclimatic conditions, the vulnerability of both surface and groundwater systems is increasing. In particular, there are stable trends towards decreases in groundwater levels, increases in mineralization, degradation of aquifers, and disruption of natural water exchange regimes [1-4].

At the same time, the transboundary interdependence of states sharing common water resources is increasing. This is particularly relevant in arid and semi-arid regions where transboundary rivers and aquifers are the only source of fresh water for millions of people. Conflicts of interest between countries over the distribution and use of water are increasingly becoming the subject of not only technical but also political and legal discussions [5-8].

In these conditions, the development and implementation of effective international legal regulatory mechanisms capable of ensuring fair and sustainable management of water resources, protection of aquatic ecosystems and prevention of transboundary water conflicts becomes particularly relevant [9, 10]. The 1992 Helsinki Convention plays a key role in this process, the first universal international treaty aimed at promoting cooperation in the protection and use of transboundary waters [11, 12].

However, practice shows that the degree of implementation of the Convention varies significantly from region to region. In some cases, it has served as the basis for the creation of sustainable institutions and comprehensive management programs, while in others, its provisions remain formal declarations, unsupported by institutional or technical implementation. This is especially true for components such as groundwater, which often remain outside the scope of transboundary regulation despite their critical importance for sustainable water use.

Thus, in the context of increasing water and environmental pressures and transboundary challenges, the development of effective models of international water cooperation grounded in the principles of the Convention is not only desirable but also a necessary condition for ensuring water security in the 21st century [13-15].

One of the key international documents in this area, as mentioned above, is the UNECE Convention on the Protection and Use of Transboundary Watercourses and Interna-

adenovadinara@gmail.com; ye_murtazin@list.ru; jay.sagin@wmich.edu; sotnikov_yevgeniy@mail.ru; sula_tashiev@mail.ru; ainurchuk90@mail.ru
Engineering Journal of Satbayev University. eISSN 2959-2348. Published by Satbayev University

tional Lakes (Helsinki, 1992) [12], which has now moved from a regional to a global status, becoming a universal instrument of international water law. The Convention establishes principles of cooperation among states for preventing transboundary impacts, exchanging information, monitoring, and protecting groundwater [16, 17].

Of particular interest in the comparative analysis is the Central Asian region, where transboundary rivers and groundwater aquifers play a key role in ensuring water and food security. An example is the Shu transboundary basin, located on the territories of Kyrgyzstan and Kazakhstan, including the Zhambyl region, where essential groundwater resources are formed and used for drinking and agricultural water supply. Despite the existence of an interstate agreement on joint management (2000) [18], issues of integrating the provisions of the Helsinki Convention, particularly regarding groundwater protection and monitoring, remain insufficiently developed [19, 20].

The purpose of this study is to conduct a comparative analysis of the application of the 1992 Helsinki Convention across various geographical and institutional contexts (Europe, Central Asia, Africa), with an emphasis on hydrogeological aspects and an assessment of the degree of implementation of the key provisions in transboundary basins. Particular attention is paid to the Central Asian region as a zone of complex water resource challenges and potential application of international legal norms.

2. Materials and methods

The methodological framework of this study combines complementary analytical approaches to assess the implementation of the 1992 Helsinki Convention across diverse geographical and institutional contexts, with particular emphasis on transboundary groundwater [11, 12].

First, a comparative analytical approach was employed to identify similarities and differences in the application of the Convention in Europe, Central Asia, and Africa. The comparison was structured according to predefined criteria, including: the legal status of the Convention, the level of institutionalization of transboundary cooperation, the inclusion of groundwater in basin management frameworks, monitoring mechanisms, and procedures for data exchange [21].

Second, geoecological and hydrogeological analyses were conducted to evaluate aquifer conditions, groundwater mineralization levels, seasonal variability of groundwater levels, and vulnerability to anthropogenic pressures. Particular attention was given to the Shu transboundary basin, encompassing the Zhambyl region of Kazakhstan and the adjacent territories of Kyrgyzstan.

Third, a content analysis of legal and institutional documents was performed, including bilateral and multilateral water agreements, official UNECE materials, and strategic documents of national and regional water authorities [22, 23]. This approach enabled an assessment of both formal compliance and the practical implementation of Convention principles within regional governance systems.

Fourth, a case study methodology was applied to the Shu transboundary basin. This approach facilitated an in-depth examination of institutional arrangements, hydrogeological characteristics, existing coordination mechanisms, and the potential for adapting international standards to the regional level [24-26]. In addition, geographic information system (GIS) data, cartographic materials, and available groundwater monitoring reports from the Zhambyl region were analyzed. Where data permitted, spatial visualization of aquifer distribution and groundwater availability dynamics was conducted to support the comparative assessment [27-30].

The integrated application of these methods ensured both regulatory-institutional and hydrogeological depth of analysis, providing a foundation for evidence-based recommendations for transboundary groundwater governance within the framework of international legal instruments.

3. Results and discussion

3.1. Institutional and legal frameworks in transboundary water management

3.1.1. European experience in the Danube Basin

In the European region, the 1992 Helsinki Convention has not only been widely ratified but also integrated into transboundary water management practices through sustainable institutional arrangements. One of the most illustrative examples is the International Commission for the Protection of the Danube River, which unites 14 countries in the basin [31, 32].

Based on the Convention and the EU Water Framework Directive (2000/60/EC) [33], Danube River Basin Management Plans have been developed and implemented, in which groundwater is considered alongside surface water within a single hydrological unit. Systems for monitoring groundwater quality and levels have been implemented, and regular data exchange is carried out between countries.

Particularly noteworthy is the inclusion of transboundary aquifers in strategic management, such as the karst and alluvial systems along the Upper and Middle Danube. Methods for assessing aquifers, mapping vulnerability zones and establishing sampling standards have been developed. A critical component is the participation of all basin countries in unified reporting and planning cycles (every 6 years), which fosters high transparency and mutual responsibility.

In Europe, the Danube basin is one of the most successful examples of implementing the principles of the 1992 Helsinki Convention. It implements integrated transboundary management, including both surface and groundwater. This was made possible by a combination of international legal mechanisms (including the Helsinki Convention and the EU Water Framework Directive) [11, 12, 34], a high level of institutional coordination and technical sophistication of monitoring.

Particular attention in the Danube Region is paid to transboundary groundwater bodies, which play an essential role in water supply, agriculture, and the maintenance of ecosystems. Within the framework of the activities of the International Commission for the Protection of the Danube River, several hydrogeological studies were carried out and a register of TGWBs was created, covering 11 major aquifers, including: Karst aquifers in Austria, Slovakia, Hungary and Slovenia; Pannonian Basin aquifers, covering Hungary, Serbia, Romania; alluvial and fluvioglacial systems in the lower and middle reaches of the Danube [35-37].

Each ICPDR Member State is required to provide information on groundwater status, water abstraction volumes, pollution sources, and the risk of depletion. This information is synthesised within the framework of the joint Danube Basin Management Plan, where groundwater is considered as an integral part of «water bodies» in accordance with the EU Framework Directive [38, 39].

A coordinated monitoring system has been technically implemented, including general parameters (pH, mineralization, nitrates, heavy metal concentrations), as well as an assessment of the chemical and quantitative state of groundwater. The integration of GIS systems and joint data platforms ensures rapid exchange of information between countries.

The legal framework for cooperation includes not only the provisions of the Helsinki Convention, but also special regional agreements, such as: the Danube River Protection Agreement [11, 12, 34], which clearly sets out obligations for groundwater management; joint technical guidelines for assessing the risk of groundwater pollution; participation of countries in the EU Climate Change Adaptation Strategy, which recognizes groundwater as a strategic resource.

Thus, the European experience shows that it is possible to implement the principles of integrated water management, in which groundwater is not separated from surface water and is considered within a single ecosystem and legal framework. This creates sustainable forms of cross-border interaction based on trust, scientific evidence and legal responsibility. The European experience shows that multilateral agreements and directives complementing the Convention's provisions provide not only a legal framework but also effective institutional implementation.

3.1.2. Transboundary cooperation in the Nile Basin

The Nile River basin, spanning 11 countries, is one of the largest and most politically sensitive transboundary water bodies in the world. Although the 1992 Helsinki Convention has been ratified by only a fraction of the countries in the region, its principles, including equitable and reasonable use, prevention of significant harm, and the exchange of information, have been partially implemented through regional initiatives and agreements [40-42].

The key mechanism for cooperation in the Nile Basin is the Nile Basin Initiative [42], founded in 1999. It unites all riparian states and seeks a sustainable, equitable distribution of water resources. Unlike European models, there is no single legally binding agreement covering the entire basin, reflecting the complex political environment and the differences in interests between upstream and downstream countries [43].

As for groundwater, its role in basin management has long remained secondary. However, in recent years, there has been growing interest in transboundary aquifers, particularly in the arid border areas between Sudan, South Sudan, Ethiopia and Uganda. Key underground systems include the deep Nubian Sandstone Aquifer System, partly connected to the eastern Nile Basin, and the aquifers of the East African Rift System, which are heavily used to supply rural populations and are under pressure due to climate fluctuations [44-47].

The NBI is implementing projects to improve monitoring and create groundwater databases, but there is still no agreed institutional system for managing them. Most research is funded by international donors (GEF, World Bank) [48], and implementation at the national level is often not synchronized across countries.

Specific challenges for groundwater include: limited data on water supplies and quality; lack of standards for transboundary information exchange; inconsistent licensing of water abstraction in border areas; climate vulnerability and weak institutional integration.

Thus, the experience of the Nile River basin demonstrates a partial implementation of the principles of the Helsinki Convention, with a primary focus on surface waters and an initial phase of accounting for groundwater resources. However, the potential of groundwater as a sustainable resource in a changing climate requires increased regional cooperation, scientific research and the establishment of a legally binding framework.

3.1.3. The Shu transboundary basin in Central Asia

The Shu transboundary basin, located on the territories of Kazakhstan and Kyrgyzstan, is a vital water management system in Central Asia's arid climate. The main watercourse, the Shu River, crosses the state border, providing water for irrigation, municipal services and partly industry in both countries. The basin is characterized not only by a well-developed surface water system but also by significant groundwater reserves, which, however, are not sufficiently accounted for in transboundary water management [49].

Kazakhstan ratified the 1992 Helsinki Convention in 2001, while Kyrgyzstan remains only a participant in several UNECE programs. At the same time, bilateral agreements are in force in the region, including the Agreement between the governments of Kazakhstan and Kyrgyzstan on the joint use of water management facilities on the Shu and Talas rivers (2000) [50]. This document creates coordination mechanisms for joint management, but the focus is almost exclusively on surface water, infrastructure and flow distribution during the growing season.

Groundwater of the Shu basin is represented by several alluvial and intermountain aquifers, such as the Shu alluvial aquifer (Zhambyl region, Kazakhstan), actively used for water supply; Merke and Kordai depressions, containing fresh and slightly mineralized waters; and Groundwater deposits in the Chui Valley (Kyrgyzstan), including those used in the agricultural sector [51-52].

Hydrogeological information on the basin is fragmentary and, in general, based on Soviet and post-Soviet research. There is currently no regular state or transboundary monitoring of groundwater. The level of mineralization of water in the basin fluctuates between 0.3 and 1.5 g/L, with seasonal variations influenced by melioration and climatic conditions. In some areas, increased nitrate concentrations have been recorded due to agricultural activities.

A significant obstacle to implementing the provisions of the Helsinki Convention is the lack of institutionalized mechanisms for accounting for and coordinating groundwater management. Unified assessment methods have not been developed; there are no maps of transboundary aquifers; and there is no coordination regarding zoning sanitary protection zones. There is also no publicly available digital database, although individual hydrogeological reports are available from specialized institutes.

In addition, the Shu basin is highly vulnerable to climate change, especially in the mountainous areas where runoff originates. Decreasing snow cover and increasing interannual runoff variability increase the pressure on groundwater as a reserve source, further increasing the need for its regulation in a transboundary context.

Thus, the experience of the Shu basin demonstrates a significant gap between the principles of the Helsinki Convention and the actual practice of groundwater management in Central Asia. The potential for integrating these resources into bilateral and regional cooperation mechanisms is obvious, but requires:

– data systematization;
– strengthening the scientific base;
– legal consolidation of the status of transboundary aquifers;
– as well as the involvement of international organizations in the development of monitoring and dialogue.

Without the formal delineation of transboundary aquifers, the establishment of a joint monitoring system, and the integration of groundwater into the mandate of the bilateral commission, the practical implementation of the Helsinki Convention in the Shu Basin will remain largely declarative thereby limiting the sustainability of transboundary water governance in the basin.

3.2. Comparative analysis of transboundary water governance in Europe, Central Asia, and Africa

The results of the analysis show significant differentiation in the degree and form of application of the provisions of the 1992 Helsinki Convention in different regions [11, 12]. In the European context, using the example of the Danube basin [31-32], the Convention serves as a basis for establishing sustainable management institutions, in which groundwater is considered an integral part of the basin approach. Regular monitoring, coordinated aquifer protection programmes and joint scientific research ensure a high level of transparency and transboundary trust (Table 1).

Table 1. Comparative assessment of transboundary groundwater governance under the 1992 Helsinki Convention

Criteria	Europe (Danube Basin)	Africa (Nile Basin)	Central Asia (Shu Basin)
Ratification status	Ratified by most basin states; fully operational within EU legal framework	Partially ratified; limited legal harmonization	Kazakhstan ratified; Kyrgyzstan not a Party; limited implementation
Level of institutionalization	High: ICPDR, binding basin management plans, structured reporting cycles	Medium: Nile Basin Initiative; limited binding authority	Low: Bilateral agreement (2000); weak coordination mechanisms
Integration of groundwater into basin management	Fully integrated into River Basin Management Plans; groundwater treated as water bodies	Limited integration; primary focus on surface water	Very limited integration; groundwater not systematically incorporated
Delineation of transboundary aquifers	Clearly identified and mapped transboundary groundwater bodies (TGWBs)	Partially identified; limited formal delineation	No formal delineation of transboundary aquifers
Groundwater monitoring	Regular monitoring with unified methodology and reporting standards	Episodic and project-based monitoring	Fragmented or local monitoring; no coordinated transboundary system
Use of GIS and hydrogeological data	Actively integrated into basin planning and decision-making	Basic and project-dependent use	Isolated initiatives; no system-wide integration
Coordination of water use standards	Regulated through multilateral agreements and EU directives	Ongoing negotiations; heterogeneous national standards	No coordinated standards for groundwater abstraction
Formal basin agreements	Danube Convention and EU directives provide binding framework	Basin cooperation agreements; limited groundwater coverage	Bilateral agreements exist; groundwater largely excluded
Key challenges and gaps	Balancing national interests; pollution control	Political instability; funding constraints	Limited monitoring capacity; absence of coordinated groundwater governance

In Africa (the Nile River basin) [40-42], despite attempts to harmonize legal regulation, the level of institutional implementation remains low. Groundwater is practically not considered an object of transboundary regulation, which creates preconditions for environmental risks (Table 1).

Central Asia, despite formal agreements, shows limited implementation of the Convention's hydrogeological components. In particular, in the Shu River basin (Zhambyl region, Kazakhstan), groundwater monitoring is not systematic, and legal regulation is declaratory [49-52]. The Interstate Commission on the Use of Waters of the Shu and Talas Rivers functions irregularly, and the protection of underground aquifers is practically not included in its mandate (Table 1).

Table 1 provides a comparative analysis of the application of the Helsinki Convention in different regions of the world, reflecting the extent to which countries have formalized and institutionalized cooperation in transboundary water governance. In particular:

– Europe demonstrates the most advanced level of implementation of the Convention with regard to groundwater, supported by strong institutional structures and technological capacity.

– Africa is progressing toward groundwater integration but continues to face resource, legal, and coordination constraints.

– Central Asia, despite the existence of formal cooperation frameworks, has not yet systematically incorporated groundwater, including in the Shu Basin, into a sustainable transboundary governance system.

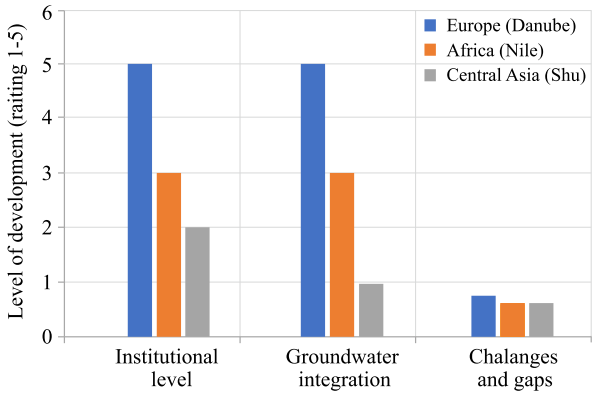

Figure 1. Comparative assessment of transboundary groundwater governance in Europe, Africa, and Central Asia

Figure 1 illustrates the comparative scoring of three regions across key dimensions of transboundary groundwater governance. Europe (Danube Basin) demonstrates consistently high performance across all assessed criteria. Africa (Nile Basin) shows a moderate level of institutionalization and partial integration of groundwater, though significant governance challenges remain. Central Asia (Shu Basin) exhibits the lowest scores, particularly with respect to groundwater monitoring and institutional integration.

Overall, the effectiveness of the Convention's implementation depends on political commitment, the strength of institutional arrangements, and the technical capacity to monitor and manage hydrogeological systems.

3.3. Perspectives for further research

Further research should focus on the development of a formalized assessment framework for evaluating the implementation of the Helsinki Convention with respect to transboundary groundwater. In particular, there is a need to operationalize measurable indicators covering aquifer delineation, monitoring density, data exchange frequency, abstraction control mechanisms, and institutional mandates. The construction of a composite governance index would allow moving from qualitative comparison to quantitative benchmarking across regions.

For the Shu transboundary basin, priority should be given to hydrogeological delineation of potential transboundary aquifers using updated geological, geophysical, and GIS-based spatial analysis. Joint field investigations aimed at identifying hydraulic connectivity across the Kazakhstan-Kyrgyzstan border would provide an empirical basis for formal recognition of shared groundwater bodies. Establishing a harmonized monitoring network with agreed observation wells and standardized chemical parameters would allow assessment of long-term trends and climate-driven variability.

A separate line of research should address the legal dimension by conducting a structured gap analysis between specific provisions of the Helsinki Convention (Articles on monitoring, information exchange, and prevention of transboundary impact) and the current mandate of the bilateral Shu-Talas Commission. Such analysis could support proposals for expanding the Commission's competence to explicitly include groundwater.

Finally, climate impact modelling for the Shu basin should be integrated with groundwater recharge assessments to evaluate the role of aquifers as buffer systems under decreasing snow cover and increasing interannual runoff variability. Coupling hydrological and hydrogeological models would enable scenario-based evaluation of future water security risks.

4. Conclusions

The study confirmed that the application of the 1992 Helsinki Convention varies significantly across geographical and political-institutional contexts. The European region demonstrates the highest level of integration of the Convention's provisions, including groundwater protection, through developed institutions and sustainable funding. In Central Asia, implementation is limited, particularly regarding groundwater, despite the existence of transboundary agreements. A weak institutional framework and the absence of a systematic approach to hydrogeological components characterize the African context.

Sustainable transboundary water management is impossible without integrating groundwater into the international regulatory system. The Helsinki Convention provides the necessary legal framework, but its practical implementation requires political will, institutional maturity and technical capacity. In Central Asia, and in particular the Shu River basin, there is an urgent need to develop joint groundwater monitoring programs, to incorporate hydrogeological data into decisions of interstate commissions, and to adapt best international practices at the local level. The article confirms that the transition from formal to functional cooperation is possible only with sustainable funding, access to data and institutional openness.

Author contributions

Conceptualization: DKA; Data curation: YZM, DKA; Formal analysis: EVS, JS, SRT; Funding acquisition: YZM; Investigation: AMB; Methodology: SRT, DKA; Project administration: EVS; Resources: EVS, JS, SRT; Software: ABM, SRT; Supervision: YZM; Validation: DKA, EVS; Visualization: EVS, JS; Writing – original draft: DKA; Writing – review & editing: YZM. All authors have read and agreed to the published version of the manuscript.

Funding

This research was funded by the Science Committee of the Ministry of Science and Higher Education of the Republic of Kazakhstan, grant number AP09260877 (2024-2026 years).

Acknowledgements

The authors express their sincere gratitude to the editor and anonymous reviewers for their constructive comments and valuable suggestions, which have significantly improved the quality of this manuscript.

Conflicts of interest

The authors declare no conflict of interest.

Data availability statement

The original contributions presented in this study are included in the article. Further inquiries can be directed to the corresponding author.

References

[1] Jakelow, A.K. (1970). Hydrogeology of the USSR. Volume XXXVI. Southern Kazakhstan. *Moscow: Nedra*, 473. https://g.eruditor.one/file/868887/?ysclid=lkwhev67jq627554410

[2] Bakker, K., & Morinville, C. (2013). The governance dimensions of water security: a review. *Philosophical transactions of the Royal society A, 371,* 20130116. https://doi.org/10.1098/rsta.2013.0116

[3] Dzhakelov, A.K. (1993). Formation of underground waters of the Chu-Sarysu artesian basin, their resources and prospects for use. *Almaty: Gylym*. https://search.rsl.ru/ru/record/01000594988?ysclid=mc1swfof7n833755399

[4] Sagin, J., Adenova, D., Tolepbayeva, A. & Poryadin, V. (2017). Underground water resources in Kazakhstan. *International Journal of Environmental Studies, 74(3),* 386-398. https://doi.org/10.1080/00207233.2017.1288059

[5] Peter, H. Gleick. (1998). The human right to water. *Water Policy, 1*(5), 487-503. https://doi.org/10.1016/S1366-7017(99)00008-2

[6] Ingrao, C., Strippoli, R., Lagioia, G., & Huisingh, D. (2023). Water scarcity in agriculture: An overview of causes, impacts and approaches for reducing the risks. *Heliyon*, *9(8), e18507* https://doi.org/10.1016/j.heliyon.2023.e18507

[7] Unfried, K., Kis-Katos, K., & Poser, T. (2022). Water scarcity and social conflict. *Journal of Environmental Economics and Management*, *113*, 102633. https://doi.org/10.1016/j.jeem.2022.102633

[8] UNESCO World Water Assessment Programme (WWAP). (2018). *The United Nations world water development report 2018: Nature-based solutions for water*. UNESCO.

[9] UNESCO World Water Assessment Programme (WWAP). (2015). *The United Nations world water development report 2015: Water for a sustainable world*. UNESCO. https://www.unescap.org/sites/default/files/__WWDR-2015.pdf

[10] UNESCO. (2022). *The United Nations world water development report 2022: Groundwater: Making the invisible visible*. UNESCO. https://www.unesco.at/fileadmin/Redaktion/Publikationen/Publikations-Dokumente/WWDR_2022_EN_report_web_0.pdf

[11] *Conventions and agreements.* (1992). Retrieved from: https://www.un.org/ru/documents/decl_conv/conventions/watercourses_lakes.shtml?ysclid=mc1tkmwygi899182835

[12] *Convention for the protection of the marine environment of the Baltic Sea area, 1992 (Helsinki Convention)*. (1992). Retrieved from: https://helcom.fi/wp-content/uploads/2019/06/Helsinki-Convention_July-2014.pdf

[13] Absametov, M.K., Adenova, D.K. & Nusupova, A.B. (2019). Assessment of the impact of anthropogenic factors water resources of Kazakhstan. *NEWS of the National Academy of Sciences of the Republic of Kazakhstan. Series of geology and technical sciences*, *1(433),* 248-254. https://doi.org/10.32014/2019.2518-170X.30

[14] Adenova, D., Tazhiyev, S., Sagin, J., Absametov, M., Murtazin, Y., Trushel, L., Miroshnichenko, O. & Zaryab, A. (2023). Groundwater Quality and Potential Health Risk in Zhambyl Region, Kazakhstan. *Water*, *15,* 482. https://doi.org/10.3390/w15030482

[15] Kurishbaev, A., Amanzholova, R., Adenova, D., Sagin, J., Burlibayeva, D., Sarsekova, D., Alikhanov, K., Serikkanov, A. & King, R. (2024). Comparative Assessment of the Mountainous River Basin in Kyrgyz Kazakh Region of Central Asia with River Basins in Australia, Canada and USA. *Grassroots Journal of Natural Resources*, *7(1),* 99-122 https://doi.org/10.33002/nr2581.6853.070106

[16] Myers, R.A., Gyimah, E., Gbemadu, K., Osei, B., & Akoto, O. (2023). Appraising groundwater quality and the associated health risks of heavy metal contamination at Suame magazine. *Scientific African, 21,* e01794 https://doi.org/10.1016/j.sciaf.2023.e01794

[17] *Guidelines for integrated water resources management in transboundary river, lake and aquifer basins*. Paris: AFD 2012, 117. Retrieved from: http://cawater-info.net/library/rus/gwp/inbo_handbook2_rus.pdf

[18] *On the accession of the Republic of Kazakhstan to the Convention on the Protection and Use of Transboundary Watercourses and International Lakes*. (2000). Retrieved from: https://adilet.zan.kz/rus/docs/Z000000094_

[19] Selected transboundary water agreements concluded by European and Asian states. (2019).

[20] Transboundary Flood Risk Management: Experiences from the UNECE Region. – New York-Geneva: UNECE. (2009). *Retrieved from:* https://hydrology.nl/images/docs/alg/Transboundary_Flood_Risk_Management_RUS.pdf

[21] RIOB. (2025). International Network of Basin Organizations. *Retrieved from*: https://www.inbo-news.org/fr/reseau-international-des-organismes-de-bassin/

[22] *Model Provisions on Transboundary Groundwaters*. New York. (2014). Retrieved from: http://cawater-info.net/library/rus/ece-gw.pdf

[23] Zhatkanbaeva, A.Ye., Jangabulova, A.K. & Aydarkhanova, K.N. (2020). Problems of legal regulation of the use of transboundary water bodies in Central Asia. *Journal of Actual Problems of Jurisprudence*, *93*(1), 94-101. https://doi.org/10.26577/JAPJ.2020.v93.i1.10

[24] Abdirova, Z.Sh. & Nurtaeva, Zh. K. (2021). Transboundary waters of Central Asia: legal aspects and cooperation challenges. *Ecological Bulletin of KazNU*, *2*(79), 43-51.

[25] Borisova, E.A. (2014). History of the development of conflicts over water resources in Central Asia in the post-Soviet period. *East (Oriens). Series "International Relations"*, *2,* 80-86.

[26] *National Plan for Integrated Water Resources Management and Improving Water Use Efficiency in the Republic of Kazakhstan for 2009-2025*. Resolution of the Government of the Republic of Kazakhstan dated January 28, 2009 № 67. Online. 20 May 2025. Retrieved from: https://adilet.zan.kz/rus/docs/P090000067

[27] National Atlas of the Republic of Kazakhstan. Medeu, A.R., Eds., *Almaty: Vit brand*, 158. *Retrieved from*: https://kazneb.kz/ru/catalogue/view/1518410

[28] Smolyar, V.A. (2023). Creation of an Atlas of hydrogeological maps of the Republic of Kazakhstan based on geographic information systems. *Geological and Subsoil Protection, 1(86),* 63-79.

[29] Shahbazbegian, M., & Noori, R. (2022). Hydropolitical system archetypes: Feedback structures, physical environments, unintended behaviors, and a diagnostic checklist. *Hydrology, 9,* 207. https://doi.org/10.3390/hydrology9120207

[30] Sydykov, Zh.S. & Shlygina, V.F. (1998). Underground waters of Kazakhstan. Structural-hydrogeological basis and systematics. *Handbook; Galym Almaty, Kazakhstan*. *Retrieved from*: https://rusneb.ru/catalog/010003_000061_d92d6c733950a9d81469b6bdd5fc72d9/?ysclid=m17sngziql298425491

[31] Nachtnebel, H.P. (2000). The Danube river basin environmental programme: plans and actions for a basin wide approach. *Water Policy*, *2*(1-2), 113-129. https://doi.org/10.1016/S1366-7017(99)00025-2

[32] Luzern Declaration. (1993). *Environmental action programme for Central and Eastern Europe. Document submitted to the Ministerial Conference*. Luzern, Switzerland. Retrieved from: http://www.eco-forum.org

[33] Directive 2000/60/EC of the European parliament and ofthe council. *Retrieved from:* eur-lex.europa.eu

[34] Buijs, P.H.L. (1991). *Proceedings of Environmental Management Programme for the Danube River Basin*. Background Document for the Technical Expert Meeting, Sofia.

[35] Buijs, P.H.L., Uzunov, K. & Tzankov, K. (1992). W*ater quality of the Danube River along the Bulgarian – Romanian stretch, June 1991*. ICWS-Report 92/01, Amsterdam

[36] *Commission du Danube*. (1992). Annuaire Hydrologique 1990. Budapest, Hungary.

[37] Danube River Protection Convention. (1994). *Proceedings of Convention on the Co-operation for the Protection and Sustainable Use of the Danube River*. Sofia, Bulgaria.

[38] IUCN. (1993). *The wetlands of Central and Eastern Europe. IUCN Report*, 1196 Gland, Switzerland.

[39] Luzern Declaration. (1993). *Environmental action programme for Central and Eastern Europe*. Document submitted to the Ministerial Conference. Luzern, Switzerland.

[40] Tatenda, D., Takudzwa, M., Linton, M., Chipo, M., Collins, O. & Pule, M.P. (2024). Rivers of West Africa. *Afrotropical Streams and Rivers: Structure, Ecological Processes and Management*, 129-161. https://doi.org/10.1016/B978-0-443-23898-7.00006-3

[41] Almesafri A., Abdulsattar S., Alblooshi A., Al-Juboori Raed A., Jephson N., & Hilal N. (2024). Waters of Contention: The GERD and Its Impact on Nile Basin Cooperation and Conflict. *Water* , 16(15). https://doi.org/10.3390/w16152174

[42] Portal. (2018). *Nile Basin Initiative*. Retrieved from: https://www.rti.org/impact/nile-river-basin-initiative

[43] Howeidy, A. (2020). *Egypt-Ethiopia Nile Water Dispute: A Timeline. Ahram Online*. Retrieved from: https://english.ahram.org.eg/News/369666.aspx

[44] Bishop, K., Lyon, S.W., & Dahlke, H.E. (2012). The relationship between land use and water. *Eos Trans. Am. Geophys. Union 93*(28), 259. https://doi.org/10.1029/2012EO280004

[45] Olago, D., Opere, A. & Barongo, J. (2009). Holocene palaeohydrology, groundwater and climate change in the lake basins of the Central Kenya Rift. *Hydrological Sciences Journal*, *54*(4), 765-780. https://doi.org/10.1623/hysj.54.4.765

[46] Bretzler, A., Osenbrück, K., Gloaguen, R., Ruprecht, J.S., Kebede, S., & Stadler, S. (2011). Groundwater origin and flow dynamics in active rift systems - A multi-isotope approach in the Main Ethiopian Rift. *Journal of Hydrology*, *402*(3-4), 274-289 https://doi.org/10.1016/j.jhydrol.2011.03.022

[47] Chikozho, C. (2014). Pathways for building capacity and ensuring effective transboundary water resources management in Africa: Revisiting the key issues, opportunities and challenges. *Physics and Chemistry of the Earth, Parts A/B/C,* 76-78, 72-82 https://doi.org/10.1016/j.pce.2014.11.004
[48] Global Environment Facility (GEF). (2025). Trust Fund. https://fiftrustee.worldbank.org/en/about/unit/dfi/fiftrustee/fund-detail/gef
[49] Adenova, D., Sarsekova, D., Absametov, M., Murtazin, Ye., Sagin, J., Trushel, L. & Miroshnichenko, O. (2024). The Study of Groundwater in the Zhambyl Region, Southern Kazakhstan, to Improve Sustainability. *Sustainability*, *16*(11), 4597. https://doi.org/10.3390/su16114597
[50] AGREEMENT between the Government of the Republic of Kazakhstan and the Government of the Kyrgyz Republic. (2020).
[51] Murtazin, Ye.Zh., Adenova, D.K. & Tazhiyev, S.R. (2022). Assessment of the potential of self-discharging hydrogeological wells for sustainable development of rural areas of Zhambyl region. *NEWS of the National Academy of Sciences of the Republic of Kazakhstan, series of geology and technical sciences*, *455*(5), 143-155. https://doi.org/10.32014/2518-170X.223
[52] Medeu, A.R., Malkovskiy, I.M., Toleubayeva, L.S. (2017). The TranskazakhstaN channel – strategic priorities of steady water supply Republic of Kazakhstan. *News of the National Academy of Sciences of the Republic of Kazakhstan, series of geology and technical sciences, 425*(5), 109-120.

Трансшекаралық жерасты суларын басқару бойынша 1992 жылғы Хельсинки конвенциясының жүзеге асырылуы: Шу бассейнінің жағдайы мен салыстырмалы талдауы

Д.К. Аденова[1*], Е.Ж. Муртазин[1], Дж. Сагин[2], Е.В. Сотников[1], С.Р. Тажиев[1], А.М. Байкадамова[1]

[1]*У.М. Ахмедсафин атындағы Гидрогеология және геоэкология институты, Алматы, Қазақстан*
[2]*Батыс Мичиган университетінің геология және қоршаған орта ғылымдары бөлімі, Каламазу, АҚШ*

**Корреспонденция үшін автор: adenovadinara@gmail.com*

Аңдатпа. Тұщы су тапшылығының артуы және климаттың өзгеруі жағдайында жерасты суларының ресурстарын қоса алғанда, трансшекаралық суды тиімді басқару ерекше маңызға ие. 1992 жылғы Хельсинки конвенциясы трансшекаралық су ағындары мен сулы горизонттарды қорғау және ұтымды пайдалану саласындағы мемлекеттердің ынтымақтастығына халықаралық құқықтық негіз береді. Бұл мақала гидрогеологиялық аспектілерге баса назар аудара отырып, әлемнің әртүрлі аймақтарында – Еуропада, Орталық Азияда және Африкада Конвенция ережелерін іске асыру тәжірибесін салыстырмалы талдауға бағытталған. Халықаралық стандарттарды ішінара енгізу жағдайы ретінде Қазақстан мен Қырғызстан аумағында орналасқан Шу трансшекаралық бассейніне ерекше назар аударылады. Жерасты суларын басқару, мониторинг және қорғау тәжірибесін жүйелі талдау негізінде Конвенцияның ережелерін өңірлік су саясаты мен институционалдық тетіктерге интеграциялау бойынша ұсыныстар ұсынылады. Зерттеудің мақсаты – 1992 жылғы Хельсинки конвенциясының трансшекаралық жерасты суларына баса назар аудара отырып, әлемнің әртүрлі аймақтарында қолдану тәжірибесіне салыстырмалы талдау жасау, Шу бассейнінің мысалында оны жүзеге асырудың проблемалары мен перспективаларын көрсету. Зерттеу 1992 жылғы Хельсинки конвенциясын қолдану географиялық және саяси-институционалдық контекстке байланысты айтарлықтай өзгеретінін растады.

Негізгі сөздер: *трансшекаралық жерасты сулары; су қауіпсіздігі; құқықтық реттеу; Орталық Азия.*

Имплементация Хельсинкской конвенции 1992 года в управлении трансграничными подземными водами: сравнительный анализ и пример Шуйского бассейна

Д.К. Аденова[1*], Е.Ж. Муртазин[1], Дж. Сагин[2], Е.В. Сотников[1], С.Р. Тажиев[1], А.М. Байкадамова[1]

[1]*Институт гидрогеологии и геоэкологии им. У.М. Ахмедсафина, Алматы, Казахстан*
[2]*Кафедра геологических и экологических наук, Университет Западного Мичигана, Каламазу, США*

**Автор для корреспонденции: adenovadinara@gmail.com*

Аннотация. В условиях нарастающего дефицита пресной воды и изменения климата особое значение приобретает эффективное трансграничное водное управление, включая подземные водные ресурсы. Хельсинкская конвенция 1992 года обеспечивает международно-правовую основу для сотрудничества государств в сфере охраны и рационального использования трансграничных водотоков и водоносных горизонтов. Настоящая статья направлена на сравнительный анализ практики реализации положений Конвенции в различных регионах мира – Европе, Центральной Азии и Африке – с акцентом на гидрогеологические аспекты. Особое внимание уделено Шуйскому трансграничному бассейну, расположенному на территории Казахстана и Кыргызстана, как кейсу частичной имплементации международных

норм. На основе системного анализа практик управления, мониторинга и защиты подземных вод предложены рекомендации по интеграции положений Конвенции в региональные водные политики и институциональные механизмы. Целью исследования является в проведении сравнительного анализа практики применения Хельсинкской конвенции 1992 года в различных регионах мира с акцентом на трансграничные подземные воды, выделяя проблемы и перспективы её имплементации на примере Шуйского бассейна. Проведённое исследование подтвердило, что применение Хельсинкской конвенции 1992 года существенно варьируется в зависимости от географического и политико-институционального контекста.

Ключевые слова: *трансграничные подземные воды; водная безопасность; правовое регулирование; Центральная Азия.*

Publisher's note

All claims expressed in this manuscript are solely those of the authors and do not necessarily represent those of their affiliated organizations, or those of the publisher, the editors and the reviewers.

CONTENTS

МАЗМҰНЫ

СОДЕРЖАНИЕ

Publisher: Satbayev University

Registration:
Ministry of Information and Social Development of the Republic of Kazakhstan
No. KZ19VPY00056529 dated 30 September 2022 (re-registration)

Official website: https://vestnik.satbayev.university/index.php/journal/

Established in August 1994. Published bimonthly

Editorial Office Address:
Satpayev St., 22, Almaty, Kazakhstan
Tel.: +7(727) 292-63-46